University of Glasgow

Silicon Pixel Detectors for Synchrotron Applications

Graeme Douglas Stewart

Submitted in fulfilment of the requirements for

the Degree of Doctor of Philosophy

April 2013

School of Physics and Astronomy

College of Science and Engineering

University of Glasgow

Abstract

Recent advances in particle accelerators have increased the demands being placed on detectors. Novel detector designs are being implemented in many different areas including, for example, high luminosity experiments at the LHC or at next generation synchrotrons. The purpose of this thesis was to characterise some of these novel detectors.

The first of the new detector types is called a 3D detector. This design was first proposed by Parker, Kenney and Segal (1997). In this design, doped electrodes are created that extend through the silicon substrate. When compared to a traditional photodiode with electrodes on the opposing surfaces, the 3D design can combine a reasonable detector thickness with a small electrode spacing resulting in fast charge collection and limited charge sharing.

The small electrode spacing leads to the detectors having lower depletion voltages. This, combined with the fast collection time, makes 3D detectors a candidate for radiation hard applications. These applications include the upgrades to the Large Hadron Collider (LHC) leading to the High Luminosity Large Hadron Collider (HL-LHC). The limited charge sharing of the devices can also improve their performance when being employed as imaging sensors. This will provide benefits in X-ray diffraction experiments.

The first experiment to evaluate the 3D detector design analysed for this thesis involved utilising a telescope consisting of 6 calibrated detector planes and a beam of pions from the Super Proton Synchrotron (SPS) at CERN. Once the tracks through the telescope were reconstructed, these gave predicted hits on the 3D detector that could be compared to the recorded energy depositions. By making this comparison, a measure of the detector's efficiency in various regions of the pixels was made. The overall efficieny of the pixel was measured at $93.0 \pm 0.5\%$. The detector was also rotated with respect to the incident beam, increasing the efficiency to $99.8 \pm 0.5\%$ for an angle of 10°, and the detector bias was altered to measure the effect of over-depletion. Measurements of the charge sharing and resolution properties of the device were also reported.

Another detector design that was investigated was a slim edge detector. Instead of the typical guard ring structures that a normal device would employ, this detector reduced the

size of these structures to enable easier tiling of the detectors. This was done by scanning the reduced edge and the standard edge of the detector with an X-ray beam with a width FWHM of 7 μm and 15 keV. The noise level of the strip closest to the cleaved edge was twice as large as that of the adjacent strip with no degradation of the charge collection capacity.

The next experiment to evaluate a short, double sided 3D strip detector was a Transient Current Technique (TCT) experiment. The TCT technique allows the electric field in the 3D devices to be probed in a way not possible before. The TCT technique uses the current waveform produced by the detector in response to a near delta function point laser pulse (illumination). The waveforms are recorded as a function of illumination position over the surface of the device under test as a function of detector bias.

This data gives information on the portion of the induced signal from electron or hole motion. From the rise times of the signals the velocity profile of the carriers in the devices and therefore electric fields can be determined. The collected charge was calculated from the integral of the waveforms.

The detectors were tested prior to irradiation, after irradiating to a dose of 5 x 10^{15} 1 MeV equivalent neutrons/cm^2, and after periods of annealing at elevated temperatures. Annealing was achieved in situ by warming to 60 °C for 20 to 600 minutes corresponding to room temperature annealing of between 8 and 200 days.

Before irradiation, full lateral depletion between the columns occurs at low bias voltages, at approximately 3 V. A uniform carrier velocity between the columns is not achieved until the bias is equal to 40 V. Both the drift of electrons and holes provide equal contributions to the measured signals. After irradiation there is clear charge multiplication enhancement along the line between columns with a very non-uniform velocity profile in the unit cell of the device. In addition, charge trapping greatly suppresses the contribution of the holes on the signal produced.

The final novel detector type was an Active Pixel Sensor (APS). Recent developments in CMOS fabrication processes have allowed new sensors to be developed and tailor-made for specific applications. These challenge traditional Charge Coupled Devices (CCD) in some

areas. The characterisation of the APS device took place in an X-ray diffraction experiment at the Diamond Light Source where it was evaluated alongside a CCD. The camera gain and stability had been determined prior to the experiment taking place. During the experiment, the dark current, noise, signal to noise and image lag performance was evaluated and compared between the APS and the CCD. The signal to noise of the APS and the CCD was comparable (150 and 200 respectively) when the same integration time was used.

Contents

List of Tables

List of Figures

Acknowledgements

Grateful for their efforts, I would like to thank my supervisors for their tireless assistance and guidance over the years. Richard Bates has provided constant support and encouragement for which I am very grateful. Additionally, I would like to thank Chris Parkes for his assistance, particularly with the 3D testbeam work. Even though he only assisted in the final stages, Lars Eklund's diligence in reading every chapter of my thesis is to be commended.

Moreover, I would like to thank the Diamond Light Source for their CASE award that made the research viable. Examples of people at Diamond that assisted me are too numerous to mention individually, but Nicola Tartoni and Julien Marchal supported me throughout the characterisation of the Vanilla APS and assisted with the testbeams on various Diamond beamlines, and I would also like to thank the beamline scientists and technicians that made the experiments possible at any and every hour of the day.

I would also like to recognise the large amount of assistance I received from various people at CERN. Specifically, Marco Gersabeck and Paula Collins deserve credit for their help in understanding the data from the 3D sensors in the testbeam at CERN. Great credit should also be due to Richard Plackett and his team for the organisation of the testbeam itself.

Of course, these experiments would not have been possible without any sensors to test. Detectors were produced for the APS work by the Rutherford Appleton Laboratory and for the 3D work by CNM. Andy Clark (RAL) and Guilio Pellegrini (CNM) provided assistance with smoothing out the operation of these sensors. Andy Blue also provided invaluable guidance in the APS work.

The final aspect of my work was a series of measurements based at the Jožef Stefan Institute in Ljubljana. I would like to thank Gregor Kramberger and Marko Milovanovic for their time and patience when explaining the experiment and code they had developed.

The office mates of rooms 337 and then 329b deserve a mention. Thanks then to Kenny for pretending to understand ROOT and to Dima for helping make detectors work and for asking questions as he's leaving a room. Thanks also to Aaron for whatever it was that he

did. Probably something to do with potatoes.

For reminding me of a world outside of physics, which was nice to visit on occasion, I would like to thank my friends in the Glasgow University Mountaineering Club and at the 29^{th} Glasgow Scout Group. The recommendations of additional research from Martin and Craig certainly was appreciated.

Finally, I would like thank my family and Kate for I would not have come this far without their love and support.

Declaration

I declare that except where explicit reference is made to the work of others, this dissertation is the result of my own work. This work has not been submitted for any other degree at the University of Glasgow or any other institution.

Graeme Stewart

Chapter 1

Motivation

1.1 Applications of Silicon Detectors for Ionising Radiation Measurement

1.1.1 A History of Radiation Detection

From the earliest days of particle physics, improvements in radiation detection has allowed new discoveries to be made. In 1895, Wilhelm Röntgen used primarily photographic plates to discover X-rays and to create the first X-ray image [1]. Photographic film was being used at similar times, but had many of the same drawbacks. These drawbacks included their fragility, low sensitivity and non-linear response.

Although many of the earliest discoveries in particle physics utilised photographic plates and films, the observable effects of the radiation were limited to the interaction with bulk materials. It was only with the invention of the cloud chamber by Charles Wilson in 1911 that allowed the interaction of radiation with individual atoms and particles to be recorded [2]. His detector design involved rapidly expanding air to decrease its temperature. The newly cooled air will now be over-saturated with suspended water vapour. This water vapour will then condense around any ions in the chamber, forming visible clouds. Radiation that passes through the chamber leaving a track of ionisation will also leave a visible cloud trail. From this trail, individual particles could be recorded for the first time. Of particular note,

the discoveries in cosmic rays of the positron in 1932 [3] and the K-meson in 1947 [4] were only possible because of cloud chambers.

The main disadvantage that a cloud chamber has is that it cannot operate continuously. However, this can be negated by replacing the gas in a cloud chamber with a superheated liquid. This design is known as a bubble chamber [5]. The resolution of bubble chambers was improved to a few micrometers [6] and were instrumental in the 1983 discoveries of the Z and W bosons. Similarly to cloud chambers, bubble chambers still required the tracks to be photographed. Semiconductor detectors, alongside wire chambers and spark chambers, provided new methods to measure radiation interactions.

The earliest semiconductor detectors were developed in the 1960s [7]. Silicon, partly due to its use in other areas of the semiconductor industry, quickly became the most widespread semiconductor used in detectors. The advantage of a semiconductor detector over a bubble chamber is in operating in low-amplitude signal conditions and providing a high precision of position sensitivity alongside their speed and the fact that they are directly read out, rather than requiring a further stage of photography. This has lead to their prevalence in many fields of experimental physics, such as particle physics, astrophysics and X-ray imaging.

The earliest silicon detectors created were simple pad diodes. Over the decades since, many more complex designs have been developed. The developments most important to this thesis are the planar technology and the advent of 3D detectors [8]; the tiling of detectors through slim edge processes [9]; and imaging CCDs [10] and CMOS sensors [11].

1.1.2 Synchrotrons and X-ray Detection

The design of particle accelerator known as a synchrotron was first proposed in the 1940s [12]. A synchrotron can be used to accelerate charged particles to very high energies. These high energy particles can then be used in high energy physics experiments or their Bremsstrahlung radiation can be used to create intense beams of photons.

By using a series of bending and accelerating magnets, it is possible to accelerate bunches of particles to high energies whilst keeping their radius of curvature constant. The energy

of the particle is proportional to the magnetic field and the radius of curvature of the synchrotron. The largest magnets in use today are superconducting magnets and they can produce a field of up to 10 T. This limits the maximum achievable energy of a synchrotron to the physical radius of the beam's curvature by,

$$B\rho = \frac{p}{q} \approx \frac{E}{cq}, \tag{1.1}$$

where B is the magnetic field, ρ is the radius of curvature, p is the momentum of the particle, q is the charge and E is the particle's energy. At relativistic velocities the momentum, p, approximates to E/c. The bunches of particles can be focused using additional magnets and radio-frequency cavities [12].

The bending magnets in a synchrotron are dipole magnets. When a particle is accelerated by these magnets, it will emit electromagnetic radiation. The power, P, radiated by the particle, when traveling at a relativistic velocity is,

$$P = \frac{1}{6\pi\epsilon_0}\frac{q^2 c}{\rho^2}\gamma^4, \tag{1.2}$$

where ϵ_0 is the permittivity of free space, c is the speed of light in a vacuum and γ is the Lorentz factor. The wavelength of the photons emitted depends on the relativistic kinetic energy of the accelerated particle - photons with energies from infra-red through to X-rays will be observed. The spectra from synchrotron radiation will typically peak in the X-ray band and can be used for a variety of scientific applications. These can vary from crystallographic diffraction, microscopy or spectroscopy. As a result, the detectors used by a synchrotron beamline will be suited specifically to the needs of the experiments being undertaken. This demand will drive the development of new detectors in particular directions. Currently, 3rd generation synchrotron facilities will typically use both CCD and CMOS sensors in their experiments depending on their requirements.

1.1.3 Colliders and Particle Detection

Another area where continual detector development is crucial is in particle colliders. For example upgrading the Large Hadron Collider (LHC) to the High Luminosity LHC (HL-LHC) will, by altering many aspects of the original design, increase the luminosity by a factor of 10 [13]. This will lead to an order of magnitude more particles produced in each bunch crossing, which will in turn demand a greater tolerance to radiation damage. Silicon sensors used to locate the vertex positions of particle collisions will be situated closest to the beam and will then suffer larger fluences of radiation.

Considering one of the experiments in the upgraded HL-LHC, the ATLAS experiment, the layer of detectors closest to the beam is called the insertable B-layer. This layer will have to withstand fluences of up to 1 x 10^{16} 1 MeV n_{eq}/cm^2 which is greater than the current inner-most pixel layer (the B-layer) was designed to withstand. The current B-layer was designed to tolerate doses up to 2 x 10^{15} 1 MeV n_{eq}/cm^2 and has survived operation at these fluences. Currently, there are several candidates for detector designs to replace this layer. They typically consist of a set of planar sensors with or without a set of complementary 3D sensors.

1.1.4 Thesis Summary

In Chapter 2, the basic development of detectors and the interaction of radiation with matter is discussed. Firstly, the fundamental properties that define semiconductors will be presented. Following on from this will be the adaption of semiconductor materials into detecting systems. This will start with PN junctions and will then investigate planar and 3D processes, and also CCD and CMOS devices. After that, the interaction of radiation with matter will be examined. This will involve looking at how charged and uncharged radiation interacts with a semiconductor and produces a measurable signal. Finally, the damaging artifacts that can be created by radiation in a semiconductor are reported on.

Chapters 3 through to 6 are where the results from the various experiments in this thesis will be reported. Chapter 3 contains an analysis of data from a 3D TimePix device in a test

beam. By combining the 120 GeV Pions with a MediPix telescope the efficiency, resolution, cluster size and collected charge could be determined for various bias voltages and incident beam angles. The potential for tiling multiple detectors is also investigated in a short section on slim edge detectors.

In Chapter 4, current formation in a double-sided 3D detector was probed using Transient Current Techniques (TCT). An infra-red laser with a picosecond pulse length was used to inject electron-hole pairs at different positions within the detector. By analysing the current signals recorded, the collected charge and the velocity of charge carriers can be determined. This is reported for the device before and after irradiation.

Chapter 5 compares a novel CMOS APS detector to a CCD in a typical synchrotron experiment. The APS detector studied was the Vanilla device developed by the MI[3] collaboration (Multidimensional Integrated Intelligent Imaging) [14] and the Rutherford Appleton Laboratory[1] (RAL). The CCD this was compared to was developed by Princeton Instruments[2] and is used by the Diamond Light Source[3] synchrotron in their experiments. Soft X-rays from the synchrotron were used to create a diffraction pattern from a permalloy sample that was then recorded with both the APS and the CCD. The noise and signal intensity of the two detectors was then compared.

Finally Chapter 6 will draw together the previous chapters and show some overall conclusions from the thesis.

[1]Rutherford Appleton Laboratory, Harwell, Oxford, UK.
[2]Princeton Instruments, Trenton, New Jersey, USA.
[3]Diamond Light Source, Harwell, Oxford, UK.

Chapter 2

Silicon Detectors in Modern Physics

In this chapter, firstly the electronic properties and characteristics of semiconductors in general will be investigated with a focus on silicon in particular. Secondly, various design configurations of semiconductor detectors will be discussed. Thirdly, the types of ionising radiation and the potential effects on a detector will be described.

2.1 Electronic Properties of Semiconductors

Solid-state materials can be broadly classified into three classes of materials: conductors, semiconductors and insulators. If, at 0 K, there is an energy gap between the filled electron shells and the empty electron shells then the material will display insulating properties. If there is no energy gap, then the material will behave as a conductor. If the temperature of the material is greater than 0 K, semiconducting properties can occur if the band gap is small enough that electrons can be thermally excited to the conduction band whereas insulating properties will continue to dominate for larger band gaps. An example of this is displayed in Figure 2.1.

There is a further difference between the conduction in metals and semiconductors when the temperature of the material is varied. Increasing the temperature of a semiconductor will increase the conductivity due to increasing the number of electrons in the conduction band. In a metal, however, there are not additional electrons available to the conduction band.

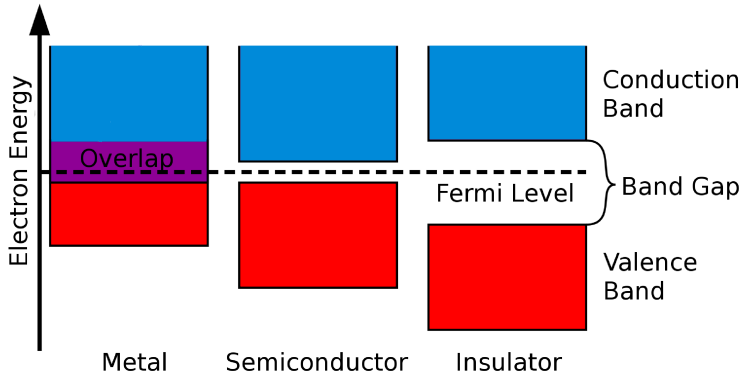

Figure 2.1: Example band gap diagram showing a metal, semiconductor and conductor with increasing band gaps.

Hence, the only effect of the increase in temperature is that the lattice vibrations increase causing greater scattering of the electrons. This increases the resistance and decreases the conductivity of the metal.

The band gap (E_g) is the difference in energy between the top of the valence band and the bottom of the conduction bands. The valence band is occupied by the valence electrons and is of lower energy than the adjacent conduction band. The relative energy levels are set so that the top of the valence band is at 0 eV. Any process (e.g. thermal or optical excitation) that elevates an electron from the valence band to the conduction band creates two charge carriers: a negative electron in the conduction band and a positive hole in the valence band.

The main difference between conductors, semiconductors and insulators is their conductivity. Conductors have a conductivity greater than 10^4 S/cm; insulators have a conductivity of less than 10^{-9} S/cm and semiconductors have a conductivity in the range in between [15]. The exact conductivity of a material is dependent on a number of factors, including the purity, magnetic field, temperature and illumination.

The first research into semiconductor properties was performed by Faraday in 1833 [16]. He discovered that the conductivity of silver sulphide was dependent on its temperature, unlike the metals and insulators known at the time. In the years since, further semiconductor materials have been discovered. The only pure elements with semiconductors properties are Group IV elements (for example, silicon and germanium). Other elements in groups II to VI can form semiconductor compounds, for example SiC, Cu_2O or GaAs. In the early 1950s,

germanium was considered the main material for semiconductor devices. However, from the 1960s onwards silicon has overtaken germanium in usage. Silicon has many properties that make it preferable to germanium. Firstly, silicon is the second most common element in the Earth's crust (behind oxygen). Consequently, high quality silicon is relatively cheap to produce. Finally, silicon devices operate well at room temperature because, at room temperature, the band gap of pure silicon is 1.12 eV, which is only slightly greater than the band gap of germanium at 0.67 eV.

The semiconductor materials studied have single crystal structures. This means that the atoms are arranged in a lattice, with a simple, periodic structure. Each atom in the lattice is held at its position, with only minor variations due to thermal vibrations. The smallest set of atoms that can be repeated to create the entire lattice structure is referred to as the crystal's unit cell. The lattice structure that any set of atoms forms is determined by the electronic arrangement. The simplest unit cell is the simple cubic structure, where each atom in the unit cell is at the vertex of a cube. There are many more complex arrangements possible for the atoms to situate themselves in. For example, a face-centred cubic structure has atoms at the vertices and in the centre of the faces of a cube. Silicon and germanium form the same tetrahedral structure as diamond. This diamond structure has essentially two face centred cubic sublattices, with the second one displaced from the first along the main diagonal by a quarter of the length of the diagonal. Compound semiconductors will often have different structures. For instance, GaAs (and other Group III and IV compound semiconductors) has a zinc blende structure. This is the same as the diamond structure, but where each sublattice contains either gallium or arsenic atoms exclusively. The diamond structure is shown in Figure 2.2.

The thermal motion of carriers is permanently present in semiconductors, although this is random and leads to no overall movement of charge. There are two main contributions to the overall motion of electrons and holes in a solid. Drift is the motion of the carriers resulting from the force applied by an electric field. Where a small electric field is present, the drift velocity (v) is proportional to the electric field (E) and the proportionality constant

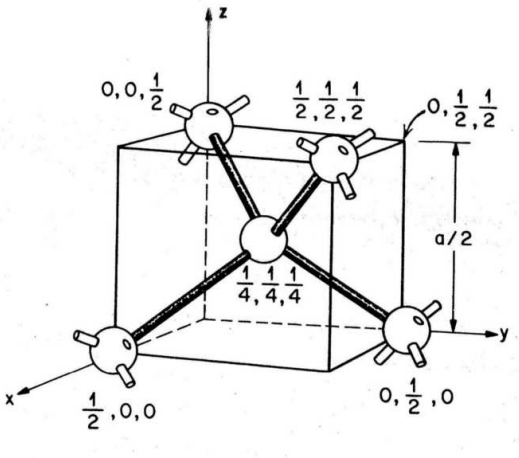

Figure 2.2: Crystal lattice diagram for silicon showing the tetrahedral structure. Taken from Sze, 2008 [15]

is given by the mobility for both the electrons (μ_e) and the holes (μ_h),

$$v_e = -\mu_e E \qquad v_h = \mu_h E. \tag{2.1}$$

The average velocity increases linearly with the field strength and is constrained by frequent scattering. As the electric field increases in magnitude, the velocity of the carriers eventually saturates. In silicon at room temperature, this occurs at velocities of 10^7 cm/s with an electric field strength of around 10^5 V/cm. The mobility of electrons is generally greater than that of holes. For instance in silicon, electrons are around 3 times more mobile than holes. Holes will eventually saturate at the same velocity as electrons, although this will require a greater electric field of up to 10^6 V/cm.

The other main contribution to the carrier motion is diffusion. The thermal velocity of any individual carrier is random. However, if the carrier density is non-uniform then it is probable that carriers will move from regions of high density to regions of low density. The flux of the electrons (F_e) and holes (F_h) is given by,

$$F_e = -D_e \nabla n \qquad F_h = -D_h \nabla p, \tag{2.2}$$

where D_e and D_h are the diffusion coefficients for electrons and holes respectively. n and p are the numbers of electrons and holes per unit volume. Taking q to be the charge of

the carriers, the overall current density generated by the electrons (J_e) and holes (J_h) are therefore given by,

$$J_e = q\mu_e nE + qD_e\nabla n \qquad J_h = q\mu_h pE - qD_h\nabla p. \tag{2.3}$$

A pure silicon crystal forms what is called an intrinsic semiconductor. Here there are equal numbers of electrons in the conduction band as there are holes in the valence band because the electrons and holes are created in pairs. At a room temperature of 300 K, silicon typically has a carrier concentration of around 10^{10} cm^{-3}.

If atoms of a different type are added to the silicon crystal it is called doping. An extrinsic semiconductor can be created by adding atoms of either Group III or Group V. A Group V atom, such as phosphorus, has 5 valence electrons. This means that when its added to the silicon lattice an additional non-bonding electron is available for conduction. This new electron will sit at an energy level about 0.05 eV below the conduction band and can be easily excited at room temperature. Hence, this is referred to as the donor level. This will not leave a corresponding hole in the valence band. In a material such as this, electrons are the dominant charge carrier and the material is referred to as n-type. The addition of a Group III atom such as boron has the alternative effect. Here, an empty energy level called the acceptor level is created just above the valence band that a valence electron can be excited to. This creates holes in the valence band that can act as charge carriers. This type of material is referred to as p-type. Figure 2.3 shows a diagram with the additional energy levels of n-type and p-type semiconductors compared to an intrinsic semiconductor.

The concentration of dopant atoms is normally many orders of magnitude less than the concentration of silicon atoms. Crystalline silicon has approximately 5 x 10^{22} atoms/cm^3. The concentration of dopant atoms will typically vary from 10^{13} to 10^{18} atoms/cm^3. Very heavily doped silicon does have some uses though, particularly where electrical contacts need to be added to semiconductor devices. These heavily doped materials are denoted by n^+ and p^+ for donor and acceptor doping respectively.

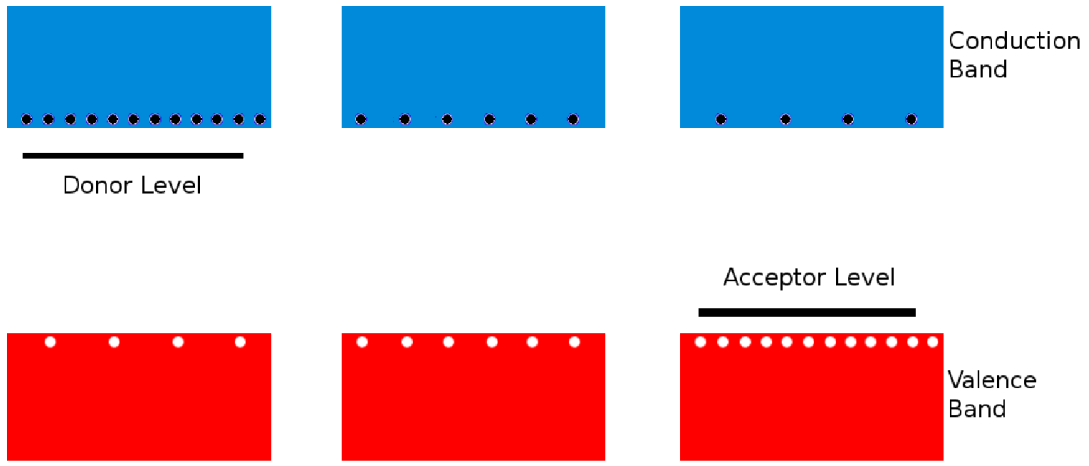

Figure 2.3: Example band gap diagram showing an n-type semiconductor (left), an intrinsic semiconductor (centre) and a p-type semiconductor (right).

2.2 Silicon Detectors

In Section 2.1 the basic properties of semiconductors, including n and p-type doping, were discussed. In this section, several different designs of semiconductor detectors will be explained. This will start with a simple p-n junction and then move on to more advanced designs. These will be the planar, 3D, Charge Coupled Device and CMOS devices.

2.2.1 P-N Junctions

The simplest type of semiconductor device is created by making a junction from an n-type and p-type silicon materials [17]. This is called a p-n junction, and can be seen in Figure 2.4. P-n junctions can form the basis of many more advanced radiation detectors.

The contact between p-type and n-type regions needs to be complete and continuous. Simply placing two doped pieces of silicon together will not suffice. The junction must have the two regions created in a single crystal structure during the fabrication process.

If the two regions are in thermal equilibrium, then the electrons will naturally diffuse to areas of lower concentration in the p-type material and the holes will diffuse to the n-type material. At the junction between the two regions the electrons and holes will recombine to create a small region with a lower concentration of charge carriers. This is called the depletion region. The donors and acceptors that are fixed at the lattice sites and therefore

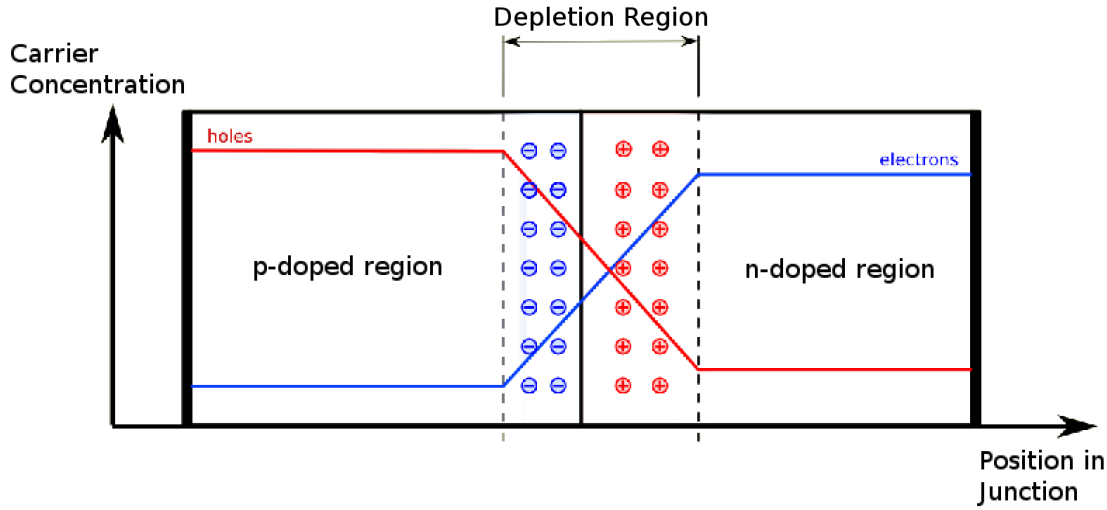

Figure 2.4: A p-n junction created from a p-type material (left) and an n-type material (right) with a depleted region in between. The junction shown here is in thermal equilibrium.

cannot move will create a small electric field that will produce carrier drift opposite to the direction of diffusion. If there is no external bias applied to the device, then there will be no net current flow.

The fixed charge within the depletion region will generate a built-in potential. The Fermi level of a material is defined as the highest occupied carrier energy level at absolute zero. By assuming that the Fermi levels in each half of the depletion region are equal, the built-in potential V_{bi} can be calculated,

$$V_{bi} = \frac{kT}{q} \ln \frac{N_a N_d}{n_i^2}, \tag{2.4}$$

where N_a and N_d are the concentrations of acceptors and donors; k is Boltzmann's constant; T is the temperature and n_i is the intrinsic concentration [18].

Taking as an example an abrupt p-n junction, with a carrier density of 10^{15} cm^{-3} and a temperature of 300 K, the built in potential is calculated as 0.60 V. The energy any individual charge carrier has from this built-in potential for silicon is 0.60 eV and is less than the band gap.

2.2.1.1 Biasing a P-N Junction

When a p-n junction is in equilibrium, the Fermi levels on either side of the junction are equal and there is no net migration of charge through the junction. A bias potential can be applied across this junction in one of two ways. Attaching a positive terminal to the p-type region and a negative terminal to the n-type region is called forward biasing the junction. Reversing the terminal positions would apply a reverse bias to the device.

When a p-n junction is forward biased, electrons will drift from the n-type region to the p-type where they will then recombine with the available holes. The electrons will drift with very little resistance to their motion. This has the overall effect of reducing the size of the depletion region and creating a large current.

Reverse biasing a p-n junction is the standard method to create a radiation detector. Since the depletion region contains relatively few free charge carriers, very little current will be generated initially. Instead, as the bias is increased the holes from the edge of the p-type region and electrons from the edge of the n-type region will begin to drift away from the depletion region. This will have the result of the depletion region widening. Once the electric field increases beyond a critical level, breakdown will occur in the device and current will begin to flow. If there was to be a simple, one-dimensional p-n junction and a bias of V_R was applied to it, then the width of the depletion region, w, would be,

$$w = \sqrt{\frac{2\epsilon_s(N_a + N_d)}{qN_aN_d}(V_R + V_{bi})}, \tag{2.5}$$

where ϵ_s is the permitivity of silicon and V_R + V_{bi} is the sum of the built in and applied biases [18]. Although the overall charge in the depletion region is zero, if one of regions of the junction has a lower concentration of dopant atoms then the depletion region will extend further into this region. The capacitance of a p-n junction, C_j, is inversely proportional to the width of the depletion region and is,

$$C_j = \frac{\epsilon_s}{w}. \tag{2.6}$$

The bias voltage required to create a depletion region equal to the thickness of the detector is called the full depletion voltage. If the detector is biased to a voltage above this value, then the detector is said to be overdepleted. Detectors will generally be operated at bias voltages just above the depletion voltage. The depletion voltage for a device can be calculated by measuring the change in capacitance against the bias voltage. A plot of C^{-2} against V for a diode will show a linear decrease in capacitance under reverse biasing and then a plateau in the capacitance. The full depletion voltage is defined by convention to be the turning point in this graph. An example of this is shown in Figure 2.5.

The full depletion voltage increases with the square of the thickness of a detector and in proportion to the absolute value of the effective doping concentration. For a further discussion of the effects doping has on the depletion voltage, see Section 2.3.6.2.

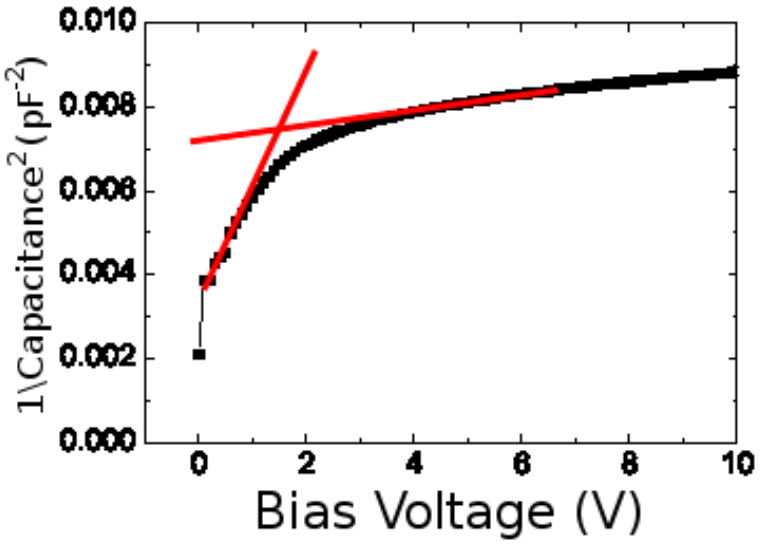

Figure 2.5: Example of a CV curve for a diode with an electrode spacing of 40 μm. The red lines indicate the linear regimes that give the full depletion voltage.

2.2.1.2 P-I-N Diodes

A further level of complexity can be added to a p-n junction by inserting a near-intrinsic layer (the i-region) in between the p and n regions [15]. For many practical applications, this intrinsic layer will often be approximated by a high resistivity n or p-layer. The advantages of p-i-n diodes over basic p-n diodes are that the capacitance is low and constant; when reverse

biased the breakdown voltage is relatively high and when forward biased the device operates as a variable resistor.

The intrinsic layer, even if lightly doped, will be fully depleted with a low reverse bias. After full depletion, the capacitance is independent of the bias voltage and the breakdown voltage can be estimated to be proportional to the width of the intrinsic region. These characteristics are desirable for photodetectors and hence, p-i-n diodes are typically preferred over p-n diodes.

2.2.2 Planar Detectors

The use of p-n and p-i-n junctions in radiation detection allowed many advantages to be accrued [19]. For instance, solid-state detectors can have physical dimensions many orders smaller than equivalent gas-state detectors and an energy resolution much greater than scintillating detectors. Further developments to the standard p-i-n junction have produced detectors with improved characteristics [20].

The primary ionisation mechanisms in a semiconductor are proportional to the energy loss of the incident radiation [21]. This allows for energy sensitive detectors, based on semiconductor technology, to be developed relatively easily. Simple photodiodes based on p-n junctions will allow the energy of detected radiation to be determined. Discovering where in a detector the radiation interacted with the semiconductor is more difficult. Rather than employing a single p-n junction to collect deposited charge, the detector will be split into many smaller sub-detectors. These can then operate semi-independently to collect and read out charge created within their boundaries.

The physical limit of the precision of a position measurement depends on the information recorded by the detector. If a simple binary readout is employed, where a pixel reports either being hit or not, and the measured hit position is taken to be the centre of the pixel or strip and there is no charge sharing, then the root-mean-square deviation from the actual hit position (x) is given by,

$$\sqrt{\langle \Delta x^2 \rangle} = \sqrt{\frac{1}{p}\int_{-p/2}^{p/2} x^2 dx} = \frac{p}{\sqrt{12}}, \tag{2.7}$$

where p is the pitch of the device. Charge sharing between pixels, either from diffusion or from the angle of the incident radiation, will improve the resolution. An analogue readout that records the amount of charge deposited in neighbouring pixels can have greater precision by using, for example, a centre of mass calculation. Analogue readout will be advantageous for measurements where the average charge diffusion is greater than the pitch. Where the diffusion is less than the pitch, there will be no advantage to the precision [22].

The first position sensitive silicon detectors created were microstrip devices for use in vertex telescopes [23]. The first detectors were single-sided, in that they had highly doped electrodes on only one surface. This would then measure the induced current from the electrons. A further improvement was the use of detectors with a double-sided readout. A double-sided readout system has highly doped electrodes on opposing surfaces and measures the current induced from both types of carrier. An example of a planar device is shown in Figure 2.6. In this example, the position of the metallisation, the passivation and the highly doped regions for a p-on-n detector are shown.

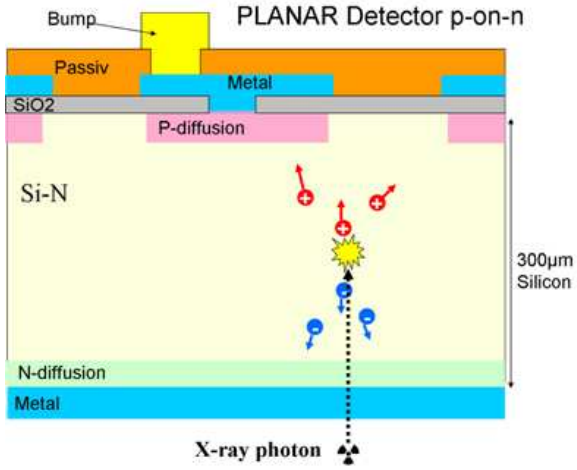

Figure 2.6: A schematic of a Planar, pixel detector [24]. An example of the drift of electrons and holes is shown along with some characteristic dimensions. The detector will be DC-coupled to the amplifier.

The semiconductor industry created newer fabrication techniques in the desire to produce integrated circuits. Some of these new techniques, such as ion implantation and photolithog-

raphy, have been adapted for use in detector fabrication. This allowed the creation of new, passivated planar detectors. The advantage of using techniques from the semiconductor industry was that they lend themselves to large-scale batch processes providing cost benefits, and can generate the potentially complicated electrode geometries on a silicon wafer.

The fabrication of devices via the planar process involves a combination of passivations, photolithographic patterning and doping [25]. Initially, a silicon wafer of high purity is manufactured. This will often be lightly n-type due to the small concentrations of donor impurities. Then, once the wafer has been polished and cleaned the passification process begins. During passification, the surface of the silicon is heated and coated with an oxide layer. This is performed by passing an oxygen stream over the wafer within high purity quartz tubes at 1030 °C [25].

After that, photolithographic techniques are employed to remove regions of the oxide layer. The first step in this stage of the process is to coat the wafer in 1 to 2 μm of a photoresist by using a spinning machine. After a softbaking process, a mask is used to cover the portions of the resist that must remain and the rest is stripped. The resist is then hardbaked and the exposed SiO_2 is etched using HF. In the final step, the resist is removed either by plasma stripping or chemically. These etched areas will later form the junctions in the silicon. Structures as small as 40 nm can be created with optical lithography [26].

The area within these windows is doped with acceptor ions in a thin layer of 1 or 2 μm into the silicon. The opposite surface is then implanted with donor ions, making it into n^+ silicon. The wafer is then annealed to repair some of the radiation damage that the implantation ions may have caused. Lastly, photolithographic techniques are again employed to deposit aluminium, electrical contacts for the front and back-side. Thicker layers of aluminium will decrease the energy resolution of the detector, so the metalisation is kept as thin as possible.

2.2.2.1 Slim Edge Technology

In a standard detector, there will typically be a series of guard ring structures surrounding the detector. These structures will gradually decrease the potential across a larger distance

to reduce the noise generated. The main disadvantage this technology introduces is the loss of up to a millimeter of active silicon all around the sensor.

If an actively biased area of a detector is directly adjacent to the cut edge of the device, then there will be a large potential difference. This is because the cut edge will provide a leakage pathway around the device. This will then generate a large current and consequently a large source of noise and increased heat to be dissipated. However, large area imaging [27] where multiple detectors are required to be tiled together would have a loss of signal in the dead areas between the detectors.

One solution to this problem is through the use of slim edge technology. By utilising slim edge technologies the dead area around a detector can be reduced from over 500 μm to less than 100 μm [28]. This will have no effect on applications where the area needed to be imaged is can be fitted within a single sensor. There are multiple techniques within this category, but they all result in the reduction in size of the dead area [29]. One design of slim edge detectors involves heavily doping the edge and bottom of the device whilst retaining the standard planar diode junction on the top of the device. The downside to this is that the corners of the detector far away from the junction electrodes will require very high bias voltages to fully deplete.

Another method, particularly applicable to 3D detectors, is to design the detector to have a full 3D column at the edge to contain the electric field [30]. Alternatively, an oxide layer could be used instead of the edge polysilicon. This would have the advantage of increasing the radiation hardness. Examples of these slim edge technologies are shown in Figure 2.7.

2.2.3 3D Detectors

As particle colliders increase their luminosity, there will need to be an increase in the radiation hardness of their detectors [31]. In 1999, a new design of detector was proposed that would possibly be an improvement over traditional planar detectors in a number of areas [32] [8] [30]. Ion implanting can only create doped layers in the few micrometers closest to a surface. By employing micromachining techniques it is possible to create long columns, of

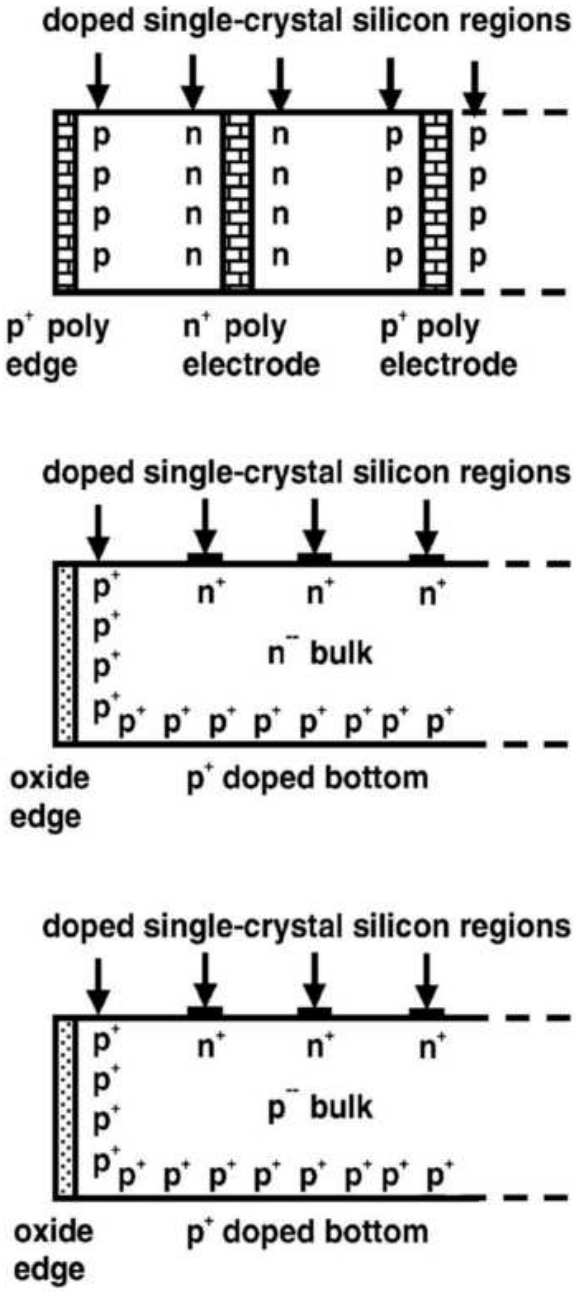

Figure 2.7: Examples of various slim edge technologies [29]. The top example shows a device with full 3D columns. The middle and bottom examples are of planar devices with a heavily doped edge and bottom and either an n-type or p-type bulk.

alternating n^+ and p^+, that penetrate through the bulk of a silicon crystal. A schematic of this design is shown in Figure 2.8. One half of the columns would be connected to the readout electronics and the other half would be used to bias the device. Typically, to form quadrilateral pixels, one readout column will be at the centre of the pixel and four bias columns will be at the corners of each pixel, although other geometries have been developed more recently

[33].

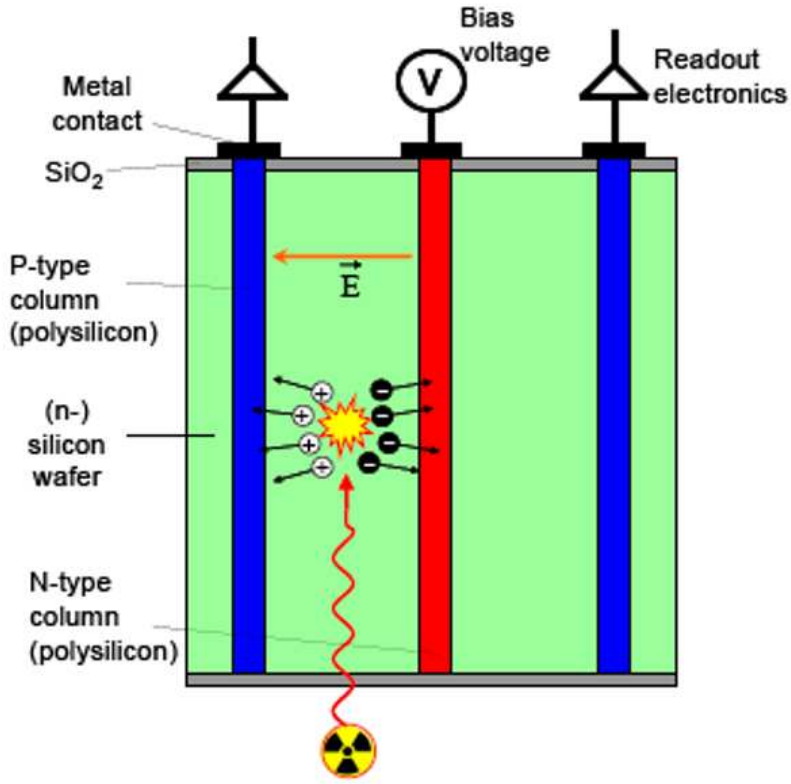

Figure 2.8: A schematic of a full-3D detector. An example of the drift of electrons and holes is shown.

In a planar device, the thickness of the silicon determines the drift time of carriers and the depletion characteristics. In the novel 3D design it is the spacing between the columns that will define the drift times and the depletion voltage. Depletion of the sensor will occur laterally, between the columns as opposed to the vertical depletion of a planar sensor. The depletion distance (and hence the collection distance) is dependent on the column pitch rather than the thickness of the device. The pitch can then be less than the thickness. Therefore, a planar device and a 3D device of the same thickness will collect the same quantity of charge from a MIP, but the 3D device will have the readout electrodes much closer together.

Another advantage is that the shorter distances between electrodes will produce a greater electric field. This means that charge carriers will undergo less trapping before collection after radiation damage. The overall effect should be to ensure that the detector is more radiation hard than similar planar devices.

The electrode structure of the 3D design defines an electric field within the substrate that differs from that of the planar sensor. In the planar design charge created in the substrate drifts through the substrate thickness towards the collecting electrodes on the surface of the device. This allows time for the charge cloud to spread laterally by diffusion, leading to a greater probability that the charge will be collected across multiple pixels. The electric field in the 3D design drifts charge parallel to the substrate surface, towards the collecting electrode in each pixel cell. This reduces the charge sharing in the detector which is advantageous to X-ray imaging applications. In imaging applications, where photon counting is used, charge sharing can lead to multiple counts or no counts for a single photon depending on the threshold thus reducing the image quality.

There are disadvantages to reducing charge sharing. For example, charge sharing is necessary to improve position resolutions using centre-of-mass calculations.

The 3D electrode structure has a self-shielding geometry which reduces the required guard ring area and can also allow for active edge technology [34] to be applied. Consequently, the size of the insensitive region around the sensor can be reduced to a few microns. This is important in large area detectors where multiple sensor substrates are tiled together. The possibility to cover large detection areas with minimal dead area, the fast collection times and the reduction in charge sharing makes 3D detector designs attractive for application in synchrotron X-ray experiments as well as high energy physics. Typical synchrotron experiments are described in Chapter 5.

The main disadvantage to 3D detector designs is the complexity of the fabrication process, and this will be discussed later. Another disadvantage is that the columns are non-active. The electric field within the columns is negligible so any charge produced there will not be collected. Finally, the close electrode spacing will create a large capacitance in the device which can lead to greater noise in the front-end amplifier than in a typical planar device.

The first true 3D detectors produced were called full 3D as they had n-type and p-type columns that passed completely through the silicon from the front-side to the back-side.

These columns were fabricated from the same side, and in order for the processing to work a handle wafer would be bonded to the silicon wafer [35]. The use of the handling wafer increases the complexity, and hence cost, and reduces the reliability of the fabrication process.

An alternative to this is the use of double-sided 3D detectors. In this design of detector the columns do not pass the entire way through the silicon substrate. Instead, the n-type columns extend from one side and the p-type columns extend from the other. Figure 2.9 displays an example of a double-sided 3D p-type detector. The p-type and n-type columns are shown along with the passivation, metallisation and p-stops. During fabrication, a double-sided detector does not require a handling wafer so the reliability of the fabrication process is improved compared to a full 3D device.

The region of the double-sided 3D device where the columns overlap depletes latterly in the same way the full 3D device would. However, the regions beyond the end of either of the columns will require a far greater bias voltage to deplete than the lateral depletion. Consequently, when quoting the depletion voltage for a 3D device typically two voltages will be stated. These are the lateral depletion in the overlap region and the depletion beneath the columns.

The fabrication of full and double-sided 3D detectors is similar, except that the depth of the columns must be accurately controlled for the double-sided and it has no requirement for a handle wafer [36]. The fabrication process adds micromachining techniques to those used for planar devices [37].

The first stages of the fabrication are identical to that of a planar device. After the photoresist and the photolithography is completed however, holes for the columns are etched. Using either dry etching or wet chemical etching techniques are possible, but a dry etching technique such as inductively coupled plasma grants greater control and homogeneity of the electrodes [37]. Cycles of etching and passivations are performed because long etching stages would cause etching to occur in orthogonal directions to the column.

The maximum depth that a column can be etched is limited by the etching machine's limited aspect ratio for etched structures. The ideal column design would be as thin as

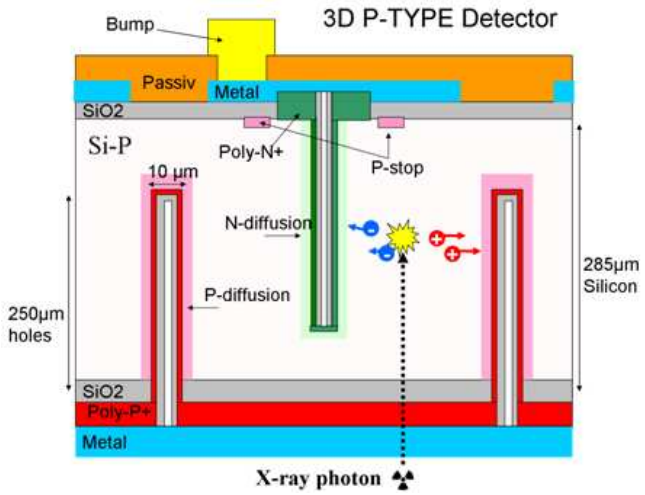

Figure 2.9: A schematic of a double-sided 3D p-type detector [24]. An example of the drift of electrons and holes is shown along with some characteristic dimensions.

possible. Reducing the width is advantageous because the column is non-collecting and so a reduction in the dead area is desirable. However, a longer column will reduce the collection time for charge in the device as there will be a greater amount of overlap between the columns of opposite type. Extending the columns fully through the device will create a dead area where no signal will be collected. For these reasons, a typical silicon detector with a thickness of 300 µm might aim to have columns around 10 µm wide and 250 µm deep.

Once the holes are formed, they are coated with a layer of polysilicon and doped appropriately. The polysilicon layer at the surface of the substrate is then etched and passivated and metalised as with a planar device.

2.2.4 Charge Couped Devices

The charge coupled device (CCD) was invented in 1969 by Boyle and Smith at the Bell Telephone Laboratories [38]. The invention of the CCD moved photographic imaging away from film and towards solid-state devices. This had a profound effect on scientific imaging [39].

Originally, CCDs were developed as a means of storing data in a solid state device. In order for a device to function as a memory storage device, there needs to be a way of reading the presence or absence of data bits and the ability to create and destroy these bits. In a CCD,

a bit of information is represented as a packet of charge carriers in the depletion region of a metal-oxide-semiconductor (MOS) capacitor. By placing multiple MOS capacitors in close proximity, it is possible to control the flow of charge through several capacitors by altering the bias voltages on the gate's of the capacitors independently. An amplifier at the end of the series of capacitors can convert the presence of a charge packet into an output voltage, allowing the data to be read. In its original function as a memory storage device the initial charge would be generated using an input diode. However, as shown in Section 2.3, charge can be generated optically as well [40] [41].

There are many different designs of devices that fit into the category of CCDs. Perhaps the simplest design conceptually, and the original design [42], uses three phases of gates to pass charge from one pixel to the next. Each pixel consists of three gates in parallel and every third gate is driven by the same clock driver. Each column of pixels is separated from its neighbours by means of potential barriers. Every time the charge packets move three gates further down the chain, the pixels at the bottom of the columns are read out horizontally by a series register. By this method, the entire device is read out a line at a time. This process is shown in the schematic in Figure 2.10(a). Figure 2.10(b) shows a cross-section of a front-illuminated CCD with regions of different doping concentrations highlighted.

The are four primary operations that a CCD must be able to complete in order to create a full image. These are generating the charge; collecting the charge in packets; transferring the packets down the columns; and measuring the charge.

Firstly, charge generation is the process by which incident photons are converted into electron-hole pairs. A fundamental characteristic of CCDs is their quantum efficiency. The quantum efficiency of a CCD is the percentage of energy from incoming photons that is captured as charge in the device. It is strongly dependent on the wavelength of the incoming light, with the efficiency decaying for both high and low energy photons. Photons with a wavelength greater than approximately 1090 nm will not have enough energy to create electron-hole pairs. A typical CCD's response will normally peak at wavelengths of around 650 nm [45]. UV photons with wavelengths of 300 nm to around 100 nm will often not be

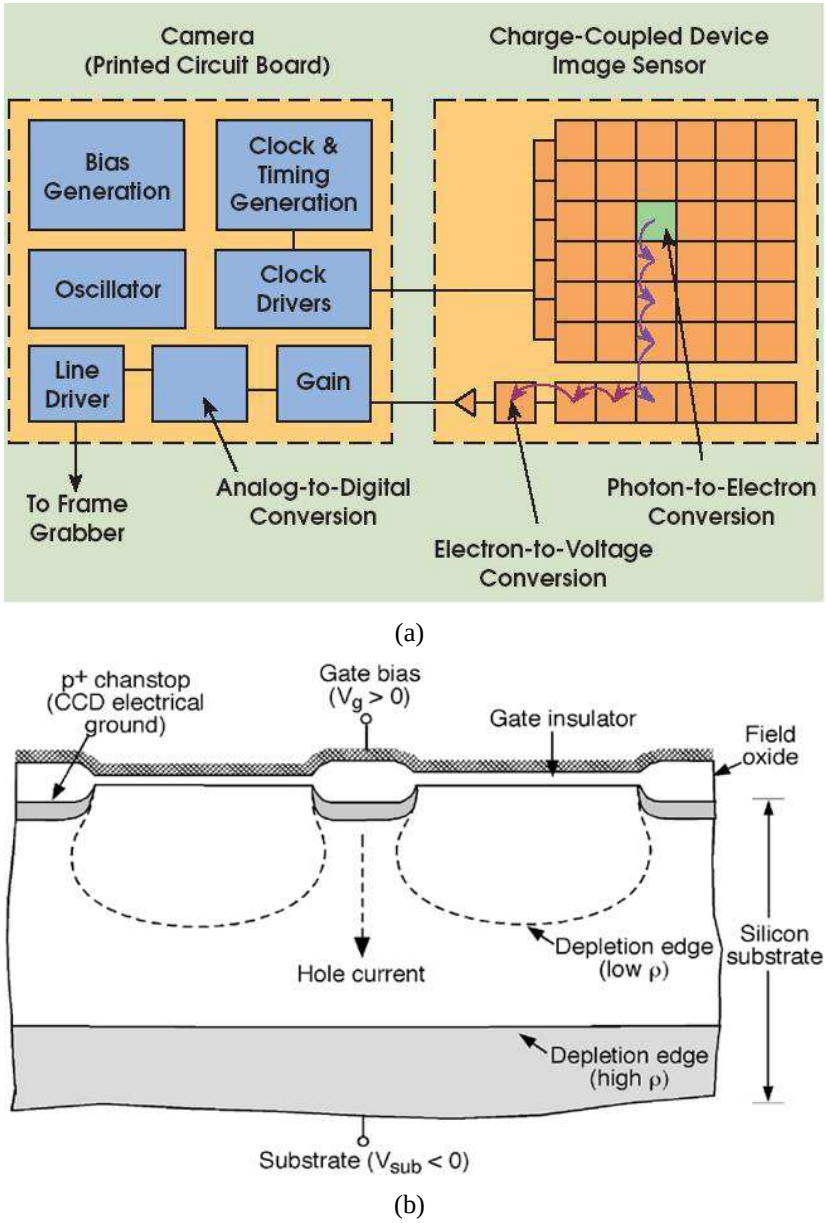

Figure 2.10: (a) A schematic of the transfer of signal down each column [43] and (b) the cross section of a generic CCD ©2004 IEEE [44].

detected due to the photons not penetrating far enough into the silicon. X-ray photons with wavelengths of 1 nm (1.24 keV) and less will start to be detected again due to the penetration depth of these X-rays increasing enough to enter the depletion region. The absorption coefficient of photons is strongly correlated to the atomic number of the medium.

There are techniques that can be used to increase the sensitivity of a CCD to photons in the blue and UV ranges. One method is to coat the surface of the device with a phosphor that will re-emit a lower energy photon when a UV photon interacts with it. These newly

created photons will be emitted in a random direction so some position resolution will be lost as well as energy resolution and half of the photons will escape detection entirely. This was the method used to increase the sensitive range of the Hubble telescope [46]. Another more expensive method is through two processes known as back-thinning and back-side illumination. Rather than illuminating the front-side of the CCD, where photons can be lost by interactions with the gate structures and electronics, the silicon on the back-side is directly interacted with. However, thick back-side substrates will not allow charge to be generated close enough to the gates be collected efficiently. Therefore, the back-side of the CCD is thinned [47].

The second important operation of a CCD is collecting the charge generated into packets. The collection of the electrons is based on their diffusion. This operation is performed within each pixel of a CCD. There are a number of features of the pixels that dictate the effectiveness of this process. These are the number of signal electrons that a pixel can hold prior to saturation and the ability of the pixel to collect the signal electrons generated. The maximum number of signal electrons that a pixel can measure at once is called the full-well capacity and is fundamentally constrained by the size of the pixel. Larger pixels can hold more charge, but also allow for less position sensitivity. The greater the full-well capacity the better the signal-to-noise performance and the dynamic range. The dynamic range of a device is the ratio of the largest and smallest signals that can be measured simultaneously. The diffusion of electrons to neighbouring pixels will prevent a single pixel collecting all the charge generated within it. CCDs designed for a specific range of energies of photons will normally have substrate thicknesses such that the electrons are generated close to the collection architecture. Reducing the cross-talk between pixels is key to improving this stage of the CCD's readout.

The third operation is transferring the charge down the column in which it was captured. This is achieved through modifying the voltages on the sequence of gates that make up the vertical registers. Every time a pixel passes its charge to the neighbouring pixel there is a small chance some of the signal will be lost. A modern CCD can have many thousand pixels in each column, so a signal from the pixel farthest away from the horizontal register needs

to be transferred thousands of times successfully before its read out. The efficiency of this operation is improved by increasing the time allowed to move each pixel's charge down the register. CCDs employed in optical photography may only take one frame a second. These will generally have much higher charge transfer efficiencies compared to CCDs used, for example, in biological applications that may take a thousand frames a second.

The final operation is measuring the charge produced. This is achieved by dumping the outputted charge onto a capacitor linked to a MOSFET amplifier. This amplifier then generates a voltage for each pixel proportional to the signal charge registered.

2.2.5 CMOS Active Pixel Sensors

Complementary Metal Oxide Semiconductor (CMOS) Active Pixel Sensors (APS) are a class of imaging devices, developed in order to improve upon some aspects of the CCD design [48]. One of the major technological difficulties that CCDs have is their need for almost perfect charge transfer between pixels during readout. This makes it difficult for CCDs to be integrated with on-chip electronics associated with miniaturisation. Another problem is the limit this places on the readout rate.

The miniaturising of instrumentation demands that circuitry be integrated into the on-chip electronics. The analogue to digital conversion of a signal is a feature that is possible with CMOS designs. However, the standard CCD design is not compatible with CMOS electronics. Furthermore, CCDs generally require high voltages at the transfer gates that can cause an increase in the leakage current of the device.

An APS device has one or more transistors integrated into the pixel architecture. This assists in both buffering the photosignal and driving the readout. This technology also allows for random-access to pixels. The power dissipated in an APS is less than that of an equivalent CCD. This is because in order to read out any single pixel in the array, the CCD requires every other pixel to be active as well. Sensitivity, read noise and dynamic range can be designed to be comparable to a similar CCD. CCDs were initially an attractive design because they required only three electrodes per pixel. As the semiconductor industry improved

microlithography techniques to the sub-micron regime, the quantity of electronics that could be fabricated on a single pixel were increased.

The addition of extra circuitry can provide a source of functionality, performance and also complexity [49]. Separating the photodiode and the source follower gates with a transfer gate maintains the photodiode at a constant potential and reduces the capacitance [50]. This is called a 4T CMOS design. This has the overall negative effect of increasing the output conversion gain. A 4T CMOS pixel can achieve lower noise and a higher conversion gain for an increased sensitivity to small amounts of charge compared to the simpler 3T pixel.

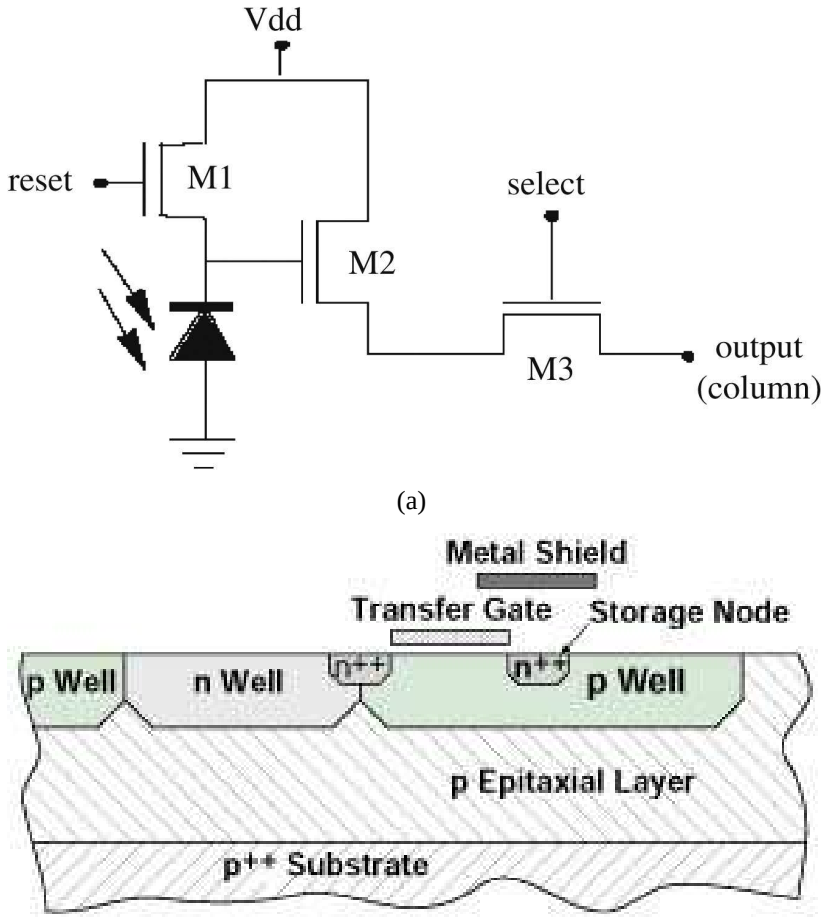

Figure 2.11: (a) A schematic of a generic CMOS APS device with three transistors [51] and (b) a cross sectional view of an APS pixel depicting features that would give rise to an electric field that would prevent leakage.

The schematic shown in Figure 2.11(a) is of a generic CMOS APS device with three transistors in each pixel. Each of the three transistors has a separate function on the pixel.

The first (M1) resets the photoelement, the second (M2) converts the accumulated charge to a voltage and the third (M3) selects which row is to be read. The main difference compared with how a CCD operates is that the charge to voltage conversion is contained within each individual pixel and they can be read out independently. As with CCDs, the collection of the electrons is based on diffusion rather than drift. Figure 2.11(b) shows the cross section of a CMOS APS pixel.

There are downsides caused by the APS design. The pixel architecture creates a pixel-to-pixel variation across the sensor. This results in an increase in fixed pattern noise. This effect is discussed more fully in Chapter 5. Correlated double sampling can be used to minimise the fixed pattern noise. This is a noise reduction technique where the voltage after a pixel is reset is subtracted from the voltage at the end of the integration time. However, additional memory will be needed to store the offset information.

2.3 Ionising Radiation

Any radiation that has the potential to ionise electrons in the bulk of a semiconductor substrate can be detected. These can generally be split into two broad categories each with two sub-categories. Firstly, charged particles continuously act on the electrons in any medium through which they are traveling via the Coulomb effect. These can either be heavy charged particles such as protons or pions, or lighter charged particles such as fast electrons. Secondly, uncharged radiation can also ionise electrons in a medium, but must first undergo an interaction that deposits most of the radiation's energy at a single point. Photons will excite secondary electrons when they deposit their energy that are similar in properties to fast electrons. Neutrons can only be detected after interactions with lattice nuclei generate heavy charged particles.

For the purposes of this thesis, interactions involving heavy charged particles and photons are of the greatest importance.

2.3.1 Charged Radiation: Heavy, Charged Particles

Heavy, charged particles are generally considered to have a mass exceeding that of an electron. This includes particles such as the muon, pion, kaon and proton. Positively and negatively charged particles are considered to have similar effects. They will primarily interact with the medium they travel through via a Coulomb interaction between the particle and the medium's electrons. Rarer interactions such as Rutherford scattering from the nuclei are also possible. These interactions do not occur frequently enough for a detector to reliably detect particles based on them.

The Coulomb interaction is based on an inverse square law relationship of the distances between interacting charges. The charged radiation will, therefore, interact simultaneously with many electrons. The force imparted upon the electron may be great enough to excite it to a higher energy level, or to completely ionise it from the atom. The energy gained by the electron is compensated for by an equivalent loss in energy in the charged radiation. The energy lost in any single encounter will be a small fraction of the total energy, however, due to the large number of encounters occurring near simultaneously the charged radiation's velocity will continually decrease. The electrons that the radiation is interacting with will normally be spaced homogeneously around it. This means there will not be large deflections in the direction of travel, unless caused by a rarer nucleic interaction.

Occasionally, an ionised electron may have enough energy to ionise further electrons. These electrons are referred to as a delta electrons. A delta electron will undergo scattering far more regularly than it's parent radiation, and will consequently have a much shorter range.

The linear stopping power of a medium with a charged particle is equal to the mean rate of energy loss and is defined by the Bethe-Bloch formula [52],

$$S \equiv -\frac{dE}{dx} = Kz^2\frac{Z}{A}\frac{1}{\beta^2}\left[\frac{1}{2}\ln\frac{2m_e c^2\beta^2\gamma^2 T_{max}}{I^2} - \beta^2 - \frac{\delta}{2}\right], \tag{2.8}$$

where S is the stopping power; K is a constant; z is the charge number of the particle; Z and A are the atomic number and atomic mass of the medium; β and γ are the standard relativistic functions; $m_e c^2$ is the electron's rest mass; I is the mean excitation energy in eV;

T_{max} is the maximum kinetic energy that can be given to an electron in a single collision and δ is the density effect correction to ionisation energy loss.

This equation provides an accuracy of around 1% for a pion passing through a copper medium, providing the pion has an energy between 6 MeV and 6 GeV. At greater energies, the radiative effects become more pronounced. At lower energies C/Z corrections have to be made for tightly bound valence electrons where C is a correction term dependent on the electron's energy shell. The energy limits vary depending on the particle and the medium involved.

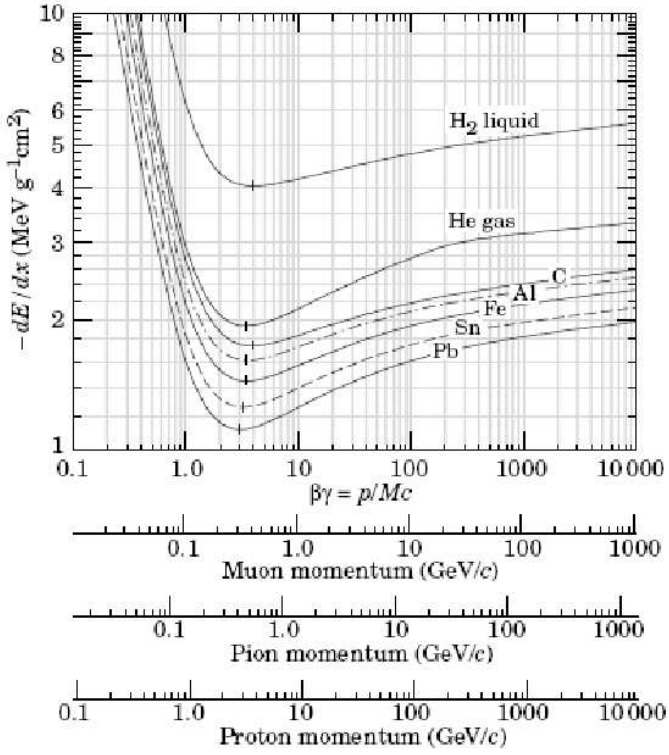

Figure 2.12: Mean energy loss rate through ionisation divided by the medium's density for a range of media and particles [52].

The curve associated with this formula can be seen in Figure 2.12. This shows the stopping power against the particle momentum for a variety of different particles and absorbing media. It can be seen that there is a momentum where the energy loss reaches a minimum. A particle with an energy loss close to the minimum value is called a Minimum Ionising Particle or MIP. For the thicknesses of detectors considered in this thesis, a MIP can be con-

sidered to pass through the full depth of the detector with its momentum and direction of travel unaffected.

The range of a particle is defined as the mean distance it travels within a medium before losing all its energy. For a particle that has the majority of its energy loss from ionisation effects, the integral of Equation 2.8 gives a good approximation of this value. At higher energies, where radiative effects begin to dominate, corrections to the integral have to be applied [53]. For a pion, this upper limit corresponds to around 100 GeV.

2.3.2 Charged Radiation: Fast Electrons

Compared to heavier charged particles, fast electrons and positrons have lower average energy losses but a far greater rate of scattering. The large scattering is due to the mass of the particle being the same as that of the orbital electrons being interacted with and, consequently, a greater proportion of the particle's energy can be lost in a single interaction.

Another difference between fast electrons and their heavier counterparts is the addition of radiative losses at all energies. Any acceleration of an electron must be associated with bremsstrahlung radiation. The change of direction from a scattering event is considered to be an acceleration. Typical bremsstrahlung radiation will normally be re-absorbed fairly close to the point of origin due to the relatively low energies involved. This radiative loss in energy adds an additional term to Equation 2.8 [20] of,

$$-\left(\frac{dE}{dx}\right)_r = K\frac{EZ(Z+1)e^4}{137m_e^2c^4}\left[4\ln\frac{2E}{m_ec^2}-\frac{4}{3}\right], \tag{2.9}$$

where E is the energy of the electron.

All the features of fast electrons also apply to positrons traveling through a medium. Positrons can also be stopped via annihilation with an orbital electron. This will release a 0.511 MeV photon that can travel a large distance from its creation point before being re-adsorbed.

2.3.3 Uncharged Radiation: Photons

Photons undergo markedly different interactions compared to charged particles. Instead of slowing down gradually with continuous and simultaneous interactions with the medium, photons lose their energy in a single interaction. This can be through a variety of processes, either photoelectric adsorption, Compton scattering or pair production. Low energy photons will interact predominantly via photoelectric adsorption and high energy photons via pair production. The relative cross sections for different energies of photons and absorber atomic numbers are shown in Figure 2.13.

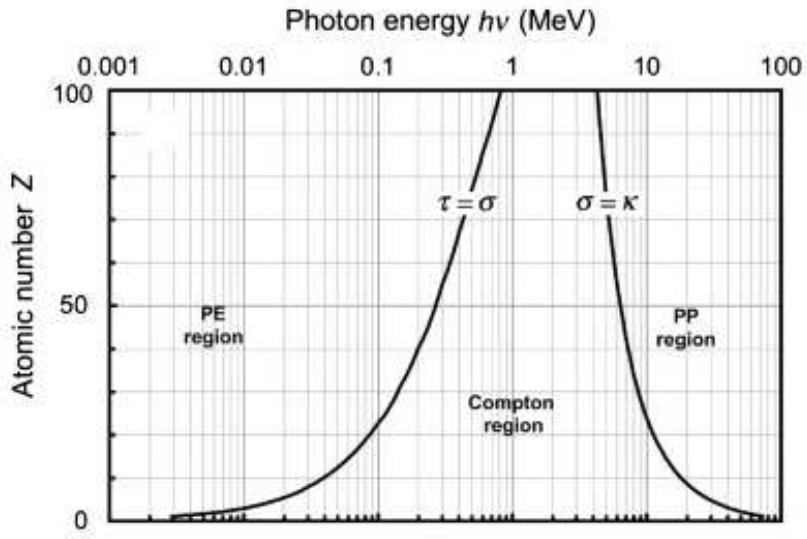

Figure 2.13: Representation of the relative predominance of the three main processes of photon interaction with absorber atom: photoelectric effect (τ), the Compton effect (σ), and pair production (κ) for adsorber atomic number (Z) against photon energy ($h\nu$). The two curves in connect points where photoelectric and Compton cross sections are equal shown by the curve on the left and Compton and pair production cross sections are equal shown by the curve on the right [54].

Photoelectric adsorption occurs when the photon interacts with an atom in the medium, ionising the atom and creating a photoelectron. The energy of the photoelectron is simply the energy of the original photon less the binding energy of the electron. Due to this interaction being with the atom as a whole, the photoelectron released is typically from one of the lower, tightly bound energy levels. This interaction can also only occur with an atom, not with a free electron because of conservation of momentum. After ionisation, the newly-formed

electron vacancy may either be filled by the capture of a free electron or the de-excitation of a higher energy electron in the atom. This process can create further X-rays with specific characteristics based on the atom. If the secondary photon escapes the detector, only part of the energy of the original photon can be detected. The photoelectron created behaves in a manner similar to the fast electrons discussed in Section 2.3.2.

Compton scattering is a process whereby a photon transfers part of its energy to an electron and deviates in the process. Assuming the electron begins at rest, any angle of scattering is possible. Therefore, the energy transfered from photon to electron can be any proportion of the photon's initial energy.

The rest mass of an electron and positron is 0.511 MeV. If a photon has an energy greater than 1.02 MeV then pair production is possible. Pair production becomes increasingly likely as the energy of the photon increases above 1.02 MeV. Any excess energy from the initial photon will be converted into kinetic energy for the electron and positron. The electron and the positron will generally undergo further scattering events and annihilation, producing further photons. The detection of this subsequent radiation is important in the design of detectors for high energy radiation.

2.3.4 Uncharged Radiation: Neutrons

Neutrons, whether slow or fast, can only interact with the nuclei of the medium in which they travel. No Coulomb or photoelectron interactions are possible. Unlike photons, the secondary radiation from neutron interactions tend to be heavy charged particles - either the nuclei themselves given sufficient energy, or the result of nuclear reactions.

Standard neutron detectors will normally use a converter to turn the neutrons into protons that can then be detected.

2.3.5 Signal Formation

Ionising radiation can create a signal on collecting electrodes. Electron-hole pairs generated in the depleted region of a detector will induce a current as a result of the external electric

field [55]. The current that is induced can be determined through Ramo's theorem [56],

$$i = qv \cdot E_w, \tag{2.10}$$

where i is the induced current, q is the charge generated with a velocity v and E_w is the weighting electric field dV_w/dx where V_w is the weighting potential. The weighting potential can be calculated for any electrode in a particular geometry by setting the potential of the electrode in question to 1 V and the potential of all other electrodes to 0 V, and then solving Poisson's Equation.

The initial velocity of charge carriers can be determined using Equation 2.1. For a simple detector with parallel electrodes on the opposite sides of silicon with a thickness of d and a reverse bias V_0, the velocity becomes,

$$v = \mu \frac{V_0}{d}, \tag{2.11}$$

and the weighting field is,

$$E_w = \frac{1}{d}. \tag{2.12}$$

Therefore, from Equation 2.10, the induced current will be,

$$i = q\mu \frac{V_0}{d^2}. \tag{2.13}$$

The total charge that is induced on the collecting electrode will then be the integral of Equation 2.13. Using the simple model of an electron-hole pair created in a reverse biased diode, a distance x from the positively biased n-type electrode and $d - x$ from the negatively biased p-type electrode with velocities proportional to the electric field, the time for collection for the electron (t_e) and the hole (t_h) will be given as,

$$t_e = \frac{xd}{\mu_e V_0} \qquad t_h = \frac{(d-x)d}{\mu_h V_0}. \tag{2.14}$$

The total charge due to the electrons (Q_e) and holes (Q_h) can then be expressed as,

$$\begin{aligned} Q_e &= i_e t_e & Q_h &= i_h t_h \\ &= q\mu_e \frac{V_0}{d^2} \frac{xd}{\mu_e V_0} & &= q\mu_h \frac{V_0}{d^2} \frac{(d-x)d}{\mu_h V_0} \\ &= q\frac{x}{d} & &= q\left(1 - \frac{x}{d}\right). \end{aligned} \tag{2.15}$$

From these equations, it can be seen that the sum of the charge induced by either the electrons or the holes is dependent on the distance the charge was generated from the electrode. Also, in the initial stages of charge collection the signal will often be dominated by the collection of electrons because the mobility of electrons is around three times greater than holes in silicon. The electrical signal that results is not simply produced when the charge carrier is collected at the electrode. The signal is generated by the drift of a carrier in the electric field [57].

The example detector used above had parallel electrodes and infinite size. In this situation, the weighting potential is linear and inversely proportional to the distance between the electrodes. In a more realistic case, where the electrodes have a finite size similar to or less than the width of the device - such as the pixel detector in Figure 2.14(a) or the 3D detector in Figure 2.14(b), the weighting field will be non-uniform. Here, the weighting field will approach zero in the majority of the detector and the non-zero portion will be centred around the collecting electrode. This has the resulting effect that the majority of the signal is induced by the motion of carriers closest to the electrodes and carriers moving to the non-collecting electrodes produce little signal. The electrodes for the planar simulation were 20 μm wide and 60 μm apart. For the 3D detector, the electrodes were 10 μm wide, 250 μm deep and 40 μm apart.

When originally derived, independently by Ramo [56] and Shockley [59], the electrodes were considered to exist in a vacuum such as there might be in a vacuum tube. It can also be shown that Ramo's theorem still applies in a non-vacuum environment where there is a fixed

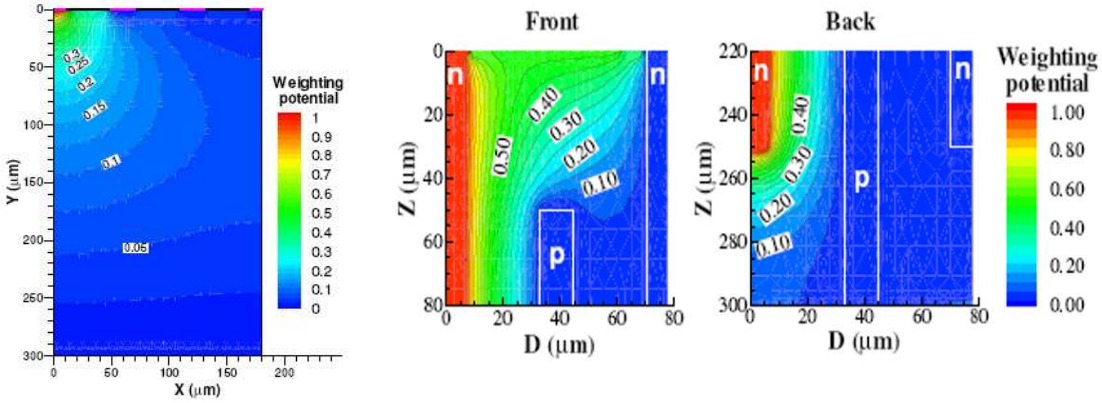

(a) (b)

Figure 2.14: Simulations of weighting fields for (a) an n-on-p planar strip detector and (b) a double-sided 3D strip detector [58]. For each simulation, a single electrode was considered to be read out. The electrodes for the planar simulation were 20 μm wide and 60 μm apart. For the 3D detector, the electrodes were 10 μm wide, 250 μm deep and 40 μm apart.

space charge present and also where there is a fixed magnetic field [60].

2.3.6 Radiation Damage

Pairs of electrons and holes created in the bulk of the semiconductor will often recombine, leaving no permanent damage. On the other hand, if these pairs are created in the oxide layer of a detector then they will often drift to the edges before recombination can occur. The electrons will drift from the oxide layer to the bulk silicon, typically in a time on the order of 100 ps. The holes will drift towards the metal contact, however their lower mobility may lead to them being trapped in the oxide layer. The result of this can be a long term increase in the positive charge of the oxide layer. This then causes the attraction of electrons inside the silicon towards the positive oxide charge. This results in an electron layer in the silicon detector which changes the detector's characteristics.

Aside from the processes referred to in Section 2.3 ionising radiation can transfer energy directly to the atoms in a crystal lattice [61]. Nuclear collisions and Coulomb effects can transfer sufficient energy to displace lattice atoms [15] to interstitial sites. This loss of energy is called Non-Ionising Energy Loss (NIEL). The displaced lattice atoms will lose their imparted kinetic energy through further collisions with the lattice, potentially creating clus-

ters of defects. The residual thermal energy of the lattice can cause these interstitial atoms to recombine with vacant lattice sites. However, some of the displaced atoms will remain in their interstitial sites having formed stable structures with surrounding atoms [62], forming a Frenkel pair. These are often referred to as traps, due to their ability to retain free electrons or holes.

The number of displaced atoms in the lattice is directly proportional to the NIEL, which in turn is related to the particle type and energy. Charged particles, such as a proton, can interact via Coulomb forces as well as nuclear processes, whereas a non-charged particle, such as a neutron, can only use nuclear processes. Nuclear interactions only become possible above energies of around 1 MeV [15]. Below this value, the NIEL of a proton will be far greater than that of a neutron. The method used to compare irradiations by different types and energies of particles is to say what would be the equivalent damage done by 1 MeV neutrons per cm^2. The notation to denote this will be 1 MeV n_{eq}/cm^2.

The type of particle also affects the eventual distribution of defects. A low mass particle like an electron will generally cause single point defects. These single defects will be unlikely to occur in clusters and are therefore more likely to recombine with the lattice vacancy. A high mass particle like a heavy ion will generally cause substantial damage to the lattice in large clusters. The result of this is, for a given level of NIEL, a heavier particle will do more damage than a lighter one.

The energy required to displace a single atom is $\sim$25 eV [63]. For a neutron to displace a single atom, it would require a kinetic energy of 175 eV. This would increase to 260 keV for an electron. Large clusters of defects generally require greater than 5 keV transferred to them. A neutron's total kinetic energy would have to be 35 keV whereas an electron would need 8 MeV.

In a silicon crystal lattice there exists an energy gap between the valence and conduction bands. Radiation damage to the lattice structure can cause additional energy levels to appear between the two main bands. A defect level that is negatively charged when filled by an electron and neutral otherwise is called an acceptor level. A donor level is one that is neutral

when filled by an electron and positively charged when empty. These can behave much like donor and acceptor dopants. Thermal excitations can generate new holes and electrons using traps. An electron can be excited from the valence band to the trap to create a hole in the valence band. Or an electron in the trap level could be excited to the conduction band. The chance of each of these processes occurring is dependent on the relative energy levels of the trap compared to the valence and conduction bands and also of the temperature of the semiconductor. Alternatively, an electron can fall from the conduction band to the trap or from the trap to the valence band. This will either remove an electron or a hole from the system. The probability of this occurring is proportional to the relative occupation of the levels. The overall effect to a semiconductor device is threefold: to increase the leakage current; to increase the doping concentration and decrease the charge collection efficiency. These will be discussed in turn.

2.3.6.1 Leakage current

Due to random thermal excitations, electron-hole pairs can be created using the trapped level as a stepping-stone between the valence and conduction bands. In situations where there is no electric field present, the electron and hole will typically recombine. However, where an electric field is present the electron and hole will drift to their respective electrodes without recombining. This effect is known as a leakage current. The rate of formation for electron-hole pairs with a trap level is given by,

$$R_{eh} = N_t n_i \frac{v_{th}^e \sigma_e v_{th}^h \sigma_h}{v_{th}^e \sigma_e e^{\left(\frac{E_t}{kT}\right)} + v_{th}^h \sigma_h e^{\left(\frac{-E_t}{kT}\right)}}, \tag{2.16}$$

where N_t is the number of traps; n_i is the intrinsic carrier concentration; v_{th}^e and v_{th}^h are the thermal velocities of electrons and holes respectively; σ_e and σ_h are the electron or hole capture cross sections and E_t is the trap energy level relative to a zero position half way between the valence and conduction bands.

It can be seen from Equation 2.16 that as the trap level gets closer in energy to either the conduction or valence bands, the formation rate will decrease exponentially. Also, the

formation rate will increase as the temperature increases. This leads to the leakage current increasing exponentially. The leakage current of a device will often be quoted at 20 °C with it scaled to other temperatures by,

$$I(T_1) = I(T_2)\left(\frac{T_1}{T_2}\right)^2 \exp\left(-\frac{E_g}{2k}\left[\frac{1}{T_2} - \frac{1}{T_1}\right]\right), \tag{2.17}$$

where T_1 is the quoted temperature and T_2 is the measured temperature.

Whilst most commonly associated with radiation damage, traps will also be present in smaller concentrations in unirradiated devices due to impurities and imperfections in the crystal lattices. The leakage current of an unirradiated device will also be proportionally smaller. Any subsequent damage to an unirradiated device will cause the leakage current to increase proportionally to the fluence of the radiation. Any annealing post-irradiation will reduce the traps available and hence the leakage current. This makes the thermal history of irradiated devices important.

The increase in the leakage current of a device after a period of irradiation can be calculated by,

$$\frac{dI}{dV} = \alpha\Phi, \tag{2.18}$$

where I and V are the leakage current and volume of the device, α is the damage constant and Φ is the irradiation fluence. The damage constant varies between different materials and temperatures. For silicon at 20 °C, the value given for α is 7.77 x 10^{-18} A/cm [64].

Another effect of leakage current is that it will increase the temperature of the device. If this heat cannot be dissipated, then a thermal runaway effect may occur with the increase in temperature leading to further increases in leakage current. This means that irradiated devices in particular need to have adequate cooling sources factored into their design specifications.

2.3.6.2 Doping Concentration

The depletion voltage of a device is the voltage required to fully extend the electric field throughout the device [63]. It is related to the effective doping concentration by,

$$V_{dep} = \frac{q_0}{2\epsilon\epsilon_0} |N_{eff}| \, d^2, \tag{2.19}$$

where V_{dep} is the depletion voltage; N_{eff} is the effective doping concentration and d is the depth of the detector.

This holds true both for doping concentrations caused by adding donor and acceptor atoms and radiation damage. For an initially n-type material, a low irradiation fluence causes the effective doping concentration to decrease exponentially. This is due to an apparent removal of donor atoms. Further irradiation will cause a type inversion to a p-type material with an exponential increase in the doping concentration as the irradiation continues. An n-type material after type inversion will display the same behavior as a p-type material. An increase to the effective doping concentration will increase the depletion voltage required to fully deplete the device. This will have a knock-on effect to the heat generated by the device and is called thermal runaway.

2.3.6.3 Charge Collection Efficiency

Defects to the crystal lattice can act as traps to any charge generated by ionising radiation. Electrons can drop from the conduction band to the trap levels for long enough to prevent their collection within the integration time of the amplifier. This will mean that the total signal generated by ionising radiation is reduced by radiation damage. This can be compensated for in standard silicon devices by maintaining a sufficiently high electric field throughout the silicon. Operating a device at the depletion voltage will lead to the peripheries having very low fields. A higher operating voltage will give greater fields throughout a device and hence reduced trapping.

Any charge that is trapped for longer than the integration time of the device will not be collected. This is referred to as ballistic deficit. Again, this can be reduced by increasing the

integration time.

2.3.6.4 Annealing Processes

Defects caused by ionising radiation can be altered through a process called annealing [65]. Heating a silicon substrate can provide defects with the thermal energy required to return to their lattice positions. There are multiple mechanisms through which this can occur.

The migration of defects can occur once defects gain enough energy to become mobile. The defects will continue to roam throughout the lattice until they can locate a stable position. This can be either through recombining with a counterpart, being held at a surface or dislocation in the silicon, or by associating with other defects to form stable complexes. A stable complex can be formed by defects of the same type, of different types or by associating with impurities in the silicon.

Another mechanism whereby annealing can affect the structure of defects is through a process known as dissociation. This will occur when a stable complex of defects is provided with enough energy to break into smaller complexes or individual defects. These smaller structures can then migrate through the the lattice as previously discussed.

Overall, it is difficult to tell exactly which mechanism is responsible for any specific portion of annealing. When a sample undergoes annealing, a combination of the mechanisms will happen simultaneously.

Annealing can be performed at any temperature. Any annealing process has an activation energy associated with it. The rate of annealing will then be proportional to $e^{\left(\frac{-E_a}{kT}\right)}$ where E_a is the activation energy of the annealing process. This will then increase as the temperature increases. Generally, when quoting the length of an annealing period, this will be shown as the number of minutes at 60 °C that would be required to get an equivalent result.

Figure 2.15 shows the effect annealing has on the effective doping concentration. The change in the effecting doping concentration, ΔN_{eff}, can be divided into three contributing components. N_A is the component that dominates in the initial stages of the annealing of the acceptors. N_C is a constant factor and independent of the annealing time. It represents

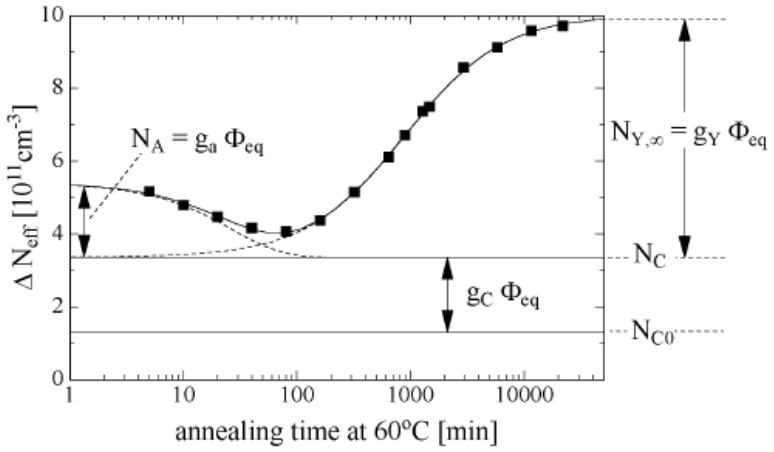

Figure 2.15: The annealing behavior of the effective doping concentration ΔN_{eff} at 60 °C after radiation damage [65]. Sample was irradiated with a fluence of 1.4 x 10^{13} cm^{-2}.

the stable damage to the lattice. Finally, N_Y is the long-term reverse annealing component. The effect of annealing a device will only end when this component saturates at long time scales. Annealing for up to 80 minutes at 60 °C causes a decrease in the effective charge concentration [65]. For a non-type inverted device the depletion voltage simply increases. For a type inverted device this leads to a decrease in the depletion voltage and is considered beneficial. Annealing beyond this, however, leads to a longer term period of reverse annealing regardless of whether type inversion has occurred.

Chapter 3

Characterisation of a 3D detector

In this chapter, the response of a 3D double-sided pixel sensor [36] to high energy pions is explored [22][66]. The device was bump-bonded to a Timepix pixel readout ASIC. Similar measurements have been made on a full-column 3D sensor elsewhere [67]. Here a high resolution study over a unit pixel cell in a double-sided 3D detector is presented. The detection response across a unit pixel cell to high energy pions is mapped and the effects due to the columnar electrodes on the detection efficiency and charge sharing is investigated. The spectral response of the regions between the electrode columns, the inter-column region, and in the regions above and below the columns are shown. This is studied through variations in the applied bias voltage and effective charge threshold used in the offline analysis. Furthermore, the detection efficiency as a function of the angle of incidence of the pion beam to the surface of the sensor is measured.

3.1 An Introduction to 3D Detectors

Future High Energy Physics (HEP) and synchrotron X-ray experiments will require a new generation of detectors capable of high-speed readout, operation under extreme radiation fluences and covering large areas with minimal dead space. The 3D sensor design, discussed in Section 2.2.3, offers several advantages over the planar silicon sensor design and is a strong contender for such future detection systems. The 3D sensor architecture [8] differs

from a standard planar sensor design by having columnar electrode structures created in the sensor substrate rather than on the device's surfaces. The distance between the electrodes in a planar device is defined by the sensor's thickness. This is no longer the case in the 3D design where the electrodes can be brought closer together significantly reducing the charge collection time of the device and also reducing the required bias voltage. A greater electric field reduces the trapping effect of radiation induced defects and therefore increases the detectors charge collection performance after heavy irradiations [68] making the detector design attractive for applications in future high energy particle tracking experiments.

3.1.1 3D Device Under Test

The double-sided 3D sensor [37] is a modification of the original design as first proposed in 1997 [8]. This sensor configuration differs from that of single-sided 3D sensors in that the holes for the columns are etched from opposite sides of the wafer. This simplifies the fabrication process and increases the production yield. The difficulty of doping two different kinds of holes on the same side of the wafer is also avoided. It is only necessary to create patterned electrode contacts on a single side of the wafer, the electrodes on the bottom side being shorted together. A further advantage of the double-sided 3D sensor is that all regions of the device have active silicon. This is because charge is still collected in the region above or below the columnar electrodes.

The device investigated in this chapter was designed by the University of Glasgow and IMB-CNM[1] and fabricated by IMB-CNM. In this design, inductively coupled plasma (ICP) was used to etch holes with a diameter of 10 μm to a depth of 250 μm in a 285 μm thick substrate sensor material. The high aspect ratio was made possible by an alternating sequence of etch and passivation cycles. This is known as the Bosch process [69]. The p^+ and n^+ electrodes were produced by partially filling the holes with polysilicon and doping with boron and phosphorous. The junction was created at about 3 μm into the silicon substrate as measured in a scanning electron microscope [37]. These measurements also show the

[1]Barcelona Microelectronics Institute, National Microelectronics Center, Barcelona, Spain.

polysilicon layer thickness is 3 μm at each edge of the hole. This was passivated with an additional 1 μm of silicon dioxide. The sensor surface was passivated and the polysilicon at the electrodes was exposed and coated with aluminium to create the contacts for bump-bonding to the readout chip. The basic cross-section of a 3D device is shown in Figure 2.8.

Devices were fabricated with both n and p-type bulks. The induced signal is generated by the movement of both electrons and holes. The device used here was a hole collecting double-sided 3D detector with n-type substrate and p-doped columns connected to the electronic readout. The columns had a pitch of 55 μm. The device was solder bump-bonded by VTT[2] to a Timepix readout chip. A low grade readout chip was used for this R&D project. Hence, there were some inactive pixel columns. The device used here was fabricated from a wafer with a resistivity of 13 kΩcm and had a leakage current of 3.8 μA at 20 V at room temperature. The double-sided 3D sensors depletion behaviour is more complex than that of the single-sided 3D or planar designs.

To test the depletion characteristics, additional double-sided 3D pad sensors were fabricated to match the pixel size of Medipix2. These consisted of 92 x 92 arrays of p-type readout columns with 55 μm spacing. The 90 x 90 columns in the centre were connected by a metal layer to form a pad, and the surrounding ring of readout columns were connected together to form a grounded guard ring. During each test, the pad was held at ground, the back contact was biased, and a 10 kHz AC signal was applied between the two. The result of one such test is shown in Figure 3.1. The capacitance decreases as the device depletes. A sharp drop in capacitance up to the line at 2.4 V occurs as the region between the columns depletes. A device with columns spaced 55 μm apart will fully deplete below 3 V with the precise value determined by the geometry. The line at 9 V denotes where the device should be fully depleted underneath the columns. The device was operated at 20 V during the experiments as this ensured it was over-depleted with a non-zero electrical field throughout.

[2]VTT Technical Research Centre, Finland.

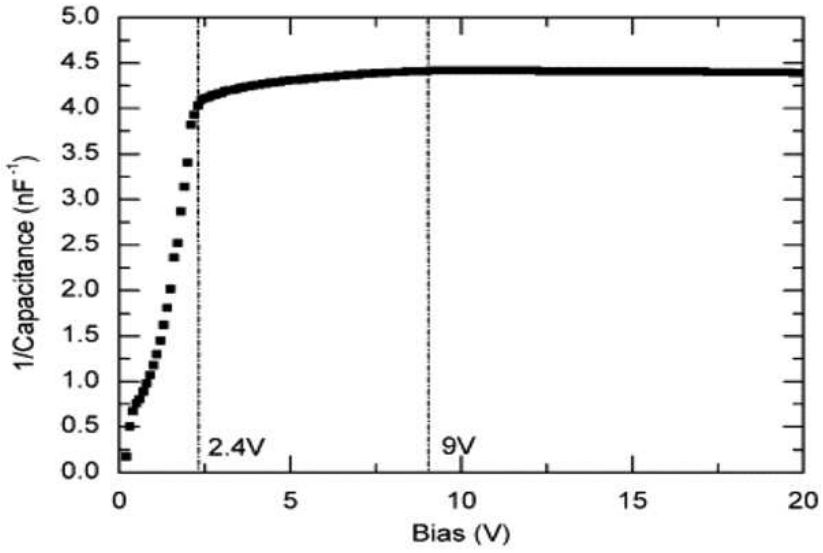

Figure 3.1: Inverse capacitance characteristics of a double-sided 3D pad detector with 90 x 90 columns and 55 μm pitch [36].

3.1.2 Timepix ASIC

Timepix [70] chips are readout ASICs produced by the Medipix2 collaboration for hybrid pixel detectors. The Timepix chips each had 256 x 256 square pixels with 55 μm pitch. Each pixel is independently coupled to the corresponding pixels of the sensor with an array of solder bump-bonds. Together the sensor pixel and readout chip pixel form an independent readout channel. Each readout chip pixel contains amplification and digitisation circuitry. The Timepix chip is a development of the Medipix2 chips that adds the possibility to propagate a clock signal to each pixel in order to provide additional timing functionality.

Medipix2 is a photon counting chip. Each pixel channel contains an amplifier and a discriminator followed by mode control logic and a 13 bit pseudo-random counter with an additional stop bit. This additional bit extends the number of counts available to 11 810 and this is iterated each time a signal from the sensor causes the amplifier signal to pass the discriminators threshold.

The three possible modes of operation are counting, time of arrival (ToA) and time over threshold (ToT). In counting mode the Timepix pixels behave in a similar manner to the original Medipix2 pixels, incrementing the counter each time the output of the amplifier passes the threshold. In ToA mode the pixel records the time between the moment when the

amplifier first passes the threshold and the closing of the shutter, up to a maximum of 11 810 counts within the pulse length of 230 μm. In ToT mode the discriminator output is used to gate the clock to the counter, recording the time the amplifier signal is above threshold and thus providing an indication of the total energy deposited. The ToT mode was used in this study because the triangular nature of the amplifier pulse means that the time recorded is proportional to the amount of charge deposited in the pixel [70]. The energy resolution is then due to the ToT mode's time resolution. Using the serial readout at 200 MHz, the time to read the entire matrix is around 5 ms. However, faster speeds are possible using a 32-bit parallel bus.

To ensure that each pixel on the chip uses a similar threshold, Timepix pixels contain four bits of trimming information that can be individually programmed. The process of setting these values to provide a uniform global threshold is referred to as equalisation.

Threshold equalisation is used to compensate the pixel to pixel threshold variations due to local transistor threshold voltages and current mismatches or more global effects like on-chip power drops. This compensation is done by means of a 4-bit current DAC placed in the discriminator chain of each pixel. The current range of this DAC is controlled by the Ths global DAC with a LSB range of 040 nA. The measured INL of this 4-bit DAC in the full pixel matrix is less than 0.8 LSB. To calculate the equalisation mask the threshold distribution for each of the 16 threshold adjustment codes is found. Then the adjustment code is selected for each pixel to make its threshold as near as possible to the average of the threshold distribution mean values. Figure 3.2 shows an example of a threshold equalisation of a Timepix chip in both collection modes. The threshold variation before equalisation is 240 e^-rms and after equalisation the achieved noise free threshold variation is 35 e^-rms for both polarities. The minimum detectable charge is defined as the smallest input charge which all pixels are able to resolve when the global threshold is set just over the noise.

The shaper and amplifier in the pixels are able to operate in both positive and negative polarities allowing the system to collect either electrons or holes from n-type or p-type bulk sensors. Here only hole collecting sensors were investigated. The readout of Timepix is

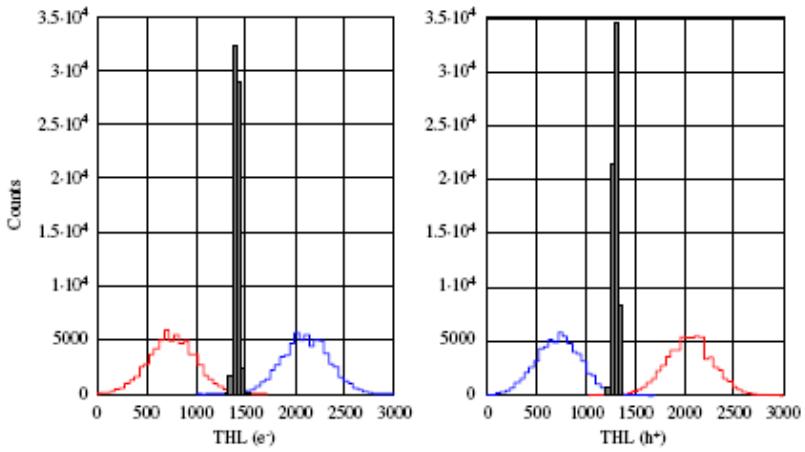

Figure 3.2: Example of the threshold equalisation result for both polarities. On the left is the electron collection and on the right is the hole collection.

performed by a shutter signal. When the shutter is open the chip is sensitive and the counters are active, counting either the number of hits seen or the number of clock ticks where appropriate. When the shutter is closed the counters are reconfigured into 256 pixel long column shift registers and the data is read off as a matrix of values which are decoded by the readout system.

The absolute DAC value of the applied threshold corresponds to the pedestal of the pixel variation between individual chips due to slight fabrication differences. The DAC controlling the global threshold, THL, is set with respect to the mean of the distribution of equalised noise edges. The absolute values were set to give a threshold corresponding to a deposited charge of approximately 1600 electrons in the assemblies that made up the telescope and in the DUTs.

3.2 Experimental Setup

The double-sided 3D n-type sensor, bump-bonded to a Timepix readout chip, was tested in a high energy pion beam provided by the Super Proton Synchrotron (SPS) at CERN. The telescope that was used is shown in Figure 3.3. The telescope allowed for the easy integration of the device under test (DUT), provided complete compatibility between the readout systems and enabled a frame rate of about 1.25 Hz.

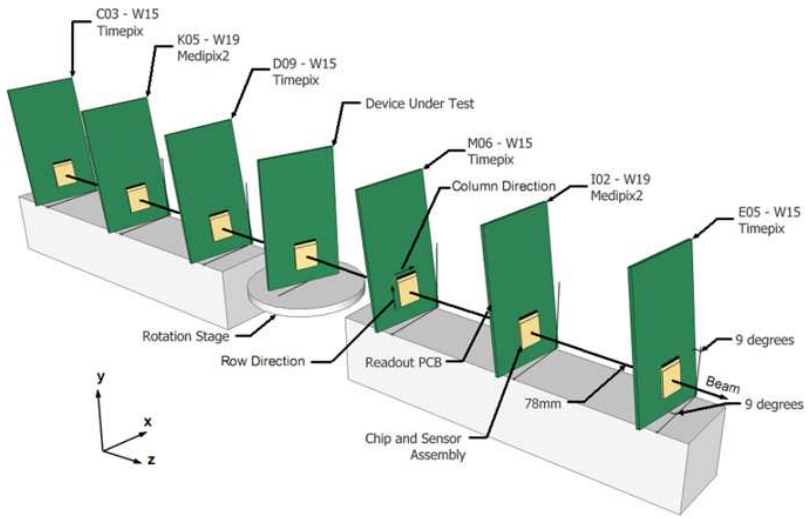

Figure 3.3: A diagram of the pixel detector assemblies within the telescope, showing the angled four Timepix and two Medipix2 detectors and the Timepix DUT with its axis of rotation.

The telescope consisted of six pixel planes, four Timepix and two Medipix2 separated from each other and the DUT by 78 mm. Each was bonded to a standard 300 μm p^+-on-n planar pixel device. As the Medipix2 planes only provide binary information, and so produce a lower spatial resolution, they were sandwiched between the Timepix sensors. The Timepix sensors formed the innermost and outermost stations of the telescope arms. The Timepix chips were used in ToT mode in order to benefit from a charge measurement in each pixel, and to be able to optimise the resolution by finding the cluster centres using charge weighting. In addition, the planes were oriented at an angle in the horizontal and vertical directions in order to guarantee charge sharing and further optimise the resolution. An estimate of the optimum angle is provided by the expression $\tan^{-1}\frac{\text{Pitch}}{\text{Thickness}}$ which gives the angle where tracks always traverse more than one pixel, due to geometric factors. In practice the angle providing the best resolution is affected by factors such as charge spreading, pixel calibrations, and non-linear charge sharing corrections, as well as the choice of the angle for the orthogonal direction. In this prototype telescope the angles of the telescope sensors were fixed to 9° in both the horizontal and vertical axes perpendicular to the beamline, which gave results which were close to the minimum achievable. The minimum given by the pitch and the thickness would have been at 10.9° but this angle can be lessened because it does

take into account the diffusion of the charge in the detectors. The DUT was mounted at the centre of a symmetric arrangement of chips to further improve the resolution that could be achieved.

To allow a resolution measurement to be taken with the DUT at as many angles as possible, and to increase precision, the DUT was mounted on high precision rotation and translation stages driven by step per motors that allowed it to be turned and aligned remotely. The stages used allowed movements with an accuracy of 2 μm and 50 μrad for the translation and rotation states respectively.

The Medipix2 and Timepix assemblies, including the DUT, were read out using USB driven systems provided by CTU Prague [71] and the Pixelman data acquisition (DAQ) and control software [72]. An example of the Pixelman DAQ is shown in Figure 3.4.

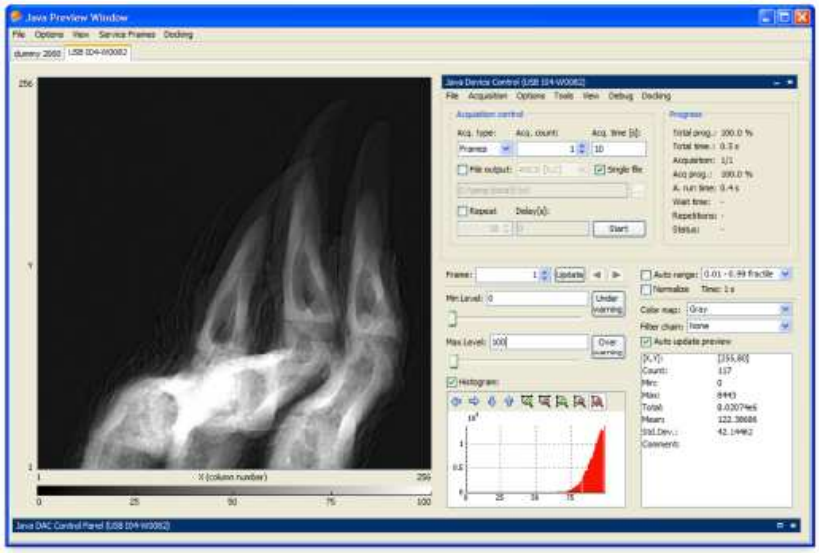

Figure 3.4: An example of the Pixelman DAQ [73].

These are the standard, portable, low-bandwidth readout systems used in most Medipix applications to date. Each USB unit is attached to one chip. A signal is applied simultaneously to all the USB readout units and its rising edge triggers local shutters to individual chips. The length of the shutter is programmable in each USB unit and it was set to be the same for each assembly. It was optimised on a run by run basis to capture between 100 and 500 tracks per frame depending on beam conditions and the required analysis. The microcontroller in the USB unit introduces a delay between the trigger being received and the

shutter being sent of 4.0±0.5 μs. Since the shutter periods were always greater than 10 ms, the error on the efficiency measurement introduced by this jitter should be small. In situations where a shorter shutter is required, such as high particle flux environments, this will become a constraint on the use of the existing USB systems.

3.3 Results

3.3.1 Analysis and Track Reconstruction

The first step of the reconstruction process is to form clusters from neighbouring pixels that registered hits. A cluster is obtained from joining all adjacent hit pixels in a given assembly. The position of the cluster is determined from a charge weighted average of the contributing pixel positions in the row and column directions, using the ToT values from the individual pixels as a weighting factor. A maximum cluster charge cut is applied for the clusters in the tracking in order to suppress high energy deposits and noisy pixels.

A linear fit is made to combine the clusters on the different assemblies into tracks. The algorithm obeyed the following process. Firstly, any frames with 5000 or more clusters were ignored to remove a small number of saturated frames. Next, the central detector was taken as the primary reference plane and each plane within the telescope was examined in turn. Starting with the first plane, each cluster is compared to all of the clusters on the remaining detectors in the telescope. If there are a set of clusters, one on each telescope plane that are within 100 μm of each other, these will form a track. A cluster is required on each plane of the telescope. A straight line track fit is then applied using the full alignment information. Once a cluster has been associated with a track, it can not be associated with any others.

Initially, the alignments of the telescope planes were set by measuring the angles and distances between the planes by hand. Using this as a starting point, an improvement was made by using a software alignment that performed an iterative procedure by minimising the residual between the track intercept position and the reconstructed cluster position. All degrees of freedom were aligned which included the displacement of each plane in the row

and column directions and along the beam, and the rotation of the planes around all three axes. The same procedure was applied to the DUT. After alignment the residual means were centred on zero, and the variation of the mean of the residual across the width of the detector was below ± 1 μm. This is shown in Figure 3.5. Were the residuals either not centred on 0 mm this would imply that the detector was misplaced laterally. If the mean of the residuals varied with the global position so that the dark band in Figure 3.5 was diagonal then this would imply that the misalignment of the detector was with the angle of rotation.

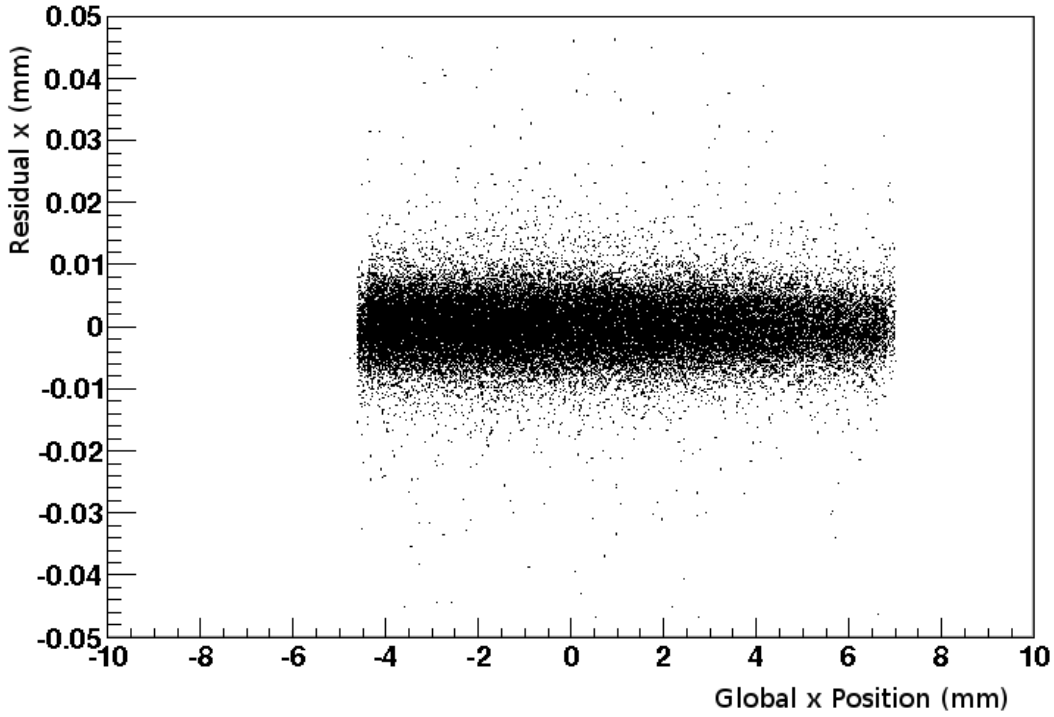

Figure 3.5: The residual in the x direction against the global x position.

The distribution of the residuals has been studied to extract the resolution of the individual telescope planes and the precision of the track intercept point at the DUT. The resolution at the DUT in both the column and row directions was found to be 2.3 ± 0.1 μm. The spatial resolution was defined as the track pointing error at the position of the DUT, with the measured biased residuals in the telescope planes being compared to the results of a Monte Carlo simulation.

Extracting the resolution of the DUT itself required a slightly different procedure. First,

the tracks were extrapolated to the plane of the DUT and a global residual formed between the tracks and all clusters in the DUT. In order to investigate the resolution in x, clusters with a residual of less than 100 μm in y were selected, and vice versa. The resulting histograms were then fitted with single Gaussians. The error on the precision was estimated by dividing the datasets into two and comparing the resolution, by varying the binning of the histograms, and by varying the cut on the y of the cluster. In addition there is slightly larger error for the perpendicular fits, where the histograms become less Gaussian due to the more binary nature of the resolution

A number of additional cuts were applied to select a clean data sample. First, the centre of clusters considered in the analysis of the DUT were required to be within 200 μm of the track intercept point. In addition, all tracks considered in the analysis were required to be separated by more than 600 μm at the DUT. If there were multiple tracks separated by less than 600 μm at the DUT then all of the tracks were discarded. This reduced the potential for incorrectly associating clusters on the DUT to the wrong tracks.

The Timepix chip used for this R&D project with the 3D sensor was of a lower grade and had two non-responding columns (512 pixels). Furthermore, the bump-bonding of the sensor was not perfect and introduced some additional dead or noisy pixels. A map of dead and noisy pixels was produced by exposing the sensor for 20 minutes to an X-ray source. An average of 1000 counts was obtained per pixel, and those pixels more than four standard deviations from the mean were flagged as dead or noisy. This identified an additional 128 pixels, which were excluded from the analysis. This map is shown in Figure 3.6.

This map was used in the analysis and all extrapolated tracks within 3 pixels of a dead or noisy pixel on the 3D sensor were excluded from the analysis. Furthermore, all extrapolated tracks were required to be more than 7 pixels from the edge of the 3D sensor.

The ToT counts in the Timepix are not linearly related to the charge deposited for low values of charge [74]. This is shown in Figure 3.7. At higher levels of deposited charge the relation is linear but with an offset in each pixel. Hence the effect of a ToT cut on one pixel and multiple pixel clusters differs, with larger clusters displaying a greater measured charge

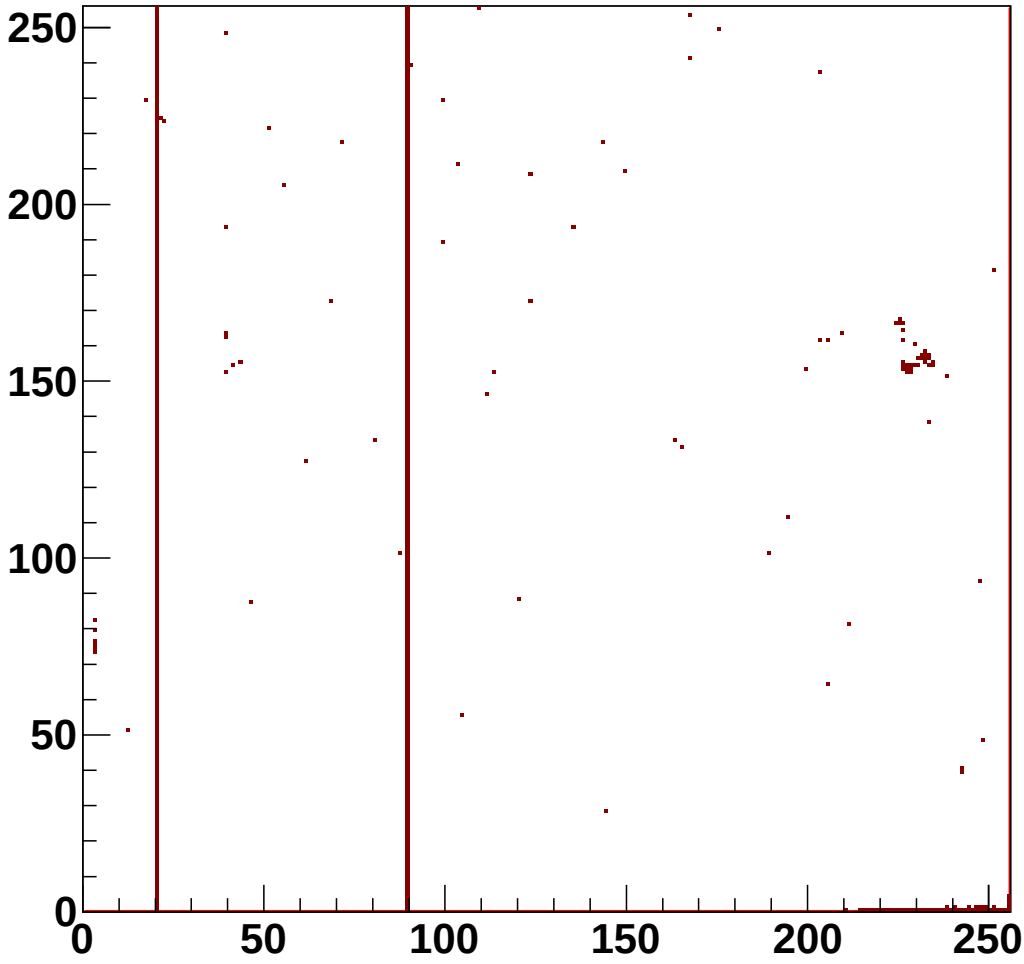

Figure 3.6: A map showing the location of dead and noisy pixels. This included two full columns. The x and y axes show the pixel number.

for a particle than if the same particle deposited its energy in a single pixel.. This is described in detail elsewhere [22] along with the calibration procedure. As a result it will be specified in each case whether the ToT cuts are applied to the cluster as a whole or a single pixel.

The detector was positioned approximately perpendicular to the beam and the alignment was determined by minimising the ratio of the average number of pixels in the column's direction of the sensor contributing to a cluster to the same quantity in the row's direction, and by maximising the fraction of single pixel clusters [22]. This was achieved by moving the detector manually using the stages and was performed in real time. The detector was

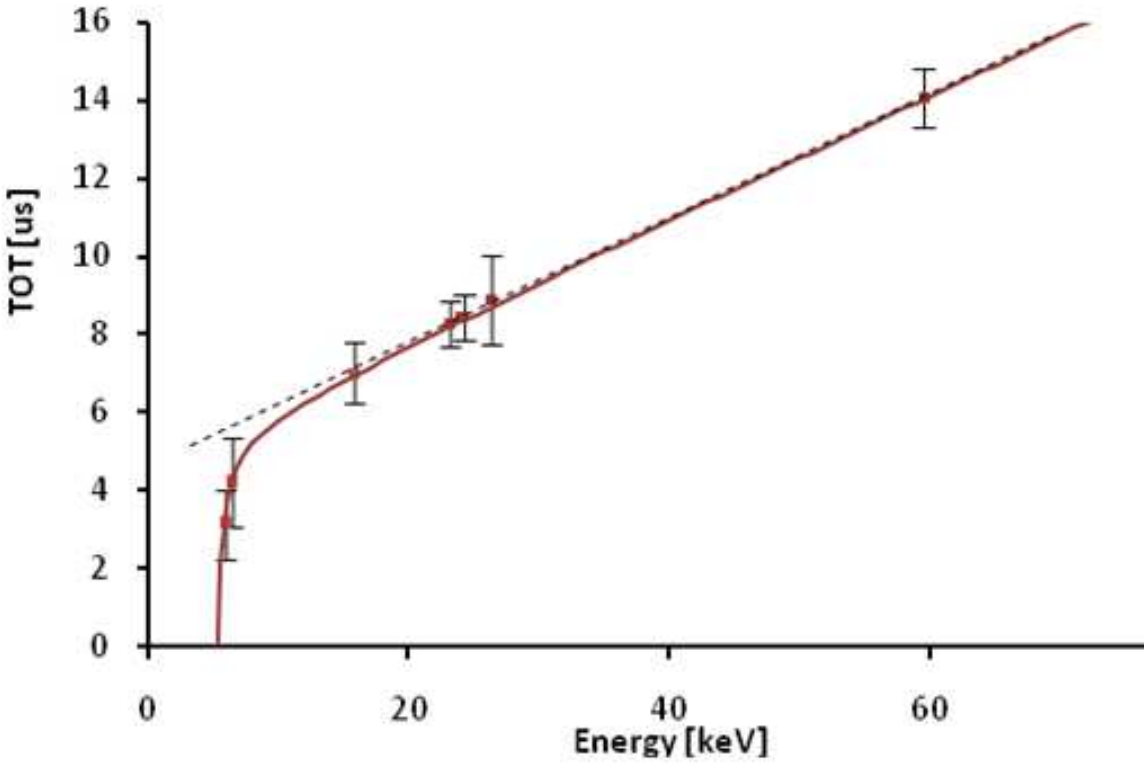

Figure 3.7: Time over threshold dependence on particle energy. The global threshold is set at the x-intercept of the red line.

rotated around the vertical axis during the studies reported here. The sensor was estimated to be offset from the set angle of rotation by -0.29°. The following plots are labeled with the stage rotation angle, rather than the true angle. This alignment accuracy corresponds to a lateral deviation of the beam by 1.6 μm as a track travels through the full thickness of the sensor substrate. This is less then the nominal diameter of the columnar electrode of 10 μm, but adds an additional smearing that reduces the resolution to the results.

3.3.2 Landau Distributions

Particle tracks reconstructed by the telescope are used to find the track intercept positions on the DUT. The energy deposited in the pixel on the DUT where the track intercepts is obtained by operating the Timepix in ToT mode. Figure 3.8 shows the mean energy measured as a function of the track intercept position inside a pixel cell. The results from the full sensor have been mapped onto a single pixel. Figure 3.8(a) shows the mean energy deposited in

the hit pixel while Figure 3.8(b) shows the mean energy of the cluster, combining the charge deposited in the hit pixel with that of its neighbours. The frequency of the collected number of ToT counts for areas of interest are shown in Figure 3.8(c).

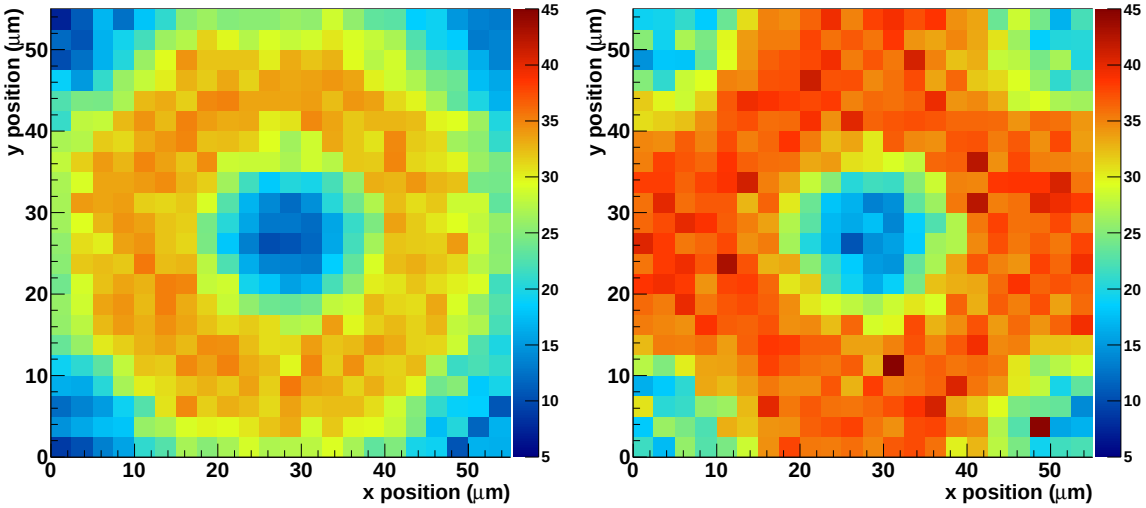

(a) (b)

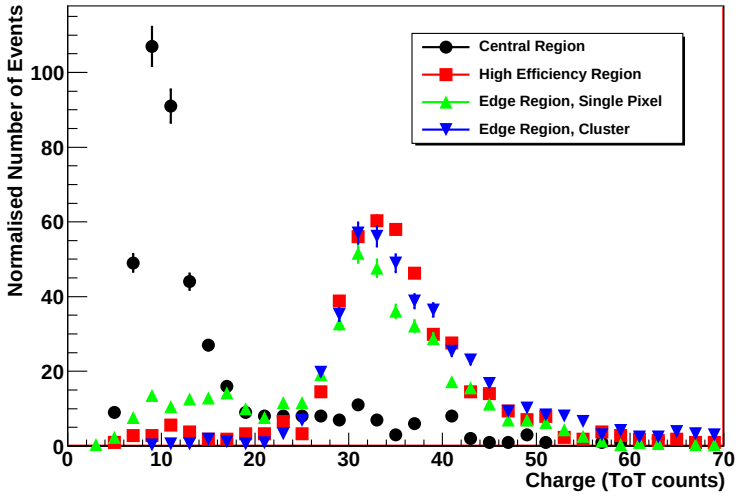

(c)

Figure 3.8: Pixel maps showing the mean energy deposition across the pixel matrix, for a single pixel (a) and the energy in clusters (b). (a) also shows the histograms of the energy deposited at the pixel edges for the single pixel and the clusters. Histograms of the ToT counts (c) in the central electrode region, away from the central electrode and pixel edges. Each region is normalised so it has the same integral.

To assist the analysis of the different pixel areas four regions were defined. The central electrode region is defined as a 5 μm radius circular region centered on the central electrode.

The corner electrodes' region consists of quarter circle areas of the same radius in the pixel corners. A 5 μm radius has been chosen here as this corresponds to the size of the etched electrode. The third region was defined as the area of high counts, away from the electrode regions. This was the area outside a 15 μm radius region from the corner and centre electrodes. A 15 μm radius was chosen as this excludes all potential for reduced counts due to the electrode column size, 5 μm radius, the diffusion of the dopant into the substrate of 3 μm around the polysilicon layer [37], the smearing of the low count region by the resolution of the telescope, 2.3 μm [22], and the sensor being not quite perpendicular to the beam. The final region was the edge region. This was defined as a rectangle on each side on the pixels, extending 5 μm into the pixel and starting 15 μm away from the corner of the pixel.

In the area away from the collecting electrodes and the pixel boundary, denoted as the high efficiency region, the energy response exhibits the standard Landau shape expected from MIP detection. In the area of the central electrode the average recorded energy reduces. A similar distribution was also seen for the corner electrodes with further losses due to the charge sharing as well. This is interpreted as no charge being collected in the electrode column but charge being collected in the 35 μm silicon above the central electrode. The ToT value is not linearly related to the charge deposited but can be corrected for with a calibration curve. After applying the appropriate calibration curve values [22], a ratio of the most probable value of the Landau distribution in the region above the electrode and the region away from the electrodes of $11 \pm 3\%$ is obtained. This is in agreement with the expected ratio of 12% from the height of the region above the central electrode (35 μm) to the full device thickness (285 μm).

The ToT value measured at track intercept positions along the boundaries of the pixel, but away from the corners, is also shown in Figure 3.8(a). A number of counts at lower energy deposition than in the main peak is observed, which is expected due to charge sharing with the neighbouring pixel. If the charge deposited in the neighbouring pixels is combined into the cluster charge then the full energy Landau shape is resolved at the pixel edges. The charge sharing is discussed in further detail in Section 3.3.6.

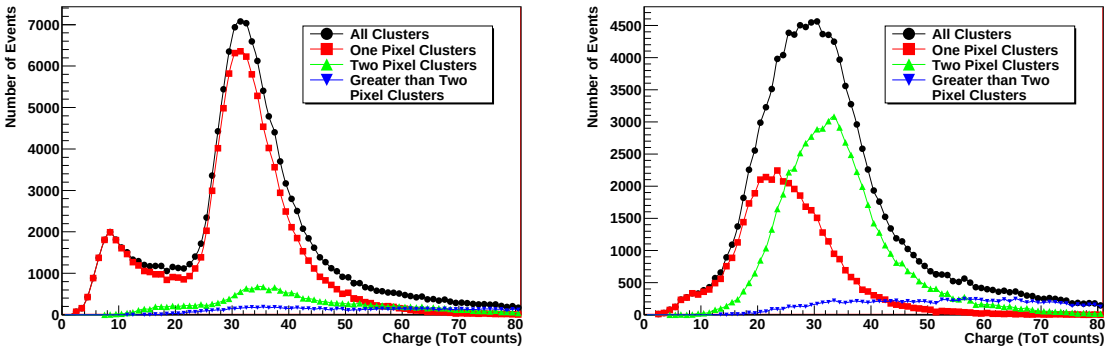

Figure 3.9: Raw ToT distributions in the 3D double-sided sensor for perpendicular tracks (a) and tracks with 10° incident angle (b). The higher energy peak in the clusters of greater than two pixels is a result of the non-linearity in the Timepix device.

Figure 3.9 shows the cluster ToT distributions for tracks with perpendicular incidence and with 10° incident angle. At 10°, almost all of the tracks will pass through two pixels. The signals for perpendicular tracks are dominated by the single pixel clusters. This is because the 3D detector showed only a small charge sharing effect at the edges and corners. The one pixel cluster ToT distribution shows the same double landau distribution as in Figure 3.8(c). The peak at 30 ToT counts is from tracks that do not pass through the detector's columns, the peak at 8 ToT counts is caused by tracks passing through the full depth of a column. The clusters with more than one pixel in them have only a single peak, with a ToT count of 30, matching the full signal of a pion track. The clusters that have two or more pixels within them typically occur when a track is incident at the edge of a pixel.

When the tracks are incident at a larger angle, the ToT distributions are modified. Now, a slight majority of the clusters are two pixel clusters rather than one pixel clusters. Also, the ToT distributions only have a single peak in them. No track is now contained within a single column as the normally incident tracks could have been. The one pixel clusters are lower in energy, as a result of charge loss to adjacent pixels that is under the set threshold.

3.3.3 Efficiency Distributions at Normal Incidence

If a reconstructed cluster position is within 200 μm of a track intercept position, then a hit is considered efficient. The efficiency maps are projected onto a unit pixel cell with entries placed at the track intercept point. Samples of approximately 30 000 tracks recorded in the telescope were used. Bias voltages of 2 V and 20 V were studied. A bias voltage of 2 V will partially deplete the region between the columns, whereas a bias voltage of 20 V will over-deplete the sensor. Errors for all efficiency measurements were calculated from the probability of mistakingly associating a noise hit to the track position where there is no actual hit and was found to be ±0.5%.

Figure 3.10 shows the efficiency measured across the pixel for 2 V and 20 V bias. These efficiencies are then summarised in Table 3.1.

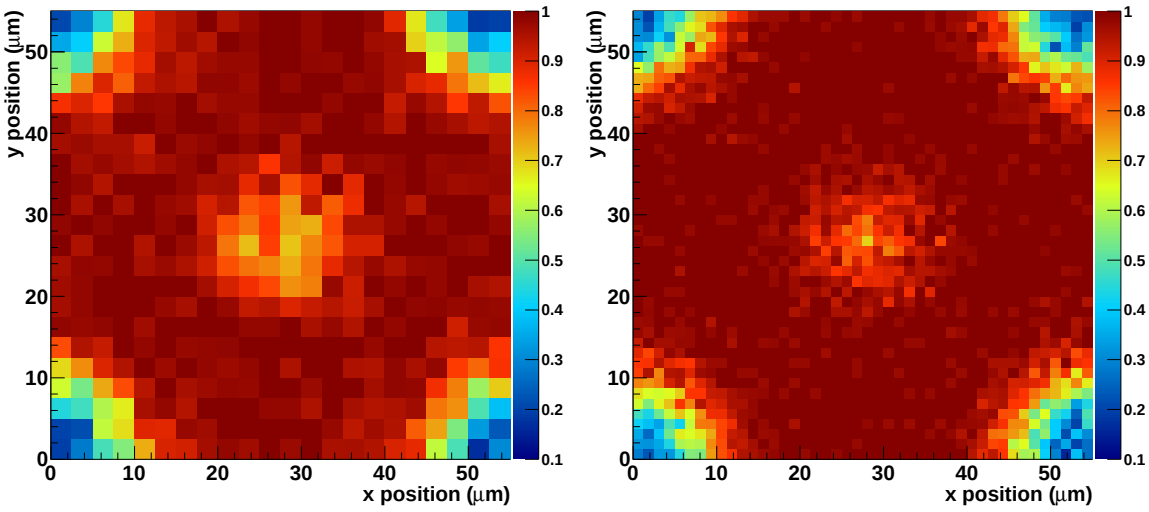

(a) (b)

Figure 3.10: Pixel efficiency maps at normal incidence to the pion beam with the sensor biased at 2 V (a) and 20 V (b).

For normal incidence tracks with a 20 V bias voltage applied the overall efficiency of the pixel is 93%, with a clear drop in efficiency evident at the positions of the electrodes. In the region away from the electrodes an efficiency greater than 99% is already measured at only 2 V. At 20 V bias an efficiency of 86.7% is found in the 5 μm radius region around the central electrode. Particles incident on this region deposit charge in the 35 μm of the depleted

	Efficiencies (%)			
Voltage	Corner	Centre	Area of High Counts	Pixel
2 V	35.6±0.5	79.1±0.5	99.1±0.5	91.2±0.5
20 V	39.1±0.5	86.7±0.5	99.7±0.5	93.0±0.5
20 V 20 ToT cut	18.8±0.5	14.2±0.5	98.1±0.5	78.9±0.5

Table 3.1: Efficiencies of different regions of the pixel measured in the Pion beam. 2 V and 20 V biases were applied, and an additional measurement with a 20 ToT cut applied to the 20 V measurements.

substrate above the columnar electrodes. The efficiency in this region is still reasonably high in this double-sided 3D sensor, in contrast to the drop to 60% that is seen in a single-sided 3D sensors [67], as the 2800 electron-hole pairs typically deposited in 35 μm is greater than the detector threshold of approximately 1600 electrons. A larger drop in efficiency is observed around the corner electrodes where an efficiency of 35.6% is measured at 20 V bias. Particles incident on the corner electrodes will also travel through 35 μm of depleted silicon at the columns. However charge deposited at the corners will be shared by up to four pixels, and each portion of the charge collected by an individual pixel may fall below threshold. At 2 V the corner and centre efficiencies both drop compared with 20 V. This is to be expected as the electric field above or below the electrodes is virtually zero at 2 V combined with there only being 35 μm of active silicon. In the 20 V biased data, applying a cut on the total charge of the pixel cluster of 20 ToT counts (around 13k electrons) requires that particles have deposited charge in the full 3D region, not just the region above or below the electrodes. As expected this causes the efficiency values at the centre and corner of the pixel to reduce significantly, with only a small drop in the area of high counts.

The efficiencies measured around the centre and corners can be interpreted as effective insensitive column sizes. The efficiency is calculated in a 15 μm radius region around the electrode columns, an area containing the full region with reduced efficiency due to the electrodes. This region is then modeled as an inefficient column surrounded by a fully efficient area. The radius of the column required to obtain the measured efficiency in this region is calculated. At 20 V bias, applying this calculation to the central electrode results in an insensitive column radius of only 2.7 μm. This result is smaller than the true electrode col-

umn size since charge is collected in the region above the central electrode. Applying a ToT cut of 20 counts on the charge of the pixel cluster removes the charge collected above the central electrode, and gives an effective radius corresponding to the column in the full 3D region of the device of 7.5±0.8 μm. This is compatible with the known column dimensions and dopant diffusion. The corner regions, which may tend to overestimate the size due to additional charge sharing effects, give an effective radius of 8.7±1.3 μm.

An alternative measurement of the size of the inefficient region around the central electrode is obtained from plotting the efficiencies as a function of their distance to the pixel centre, as shown in Figure 3.11. A threshold cut is applied to the total pixel cluster charge between 10 and 20 ToT, to remove the charge collected only in the silicon volume above the column. The line connects the average efficiencies at each position and the error is given by the standard deviation between values obtained for regions at this distance. The FWHM gives a value of 7.6±0.6 μm, where the error is assigned from varying the ToT cut. This is in line with the expected etched column size and dopant diffusion and with the value (7.5±0.8 μm) obtained from the first method above.

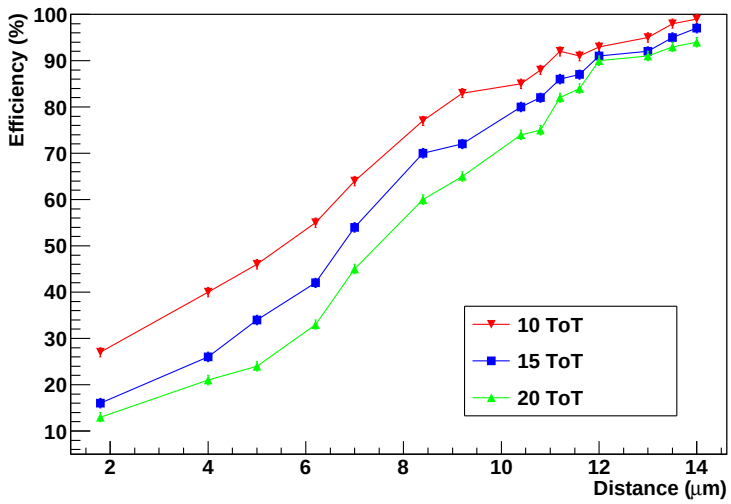

Figure 3.11: Average efficiencies of the 20 V pixel map at different threshold cuts plotted against the distance from the centre of the pixel.

3.3.4 Efficiency Distributions at Angles

The efficiency map study was repeated with the DUT rotated by up to 18° around the vertical axis. In Figure 3.12 the efficiencies of selected regions of the detector are shown. As the angle is increased a track traverses less of the electrode column and a greater section of the depleted silicon. At 10° and higher the electrodes have no effect on the efficiency measurements and an efficiency of 99.8±0.5% is reached across the pixel matrix. At an angle of 10° the track traverses a full pixel within the thickness of the sensors, and this is the angle of best resolution.

3.3.5 Single Pixel Efficiency versus Threshold

Applying energy threshold cuts on the 3D device further illustrates its spectral response. The track is intercepted with the DUT and the single pixel efficiency of finding a hit in the intercepted pixel is obtained. Here the efficiencies measured are lower than those reported previously when clusters (multiple pixel efficiencies) were recorded. Figure 3.13 shows the effect of modifying the ToT threshold value cut on the single pixel efficiency. This was done offline to the collected data, so does not include the ToT cut that is performed on the chip itself. Increasing the offline energy threshold set across the 3D device to 20 ToT counts removes the low energy counts that are deposited in the silicon above the central column and at the boundaries between pixels. Threshold cuts at this level also remove the charge deposited at the corners where particles shared energy with the neighbouring pixels. Increasing the cut further to 30 ToT counts begins to reduce the main signal in the high efficient region.

3.3.6 Charge Sharing

As briefly discussed in the introduction, in the 3D device charge drifts towards the collecting electrode at the centre of each pixel cell. This contrasts with a planar device in which the charge is drifted through the device thickness, which permits diffusion of the charge across pixel cell boundaries and leads to charge sharing. Figure 3.14 shows the positions of the track

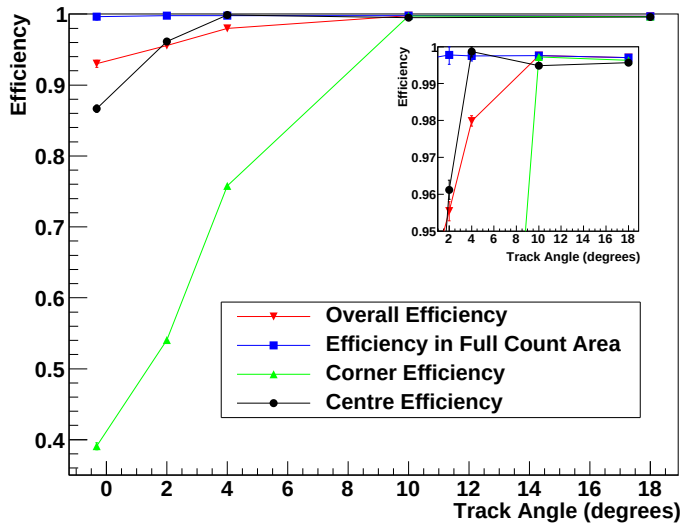

(a)

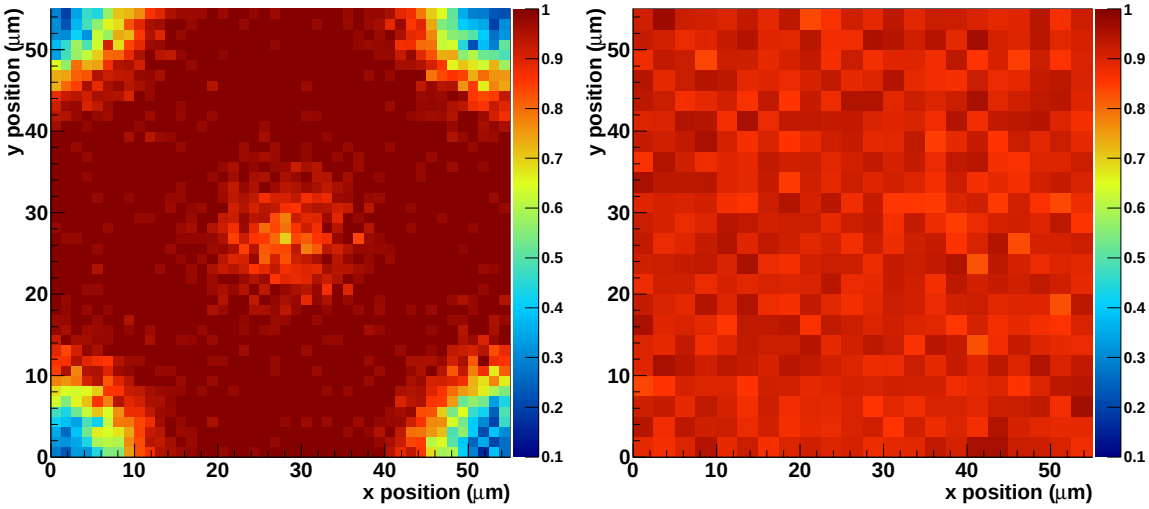

(b) (c)

Figure 3.12: Efficiencies in regions of the pixel as a function of the track angle (a) with an insert highlighting the efficiencies close to 100%. Also shown are pixel maps of the efficiencies with track angles of 0° (b) and 10° (c) showing the fully efficient response across the entire pixel with tracks at 10°.

intercepts of the particles mapped onto a unit pixel cell in the detectors. Single pixel hits, hits creating clusters of two pixels and clusters containing three or more pixels are plotted separately.

The sensor was operated with a bias of 20 V, which is above the full depletion voltage. Single pixel hits in the 3D device can be found to be spread across almost the entire pixel,

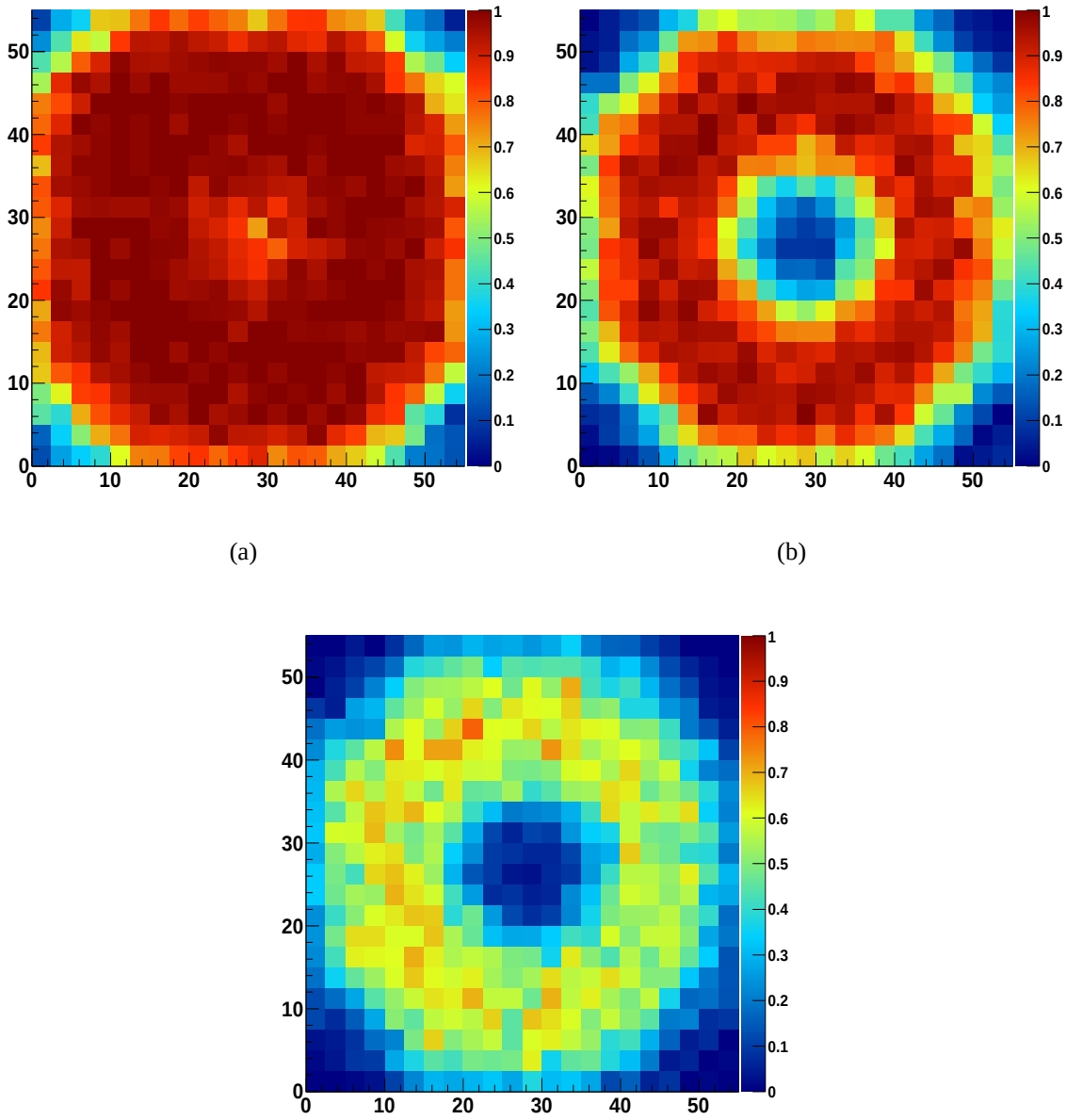

(a) (b)

(c)

Figure 3.13: Single pixel efficiency maps for the 3D device at different threshold settings illustrating the regions of the loss of counts at high threshold values. The threshold cuts shown are at 0 ToT (a), 20 ToT (b) and 30 ToT (c).

in Figure 3.14(a), with a slight reduction at the pixel's edge and corners. Looking at the percentage that multiple hit clusters make up of the total hits in Figure 3.14(d), 14.4% of incident particles share sufficient charge with neighboring pixels to create multiple pixel hits in the detector. Hits along the boundary of two pixels create double hit clusters as expected. Hits in three or more pixels are not seen at the corners of the pixels in the 3D device where

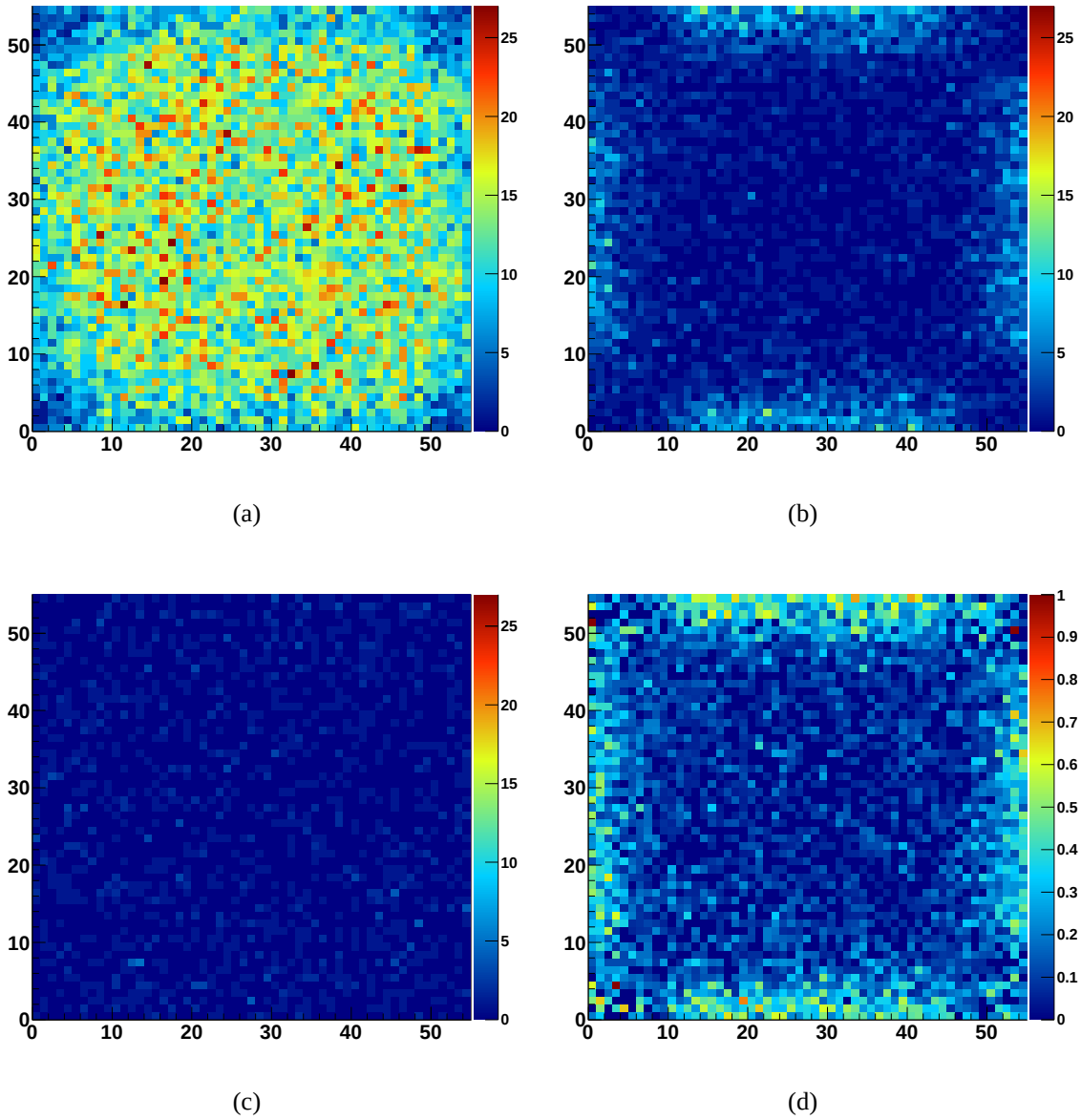

Figure 3.14: Track intercept positions across the 3D pixel matrix in a single pixel cell for tracks of normal incidence, for one pixel clusters (a), two pixels clusters (b) and cluster sizes greater than 2 (c). The location of hits that shared charge between multiple pixels is shown in (d). This is calculated bin by bin by dividing the sum of histograms (b) and (c) by the sum of histograms (a), (b) and (c).

these would appear in a planar device. This is due to the additional loss of charge in the corner electrodes.

An equivalent set of plots for a planar device can be found in [66]. Here, it can be seen that charge sharing occurs with hits up to 10 μm away from the edge of the pixel. Very few single pixel clusters appear in the region closer to the edges than 10 μm. Futhermore, the

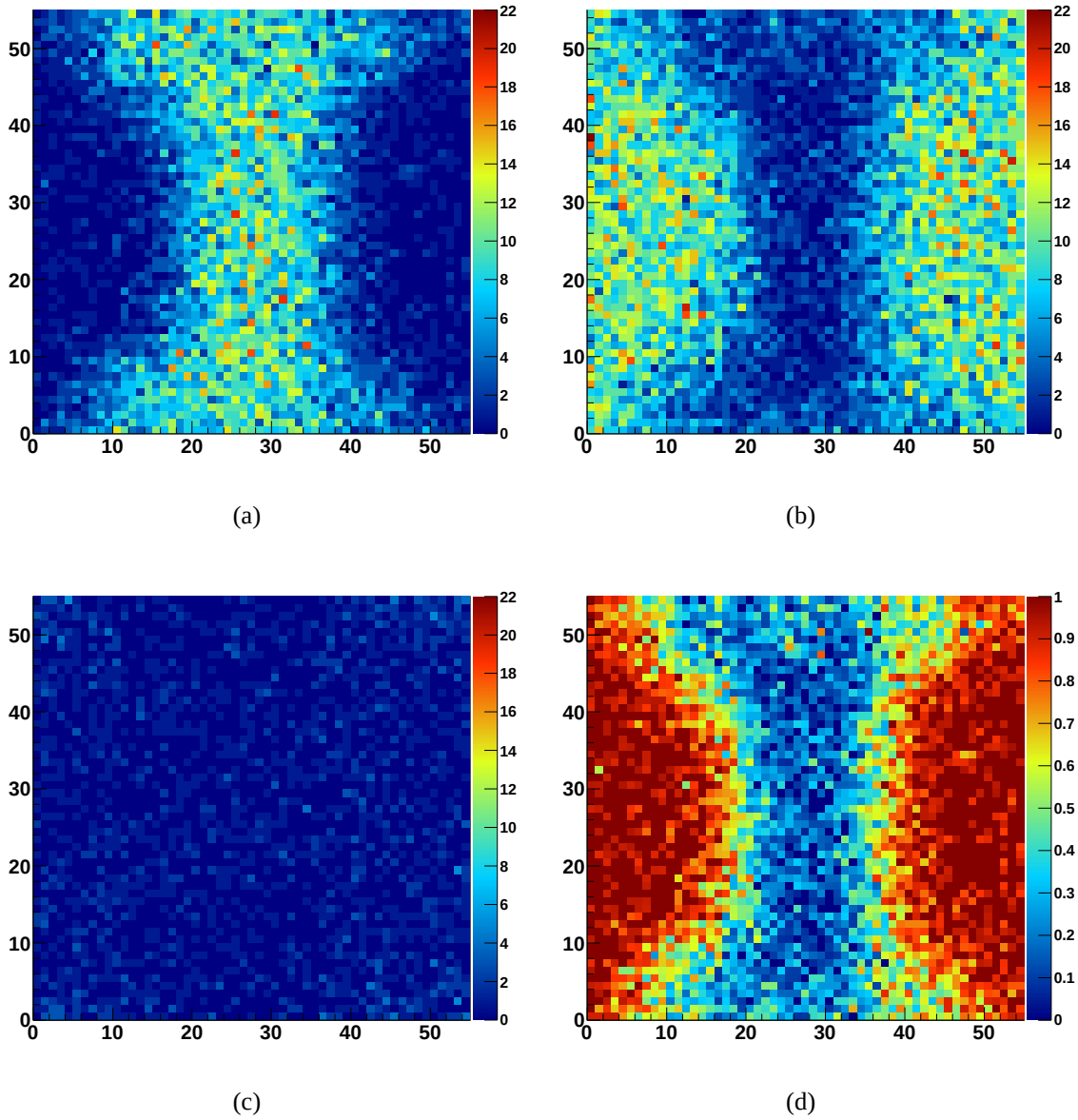

Figure 3.15: Track intercept positions across the 3D pixel matrix in a single pixel cell for tracks of 10° incidence, for one pixel clusters (a), two pixels clusters (b) and cluster sizes greater than 2 (c). The location of hits that shared charge between multiple pixels is shown in (d). This is calculated bin by bin by dividing the sum of histograms (b) and (c) by the sum of histograms (a), (b) and (c).

corners of each pixel consist almost entirely of three and four pixel clusters.

Track position maps for tracks of 10° incidence angle, rotated around the vertical axis, are shown in Figure 3.15. Broadly speaking the one pixel clusters occupy the central region and the two pixel clusters the left and right-hand regions as expected. The 3D detector single pixel cluster region widens at the upper and lower parts of the figure, as charge is lost to the

corner electrodes in the neighbouring cells at these positions. There is no region of the 3D device where clusters of more than two pixels regularly appear.

Figure 3.15(d) shows the percentage of clusters that are composed of two or more pixels. These are now dominating the areas of the pixel away from the central hourglass shaped region.

Charge sharing has some advantages. This is particularly apparent when a detector is required to make a highly position-sensitive measurement. In this application, the charge sharing will improve the resolution well below the pixel size. However, there are some instances where low charge sharing is essential. When a detector is used as an imaging sensor, reducing the charge sharing will improve the image quality. Additionally, in a highly irradiated device it is important to keep the signal level high. This can be achieved by containing the charge within the hit pixel and is made possible more easily with a 3D detector.

3.3.7 Resolution

The 3D sensor has relatively little charge sharing compared with a planar sensor. This is expected from the self-shielding electric-field geometry of the 3D sensor as demonstrated above. In a planar sensor charge drifts through the thickness of the sensor to the collection electrodes and diffusion naturally leads to charge sharing. In a 3D sensor the charge drifts to the collection electrode column and hence tends to remain bounded inside a pixel. As the angle between the sensor and the tracks is varied, the geometry leads to the charge being deposited across multiple pixels. The fraction of single and multiple pixel clusters is shown in Figure 3.16(a). At perpendicular incidence, the measured 3D sensor resolution is 15.81 ± 0.10 μm, which is compatible with the expected binary resolution for a 55 μm pixel (15.88 μm). The optimal resolution obtained was at a rotation angle of 10°, where a resolution of 9.81 ± 0.10 μm was measured. This angle corresponds to the entry and exit points of the track in the silicon being separated by approximately one pixel, and hence maximises the two pixel fraction. This resolution is superior to the expected binary resolution.

As the angle is increased beyond 10°, the resolution degrades due to a larger proportion

of the tracks now being spread over three or more pixels. The variation of the resolution with angle is shown in Table 3.2 and Figure 3.16(b).

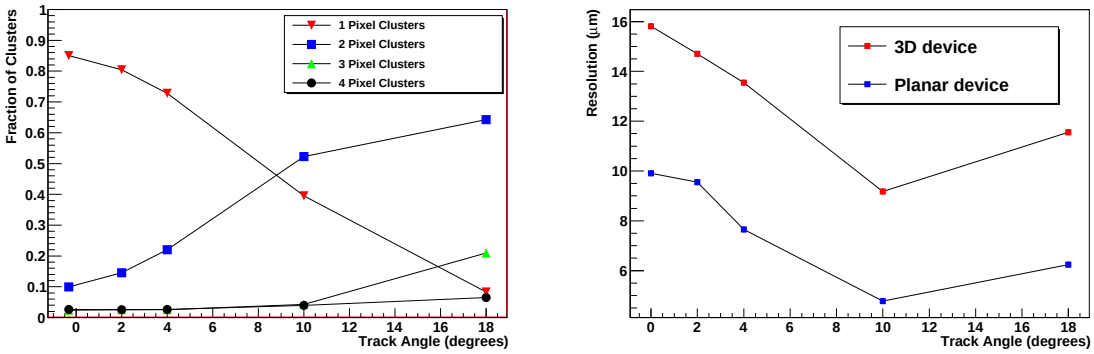

(a) (b)

Figure 3.16: (a) Fraction of single and multiple pixel clusters and (b) resolution in the direction of rotation as a function of the rotation angle for the double-sided 3D pixel DUT and an equivalent planar detector.

Angle (Degrees)	0	2	4	10	18
Resolution (μm)	15.81±0.10	14.70±0.10	13.55±0.10	9.81±0.10	11.55±0.10

Table 3.2: Resolution as a function of track incidence angle in the direction of rotation for a 3D device.

The equivalent resolution measurements for the planar device are shown in Table 3.3 [22]. These show the same relative pattern as the 3D device with an improvement in the resolution with rotations up to 10° and then a small degradation in the resolution with greater angles. The higher level of charge sharing present in the planar detector explains the improved resolution at all angles of rotation when compared with the 3D detector.

Angle (Degrees)	0	2	5	10	18
Resolution (μm)	9.91±0.10	9.55±0.10	7.65±0.10	4.78±0.10	6.24±0.10

Table 3.3: Resolution as a function of track incidence angle in the direction of rotation for a planar device [22].

3.4 Conclusions

The detector response to a high energy pion beam has been mapped across a unit pixel cell. Efficiency measurements show a total pixel efficiency of 93.0±0.5% at normal incidence and with a bias voltage of 20 V. Specific areas of a single pixel will have different efficiencies. The area of high counts away from any electrodes has an efficiency of 99.7±0.5%. The efficiency loss in the pixel is shown to be due to loss of charge in the region of the electrode columns. For the central electrode the efficiency drops to 86.7±0.5% and at the corner additional charge sharing effects causes the efficiency to decrease to 39.1±0.5%.

The two methods used to measure the effective inactive column radius gave values of 7.5±0.8 μm and 7.6±0.6 μm, in good agreement with the scanning electron microscope measurement of the junction position [37]. However, charge collection in the regions above and below the electrode columns is still observed, and shown to improve as the bias voltage is increased and this region becomes over-depleted. By tilting the angle of the detector by 10° relative to the particle beam the influence of the columns become negligible on the detector efficiency. A full pixel efficiency of 99.8±0.5% is reached across the unit pixel. For future high energy physics experiments, careful consideration of the layout to arrange the detectors such that the angle of incidence of the particles of interest is around 10° or greater. This consideration couples well with the requirement to arrange the silicon for minimum Lorentz angle and to achieve overlap with a multi-module system in a barrel system, and may match the angular acceptance of forward endcaps in some systems.

The different behaviour of the central, corner and main areas of the pixel are distinguished by mapping the energy deposition information available from the ToT mode of the Timepix readout ASIC. The reduced level of charge deposited above the central electrode is observed to be compatible with being from the expected 35 μm height of silicon in this region. The effect of the electric field within the 3D sensor in reducing the charge shared is illustrated by mapping the ratio of multiple-hit clusters to single-pixel hits. This reduces the spatial resolution of the system at normal incidence, since charge sharing in an analogue readout system increases the chance of creating multiple-hit clusters from which a weighted

centroid position can be determined. However, a decrease in the level of charge sharing may be advantageous for highly irradiated detectors which suffer from low signal-to-noise ratios as this ratio is improved by collecting all the signal in a single pixel.

3.5 Edgeless Detectors

3.5.1 Motivation

Standard silicon detectors have a relatively large insensitive region around their active area. This dead region due to presence of multiple guard rings and the clearance for the dicing street of the sensors can extend to more than 500 μm, depending on the detector application and therefore operational requirements. As discussed in Section 2.2.2.1, the columnar electrodes of 3D devices are compatible with slim edge technology [9].

In a silicon sensor the diced surface contains a high density of lattice defects. A significant fraction of these are electrically active. Such a surface will provide a leakage pathway around the device.

The guard rings present around the active detector area produce an effective screening of the electric field in the active area from the region adjacent to the chip cut, isolating the active area from the detector edge, thereby reducing the leakage current on the nearby strips or pixels.

However, the guard ring structure adds an insensitive area around the active pixel or strip region. The maximum practical size of a silicon pixel assembly is limited by the size of the high resistivity float zone silicon wafers (presently 6 inch in diameter), the detector vendor's maximum high yield device size, the ability to flip chip modules Readout Integrated Circuits (ROICs) to the sensor at high yield and with the possibility to connect to the ROIC. The data rate from the assembly may also be a limiting factor unless local data compression is performed. As a consequence of these limitations several detector modules must be used to image large areas. For example, the Excalibur sensor [75] comprises of 3 monolithic silicon sensors with a matrix of 2048 x 512 50 μm pixels, and with each sensor hybridised to 16

Medpix3 ASICs.

To remove inactive regions around each sensor reduced edge or “edgeless” sensors are required. For example, an active area of 315 x 315 mm is required to be competitive with phosphors attached to CCD’s in macromolecular crystallography applications [76]. A similar coverage is required for proton-based tomography application, where both gaps in coverage and overlapping sensor planes result in “ghosts” in reconstructed images [77].

Such sensor designs in conjunction with through-silicon vias (TSV) [78] would also result in a reduction in radiation length, making edgeless sensors a promising option for the particle physics community. Such sensors utilize one of a number of methods to reduce the number of guard rings and their pitch so to increase the active area of tiled detectors, and these are outlined in the next section.

3.5.2 Device Under Test and Readout

A 300 μm thick silicon strip sensor with a Scribed, Cleaned and Passivated (SCP) [79] edge on one side was fabricated in the context of ATLAS planar pixel sensor submission [80]. The slim edge post-processing step was performed by a collaboration of Santa Cruz Institute of Particle Physics and the U.S. Naval Research Laboratory [81] [82] [79]. The strips had a pitch of 80 μm. The cleaved edge left only 2 of the 8 guard rings intact and this is shown in Figure 3.17. The guard rings that were in the cleaved section were connected together to ensure that the other edges were not affected.

The sensor was then characterized using the ALiBaVa DAQ system [83]. The ALiBaVa system is a laboratory test system based on the LHCb Beetle front end readout chip [84] for low noise LHC speed testing of sensors. The hardware is made up of a daughter board and a motherboard. The daughter board contains two Beetle readout chips as well as the circuitry necessary to connect the Beetle chips with the motherboard. The mother board processes the analogue data that comes from the daughter board readout chips and the trigger input signal in case of radioactive source setup or the generation of a trigger signal if a laser setup is used. The system communicates with the PC software via USB. I-V characteristics were

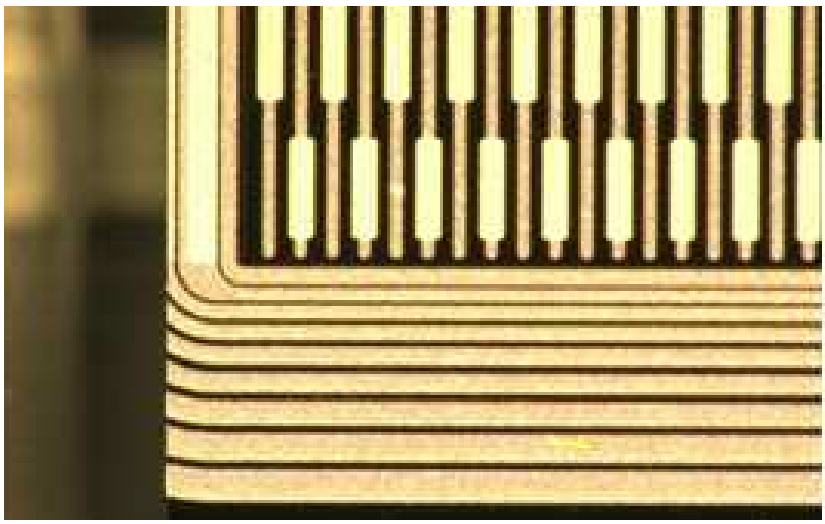

Figure 3.17: The slim edged strip detector tested showing a cleaved edge on the left hand side. The inner ring is the bias rail, with the remaining outer rings the guard rings [81].

taken using a Keithley 237 SMU and are shown in Figure 3.18. For the synchrotron tests, a bias voltage of 100V was chosen to over-deplete the device.

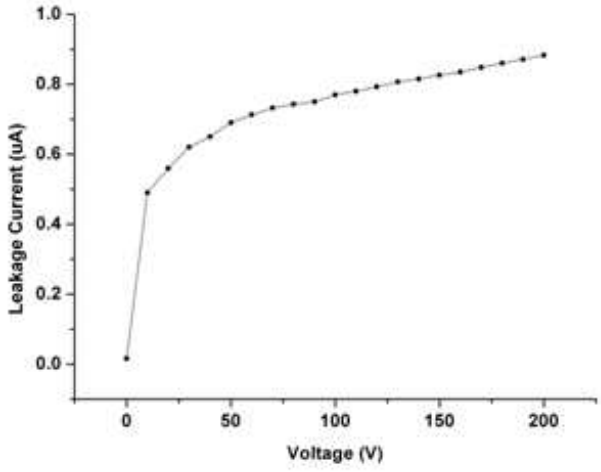

Figure 3.18: I-V Characteristic of the SCP strip sensor under test.

3.5.3 Synchrotron Technique

A micro-focused X-ray beam was used to probe any variation in charge collection efficiency in the detectors near to their edges. The beam was provided by the B16 beamline at the

Diamond Light Source synchrotron research facility. This beam line comprises of a water-cooled fixed-exit double crystal monochromator that is capable of providing monochromatic beams over a 2-20 keV photon energy range. An unfocused monochromatic beam is provided to the experimental hutch. A compound refractive lens (CRL) was used to produce a 15 keV micro-focused X-ray beam.

The size of the micro-focused beam was determined by measuring transmission scans with a 200 μm gold wire. The derivative of these scans gave a beam shape which had a RMS of 4.8 μm and 4.6 μm in the vertical and the horizontal directions respectively. The device under test (DUT) was mounted on precision translational and rotational stages giving six degrees of freedom. The translational and rotational stages had 0.1 μm and 5 μRad precision respectively.

For both detectors orthogonal alignment with the beamline was achieved using a red laser pen. The laser pen was mounted on a support integrated in the beamline and parallel to the beam and the detector was rotated on the stages until the incident beam and its reflection from the sensor surface were co-incident on a surface in front of the laser pen.

3.5.4 Analysis Method

The particular method of analysis employed in this section was constrained by the conditions of the experiment. The data was taken with a continuous x-ray beam and no trigger could be provided by the beamline. This was because with an asynchronous beam there will be a random sampling point. There is a further random element introduced to the measurement by the interaction of X-rays with silicon. As was discussed previously, in Section 2.3.3, for 15 keV X-rays the interaction probability will be based on the photoelectric effect. For X-rays of this energy and the thickness of the device, the interaction probability will be around 30%. Hence, there was an external clock running at 1 kHz used to trigger the readout of the buffer.

The detector was operated at 100 V for the calibration, pedestal and subsequent data taking runs. At each beam position 100 000 frames were collected in which there were on

average 15 000 signal hits. A signal hit was taken to be any event where the total charge recorded in the strips being scanned was above the threshold that was set. This threshold was set in the analysis stage, and could be varied as required. The mean signal size was then calculated by summing the signal in each strip and dividing this by the total number of events. The error quoted is then the standard deviation of this number. A consequence of this method is that the mean signal size will increase as the threshold is increased as lower energy hits will be excluded from the mean. Without considering instances of charge sharing, the mean signal size cannot be smaller than the threshold applied.

3.5.5 Results

Since these devices are slim edge devices, the aim of the measurement was to measure how the efficiency drops as you approach the edge. This measurement was performed on both the cleaved and non-cleaved edges of the device.

Firstly, a pedestal of 100 000 events was recorded. From this, the noise was calculated as the mean value of the magnitude of the dark signal of each strip. This is shown in Figure 3.19, with the strip closest to the cleaved edge labeled as 0. It can be seen from this that the noise in strips rises slightly in the 20 strips closest to either edge, from an average of 3.3 ADC units to between 3.5 and 3.8 ADC units. This rise occurs at both the cleaved edge and the edge with the full guard ring structures. The strip closest to the cleaved edge shows a significantly greater noise level than any other strip. This is thought to be partially due to the proximity of the cut edge, and partially because of the increased noise due to the header of the Beetle chip. The channel was affected by header cross talk on the analogue link between the sensor and the ADC on the DAQ board. This cross talk meant that the pedestal was shifted to two different levels depending on the state of the last header bit on the link. This offset increased the noise of the strip closest to the cut edge by about 2 ADC units.

The strips numbered 14 to 16 were left un-bonded and these strips show a lower level of noise than their neighbours.

In order to test the signal response of the strips, the beam position moved in steps of

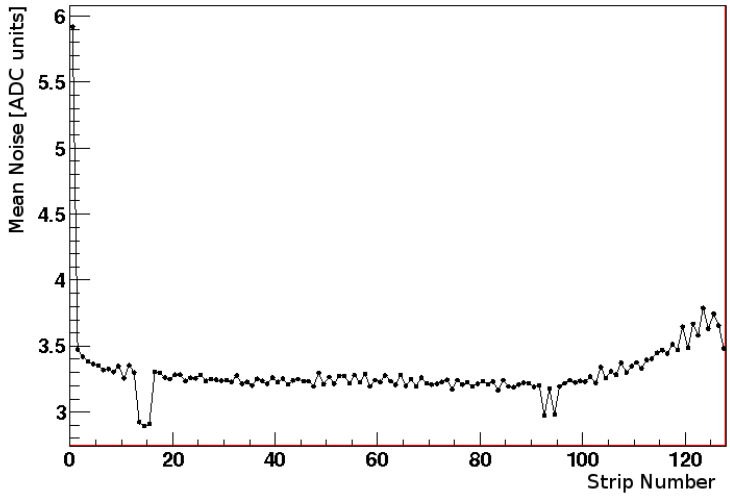

Figure 3.19: The mean noise recorded in each strip with the strip labeled 0 nearest to the cleaved edge.

10 μm perpendicular to the strips over 3 complete strips nearest to the edge (240 μm). The first scan was made covering the 3 strips across over the standard guard ring edge of the sensor and is shown in Figure 3.20. The strips are numbered such that strip 0 is nearest to the edge. With an ADC cut of -10 on the signal, an asymmetric tail was observed on the side of the strips further away from the guard rings and towards the slim edge. When the beam crossed the opposite edge of one strip into the neighbouring strip, the signal returned to the base level within 10 μm. When the beam was in the central 60 μm of any strip, greater than 90% of the signal is collected in that strip. As the beam moved towards the edge 10 μm of a strip, the charge was shared with the neighboring strip. Once the beam moved beyond edge of the last strip (a beam position of 0 μm) the number of signal hits quickly dropped from 15 000 to less than 50. However, the mean of these few hits will still give a non-zero signal. This explains the signal not dropping to zero beyond the edge of the last strip.

With an ADC cut of -40, a uniform signal was observed for the 80 μm of each strip. This cut was much larger than the noise threshold, and so removed both the charge sharing and the asymmetric tails. The mean signal size is greater with the ADC cut of -40 because the lower energy hits are now excluded compared to the ADC cut of -10.

A second scan was then made covering 3 strips over the cleaved (slim) edge side of

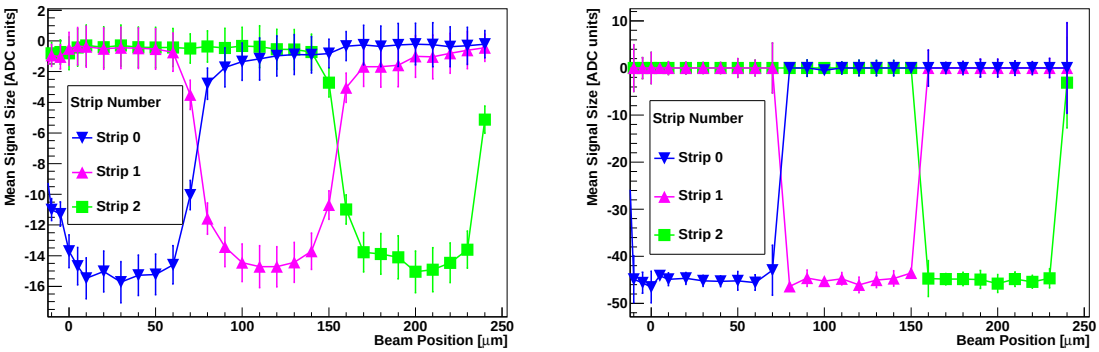

(a) (b)

Figure 3.20: Scan of the edge of the strip detector with full guard ring structures. (a) shows the mean signal size with an ADC cut of -10, (b) has an ADC cut of -40. The edge of the last strip is at 0 μm.

the device. This is shown in Figure 3.21. Again, the strip labeled 0 is the one closest to the cleaved edge. Firstly, with an ADC cut of -10 it was apparent that the strip nearest the cleaved edge had a greater noise level than any other strip. The greater noise level is apparent from the mean signal sizes at beam positions away from strip 0. Here, the baseline value of strip 0 does not return to 0 ADC units as with the other strips. This has a further knock-on effect of increasing the number of hits that reach the threshold. The result of this is that the mean values for the other strips are reduced. The increased noise level only affects the strip closest to the cleaved edge - the strip adjacent to the edge strip shows the same noise profile as any other strip. Similarly to the previous scan, strips 1 and 2 show an asymmetric tail on the side towards the cleaved edge. With a signal cut of 40, the noise from the cleaved edge is removed and a comparable signal profile to Figure 3.21(b) was observed.

The absolute efficiency of the different edge strips is not possible to compute with the experiment described here. Part of the reason for this was that there was a continuous and asynchronous X-ray beam and, hence, no trigger could be provided by the beamline. This meant that although there were 100 000 frames collected for every beam position there was not a constant number of signal hits for each position and it is impossible to say how many photons were not detected by the sensor. The only conclusive measurement it is possible to make between the two edge strips is that for the signal cuts of both -10 and -40 ADC units, they had the same mean signal size. This was -15.3±0.3 ADC units for the -10 cut and

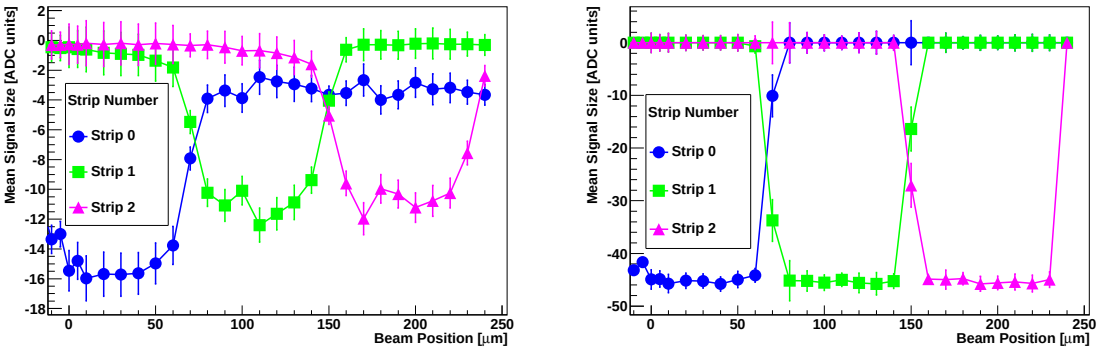

(a) (b)

Figure 3.21: Scan of the cleaved edge of the strip detector. (a) Shows the mean signal size with an ADC cut of -10, (b) has an ADC cut of -40. The edge of the last strip is at 0 μm, and this is around 80 μm from the cleaved edge.

45.1±0.3 ADC units for the -40 cut.

3.5.6 Conclusions

An edgeless detector was successfully characterised at the Diamond Light source using an 11 μm FWHM 15 keV micro-focused X-ray beam. After successful alignment and focusing of the beam, several high resolution scans were made over the edge regions of both devices to quantify by how much the charge collection is affected by the edgeless designs.

Scans of the 300 μm thick silicon strip sensor with edge reduction showed no significant degradation in charge collection for strips nearest the cleaved edge relative to those near the standard guard ring structures. When considering the mean value of the signals larger than -10 ADC units, both the cleaved edge and the non-cleaved edge showed an average charge collection of -15.3±0.3 ADC units. When signals with a mean value lower than -40 are removed, again the two different edges have the same average of 45.1±0.3 ADC units. These results are qualitatively consistent with previous n-type sensor studies [85]. However, they are done on a thinner p-type sensor with a factor of 3 smaller strip pitch. The technique used in this work offers a much higher spatial resolution allowing intra-strip studies. The noise of the strip closest to the cleaved edge is increased, but this effect does not extend to any of the strips further from the cleaved edge.

These results indicate techniques such as SCP and active edge processes offer real potential for reduced edge, tiled sensors for imaging detection applications.

Chapter 4

Transient Current Techniques

In this chapter, the signal current formation in a double-sided 3D detector was probed using Transient Current Techniques (TCT) [86]. An infra-red laser with a picosecond pulse length was used to inject electron-hole pairs at different positions within the detector. By analysing the current signals recorded, the collected charge and the velocity of charge carriers can be determined. This is reported for the device before and after irradiation.

4.1 An Introduction to Transient Current Techniques

In a Transient Current Technique (TCT) measurement, free carriers are created in a detector by a short laser pulse [87]. The drift of these carriers induces a current pulse, as shown in Ramo's Theorem and Equation 2.10 in Section 2.3.5. There are multiple advantages accrued by using transient current measurements. Firstly, the precise location of the injected charge within the device can be accurately controlled. An analysis of the induced current waveform can provide an insight into the electric field of the device, giving a lot more information than an analysis of the charge. Another advantage of studying the induced current is that the sign of space charge in a device can be observed directly.

Typically, two different wavelengths of laser will induce different currents. A red laser has a penetration depth of 3.3 μm with a wavelength of 670 nm and at a temperature of 273 K into silicon. The penetration depth is determined by the position at which the intensity has

dropped to 37% of its initial value, according to the Beer-Lambert Law. This will generate charge carriers very near to the illuminated surface in the silicon device. This is useful if the charge is generated near to one type of collection electrode as then the signal will be dominated by the other type of carrier. This method is often referred to as either electron or hole injection. In reality, it is impossible to inject the charge an infinitesimally small distance from the electrode - the beam will attenuate and the charge deposited will decrease exponentially.

The alternative method, and the one used in this chapter, is to use an infra-red laser. In this case, the laser will penetrate several millimeters into the device. Charge carriers will then be induced all along the path of the laser.

4.2 Experimental Method

Spatially-resolved edge and surface TCT measurements were performed of a double sided 3D silicon strip detector. Short, 3D, p-type strip detectors (produced at CNM in Barcelona) have been used for this study [37]. A photograph of the strips is shown in Figure 4.1 and a schematic of these detectors is displayed in Figure 4.2.

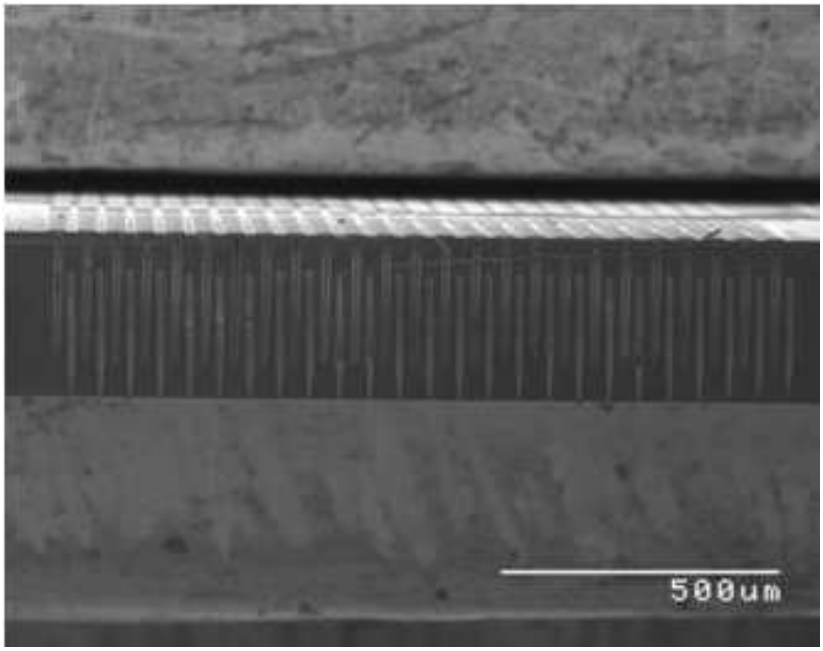

Figure 4.1: Photograph of the strip detector.

The strip detectors had a substrate thickness of 230$\pm$15 micrometers and a strip pitch of 80 micrometers. The non-active columns that formed the electrodes had a diameter of 10 micrometers, and were 170$\pm$10 micrometers deep. The p-type columns were not fully etched since the strip detectors were placed at the edge of the wafer during fabrication where the Reactive Ion Etching process was not uniform. The columns were arranged as a square array with the same type columns at a pitch of 80 micrometers. The array of junction columns were displaced by half a pitch in both orthogonal directions to the ohmic columns, such that they lie at the centre of the square formed by the ohmic columns. The n-type junction electrodes were connected together with 20 micrometer wide aluminium metallisation to form the strips. Each readout strip was 4 mm long and consisted of 50 junction columns connected together. The Ohmic electrodes were connected together on the back-side of the device with a uniform aluminium contact. These devices use a similar technology as to that used for the ATLAS IBL 3D pixel sensor candidates [33]. The detectors were tested both prior to irradiation and after irradiating with reactor neutrons from the Jozef Stefan Institute reactor [88], to a dose of 5 x 10^{15} 1 MeV equivalent neutrons/cm^2. Studies were performed into the effect of varying bias voltage and also the effect of annealing for up to 300 minutes at 60 °C on the irradiated sample. Conversion of the annealing time at high temperatures to a longer time at room temperature was achieved by calculating the accelerating factor from the relevant activation energy and frequency factor [89]. 300 minutes is equivalent to the amount of annealing expected for 7 years of operation in an LHC experiment, where (for example in ATLAS) it is estimated that the silicon sensors will be at 20 °C for 30 days per year of operation.

An IR laser (1064 nm, pulse width of 0.1 ns) was used to scan the devices with the spot focused on the centre of the bulk silicon. The spot had a diameter with a FWHM equal to 7 micrometers. This was measured by scanning across the aluminium strip on the top surface of the detector. The distance the laser moved in order for the signal to drop from the maximum value to the minimum value was taken as the width of the beam spot. The detector itself was mounted on a copper block with a Peltier element that allowed the temperature to

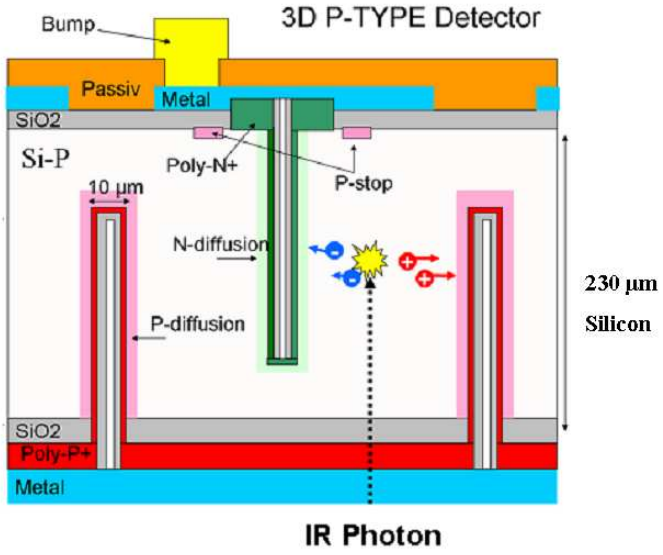

(a)

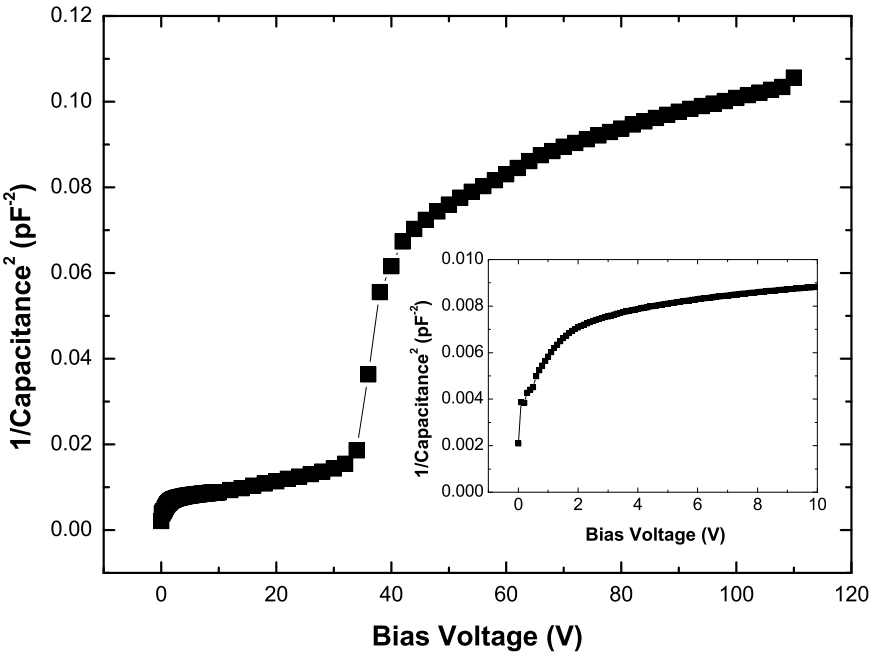

(b)

Figure 4.2: (a) Schematic of a p-type double-sided 3D detector and (b) the related CV curve. The CV curve insert shows the inter-column region depletes at 3V while the main plot shows the under-column region depletes at 40 V [24].

be controlled from -20 °C to 60 °C. This was then placed in a sealed dark box that could be flushed with dry air. The aluminium box also shielded the samples from outside radio sources. A Picosecond Pulse Labs Model 5531 bias-T was used to connect the high voltage

power supply. This has a bandwidth of 1 MHz up to 10 GHz. This then decoupled the readout electronics from the high voltage with a capacitance of 2.2 nF. Eleven strips adjacent to one another were bonded up, with the central strip connected to a wide band amplifier (0.01 - 1 GHz) for readout. An oscilloscope then digitized and recorded the induced currents produced by the laser illumination. The oscilloscope provided a maximum of 10^9 samples per second at the analogue band-width of 500 MHz.

Scans with a step of 2.5 micrometers were performed over the surface of the device in both orthogonal directions, illuminating either the front surface or the cut edge (perpendicular to the strips). The data was recorded for the 10 ns before the laser pulse and the 40 ns after the laser pulse. The DAQ was triggered on the pulse from the laser driver, for each laser pulse with the final result for any illumination position taken as the average of many pulses. The laser pulses generated charge pairs along the path of the beam. The total signal is therefore an integration of the device's response throughout its depth. Illumination of non-active areas (metallisation or columns) resulted in reduced signals. The baseline is the background signal and this is required to be a constant during a measurement. The baseline was corrected based on normalising to the 10 ns prior to the pulse and extrapolating that to the rest of the signal. For a full description of the TCT technology and methods, refer to reference [87].

In order to reduce the diffraction of the light and hence reduce the beam width, for the edge illumination studies, the cut edge was polished prior to illumination. The laser beam illuminated the cut edge perpendicular to the aluminium strips on the top surface. The strip connected to the amplifier was several millimetres from the cut edge. In order for the laser light to reach the readout strip, around 40 inactive strip needed to be passed through. In the regions where the beam traversed purely the silicon substrate, no degradation in the signal would occur. However, when the photons had to pass through multiple, inactive columns there was a consequential loss of signal due to reflections at the silicon, polysilicon and air boundaries within the columns. From an analysis with Fresnel's equations, assuming pure silicon between the columns and polysilicon within the columns [90], this was estimated to lead to around a 4% loss of signal due to reflections per column. After 40 columns,

only around 20% of the initial signal remained. The irradiation and edge polishing were completed at the Jozef Stefan Institute in Ljubljana [91].

The TCT experiment was undertaken in an atmosphere of dry air, with the irradiated samples maintained at a temperature of -20 °C. The non-irradiated samples were kept at room temperature with no temperature control, causing a greater leakage current than for the equivalent irradiated sample. The leakage current was recorded for each setup. Annealing was achieved in situ by warming to 60 °C for intervals of 20, 40, 100, 300 and 600 minutes corresponding to room temperature annealing times of between 8 days and 200 days.

4.3 Results

4.3.1 CV and IV Characteristics

Figure 4.2(b) shows the capacitance-voltage characteristics of a non-irradiated short strip 3D detector. The curve demonstrates two distinct sections which relate to the two depletion regions: the inter-column region depletes at 3 V while the main plot shows the under-column region depletes at 40 V [24]. The leakage current characteristics are shown for each step in Figure 4.3. All the leakage currents after irradiation were measured with a detector temperature of -20 °C. The device before irradiation was measured at 20 °C and scaled to the equivalent at -20 °C using Equation 2.17. The lateral full depletion voltage of the irradiated device is around 100 V [68], corresponding to the plateauing of the leakage current around that bias voltage. The increase in the leakage current once irradiated can be used to calculate α, the related damage factor, using Equation 2.18. Given the dimensions of the device (0.5 cm by 1 cm) and the leakage current scaled to 20 °C (0.42 mA) a value for α of 7.77 x 10^{-18} A/cm was calculated for the sample prior to annealing [64]. For bias voltages above this value, soft breakdown occurs as is often the case in irradiated detectors. Annealing decreases the leakage current of the device.

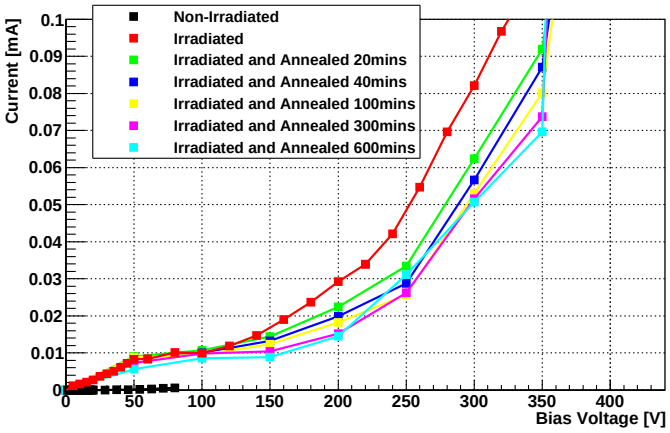

Figure 4.3: Leakage current against reverse bias voltage for the non-irradiated and irradiated sample and for each annealing step.

4.3.2 Edge TCTs for Non-Irradiated Sensors

The TCT measurements where the cut edge was illuminated were performed only for non-irradiated devices and are therefore shown first. Waveforms were collected for laser pulses at a series of different positions on the cut edge and shown in Figure 4.4. The back-side, p^+-type, ohmic columns extend downwards from the top of the figure and the front-side, n^+-type, junction columns extend from the bottom. The charge collection plot was obtained for an integration time of 20 ns and a bias voltage of 20 V. The collected charge was recorded as a negative signal. As the laser light penetrates deep into the device, the signal produced is due to the device's response from charge generated throughout the detector. Therefore, the signal observed at the position of the columns is due to charge generated in the silicon in front of and behind the columns as well as the column itself. The columns that the laser beam passes through present boundaries (such as between the silicon and polysilicon in the columns). Some of the photons will then be reflected and there will then be fewer charge carriers produced afterwards. There is no correction made for this effect.

Areas of high charge collection between areas of low charge collection are observed. The areas of low charge collection correspond to the positions of the columns [36]. The bias voltage of 20 V is greater than the lateral depletion of 3 V, but less than the full depletion beneath the columns of 40 V.

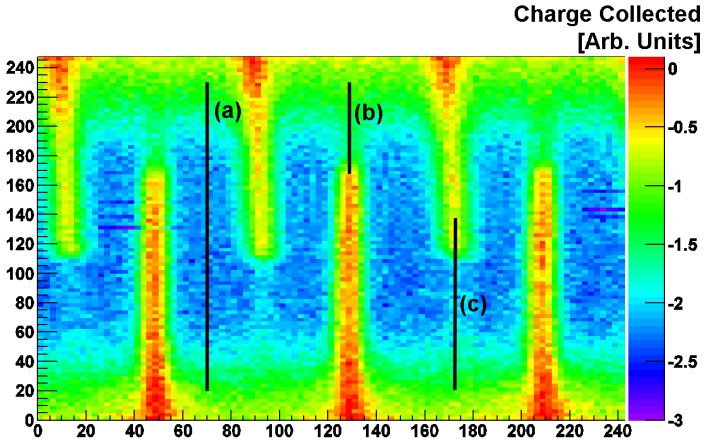

Figure 4.4: Charge collection map for non-irradiated device with edge illumination. Bias voltage was set to 20 V. Lines (a), (b) and (c) correspond to the waveforms in Figures 4.5(a), (b) and (c). Columns extending from the top of the image (at x-positions 10, 90 and 170 μm) are the p-type, ohmic columns, and the opposing columns (at x-positions 50, 130 and 210 μm) are the n-type, junction columns. The areas of more negative signals have the greater charge collection. The x and y axes are distances in micrometers.

The waveforms from which the charge collection map was created are shown in Figure 4.5. From these, the major peak of the signal and the majority of the charge was collected within the first few nanoseconds but an integration time of 20 ns was required to fully collect the charge. The figures show only the initial 10 ns in order to improve the clarity of the initial peaks. From 10 ns to 20 ns, the signals merely degrade to the baseline level. For longer integration times, a reflection of the signal along the cable between the amplifier and the oscilloscope caused an erroneous result to be produced. Another aspect of the charge collection that can be analysed with the waveforms is the rate of charge collection. When considering illumination for positions between the columns, shown in Figure 4.5(a), the earliest peaks and consequently the fastest signals occur in the centre of the device, shown for waveforms collected at 140 and 170 μm. This corresponds to the area of highest field strength [36]. In the region of high collection efficiency below the columns seen in Figures 4.5(b) and 4.5(c)) the total charge collected is constant. However, the collection of charge takes a longer time as the position of illumination moves away from the column, as shown in the waveforms at 230 μm in Figure 4.5(b) and 80 μm in Figure 4.5(c). The columns of each type appear to have physical differences between them. The front-side, junction columns

appear to penetrate to 170 μm whereas the back-side, ohmic columns only appear to reach 135 μm.

The data collected for a scan between the two column types as a function of position from the back (0 μm) to the front (245 μm) side of the detectors were used to determine the charge collection profile at different bias voltages, as plotted in Figure 4.6. The collected charge was measured by integrating the current in the 20 ns after the laser pulse. At 0 V there is some charge collection due to the built in potential creating a small depletion region around the n-type columns. It can be seen that the charge collected in the inter-column region saturates at voltages above the lateral depletion voltage of 3 V. At a bias voltage of 4 V, just above full lateral depletion, full charge collection is obtained from 70 μm to 180 μm. At higher bias voltages the charge collected in this region remains constant, while the region extends in both directions, such that at 20 V full charge collection is obtained from 40 μm to 190 μm. 50% of full charge collection is obtained from 15 μm to 215 μm at this bias voltage. The assymetry associated with the top and bottom of the detector is due to the difference in the way the opposing edges deplete - below the ohmic columns deplete earlier than above the junction columns.

Maps of the charge collected over the entire edge of the device were obtained for increasing bias voltages, and shown in Figure 4.7. It can be seen that the charge collected increases with the bias voltage. The inter-column region is depleted at biases of 4 V and above, with the region beneath the columns depleting at greater biases. A low field region with reduced charge collection can also be seen where the columns connect with the front and back surfaces of the detector. This low-field region reduces in size as the bias voltage increases.

From the charge collection maps the widths of the p and n-type columns were calculated and then compared to previous measurements [66]. Gaussian curves were fitted to the charge collection at the mid-depth of the device (130 μm) at each bias point, with the FWHM taken as the width of the column. This is displayed in Figure 4.8. Bias voltages below the depletion voltage (3 V) were not included in the calculation of the average as the edges of the columns

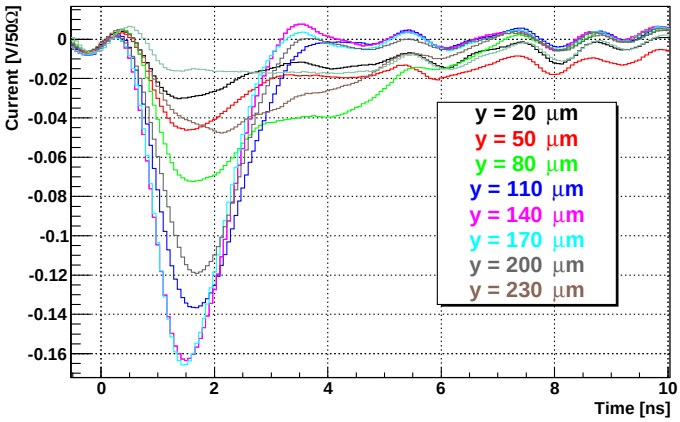

(a)

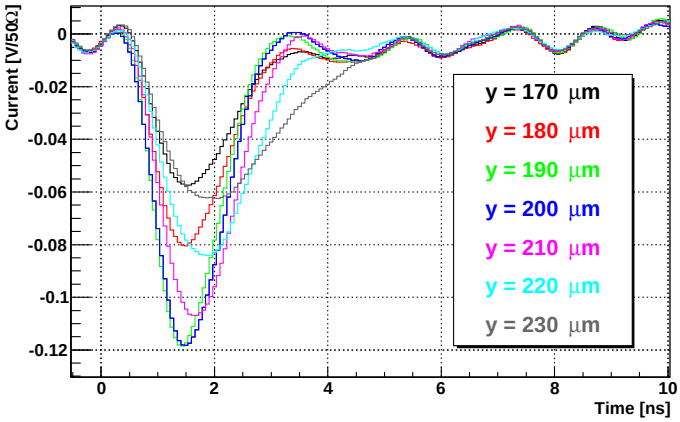

(b)

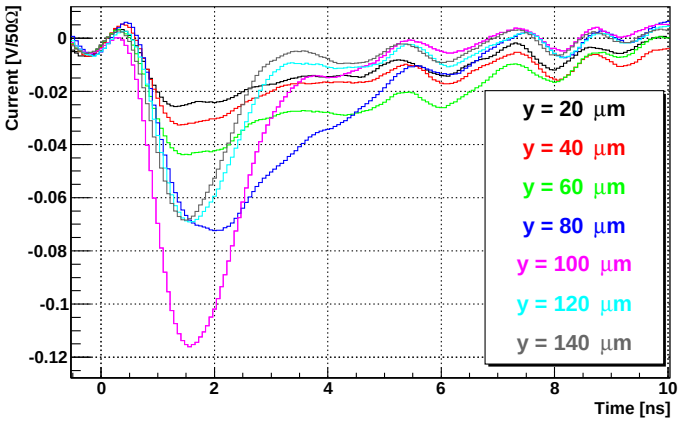

(c)

Figure 4.5: Waveforms resulting from illumination with a bias voltage of 20 V. Waveforms (a), (b) and (c) correspond to the lines in Figure 4.4. An increase in the time required for the peak charge shown as the position moves towards the edge of the device.

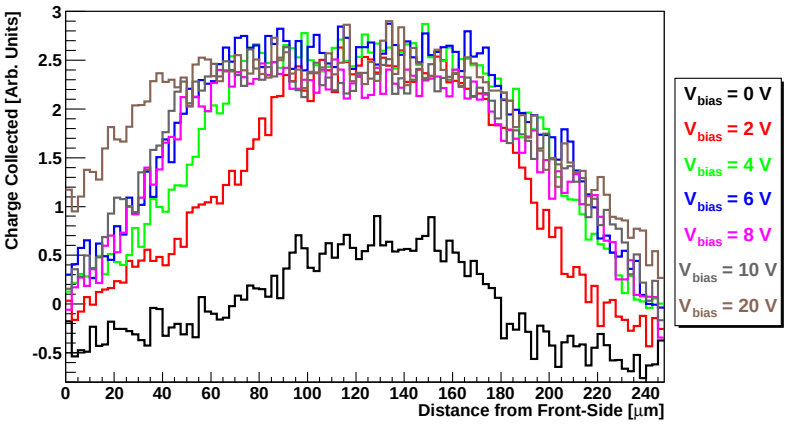

Figure 4.6: Charge collected as a function of the distance from the front-side of the detector, at different detector biases. The distance is measured from 0 μm at the front-side of the detector to 245 μm at the back-side of the detector. The lateral illumination position was halfway between n-type and p-type columns.

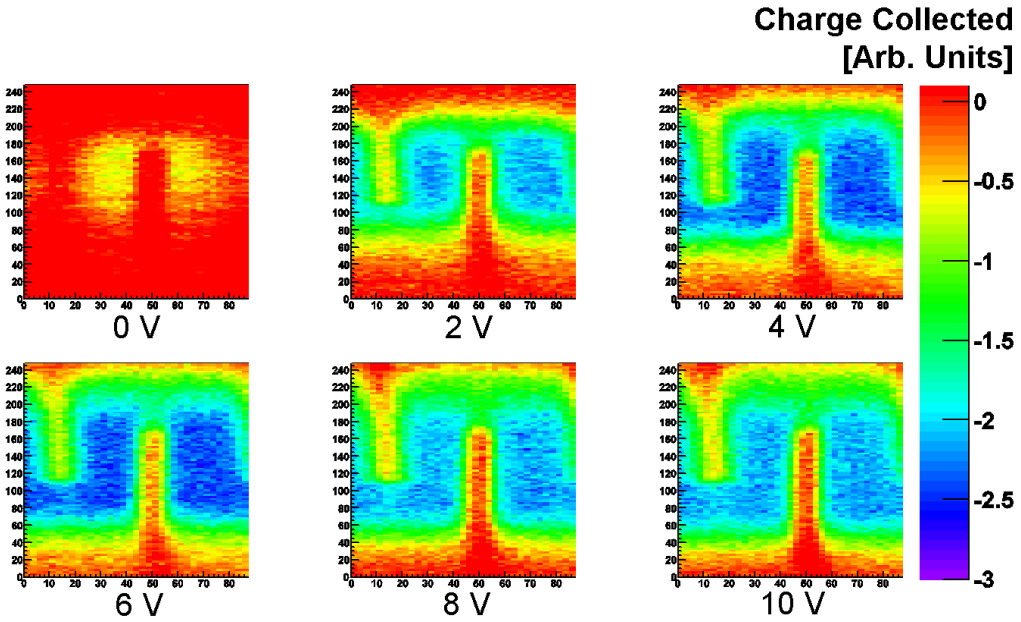

Figure 4.7: Charge collection maps with edge illumination, with bias voltages increasing from 0 V (top left) to 10 V (bottom right) in steps of 2 V. For the charge collection at 20 V, refer to Figure 4.4.

were less well defined. This gave an average value of 7.30±0.03 μm for the p-type column and 9.18±0.03 μm for the n-type column. This agrees with the previous analysis [66].

The rise time of the waveforms is the time taken for the amount of charge collected to increase from 10% to 90% of the maximum [91]. For our system this varied from 0.5 ns to 0.75 ns. By fitting a second order polynomial to this range, any trapping effects can be ig-

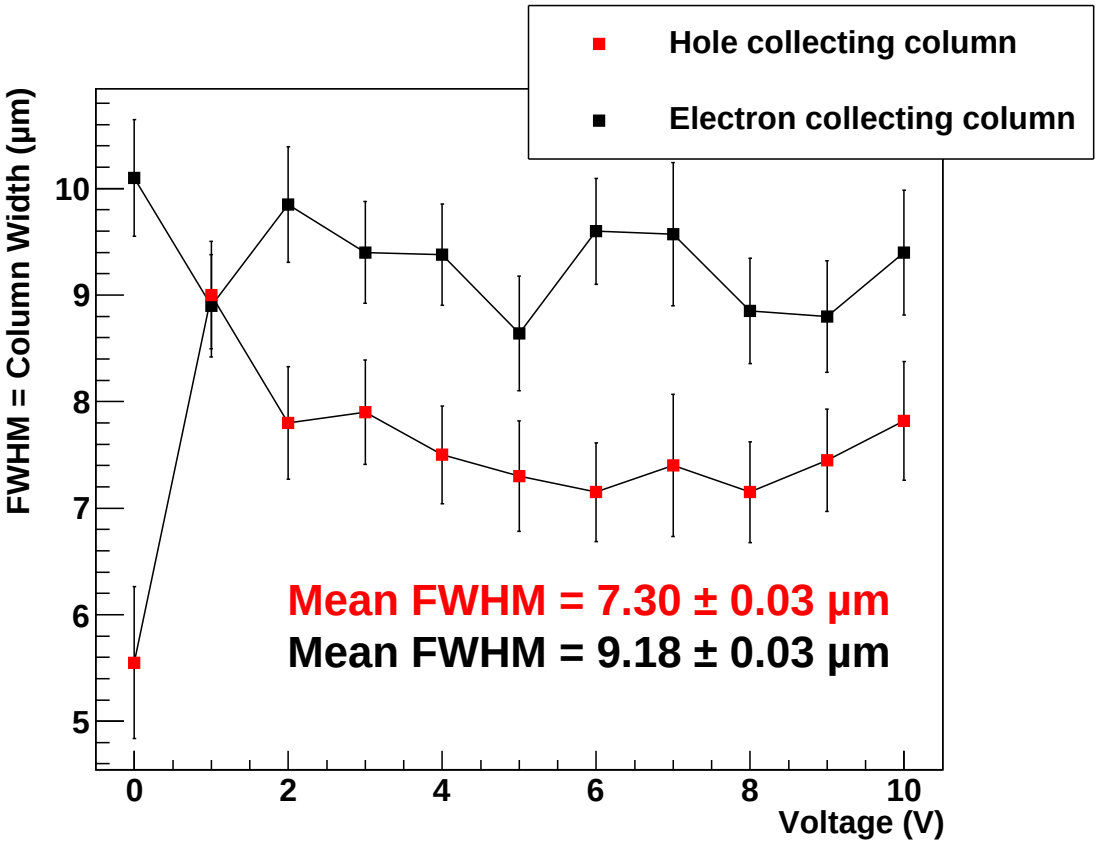

Figure 4.8: FWHM values for increasing bias voltages. Average calculated for bias voltages above the depletion voltage of 3 V.

nored and the velocity profile of the charge carriers can be determined from the current. The velocity is defined as the gradient of the second order polynomial, and increasingly negative values result from higher velocities. It is not possible with this technique to determine the contribution towards the velocity derived from either the electrons or holes independently. This method assumes that all of the charge carriers were generated in the same field. This is certainly true in the region of overlap in the columns.

Velocity maps were produced for edge illumination, shown in Figure 4.9. Figure 4.9(a) shows the velocity of a region with a bias voltage increasing from 0 V up to 10 V. Figure 4.9(b) shows a larger region with a bias voltage of 20 V.

Firstly, every position within the detector shows an increase in velocity as the bias voltage increases due to the uniform increase in the electric field with bias voltage. This is in contrast to the charge collection, shown previously in Figure 4.6. Whereas the full charge is collected in 20 ns at 4 V, the carrier velocity and therefore electric field continues to increase with bias

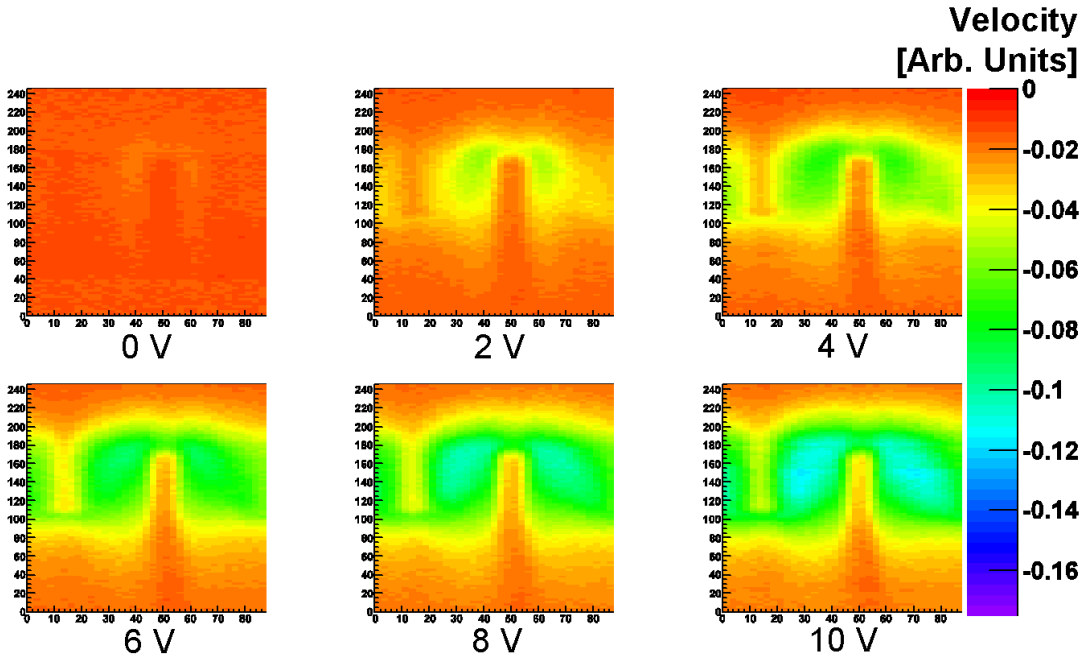

(a)

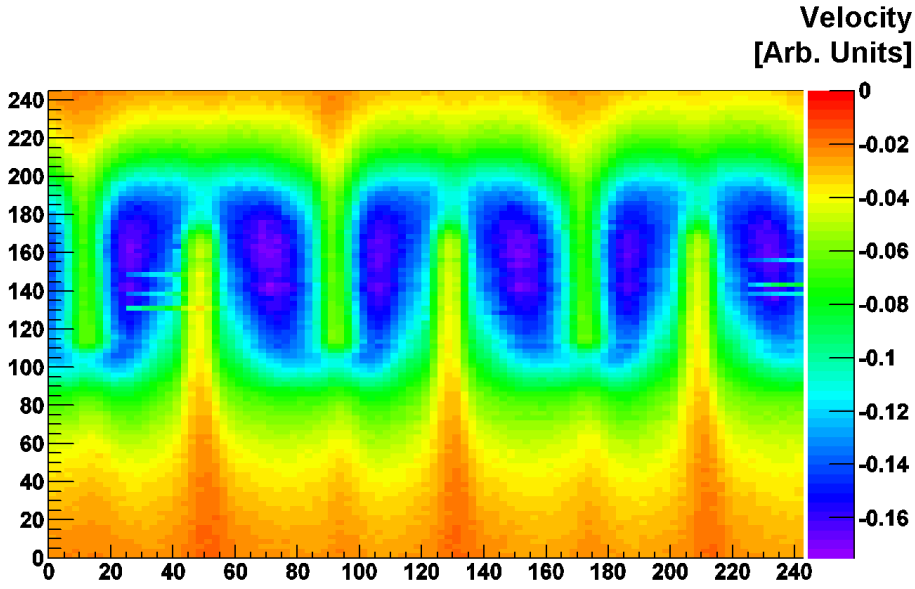

(b)

Figure 4.9: Velocity maps of a non-irradiated sensor with various bias voltages and edge illumination. (a) shows the effect of increasing the bias voltage from 0 V to 10 V. (b) shows the effect of a bias voltage of 20 V. Larger negative values result from larger velocities as a result of the negative signal.

voltage. Even at 20 V, it can be seen that the velocity is non-uniform throughout the device unlike the highly uniform charge collection map. The maximum velocities, shown in Figure 4.10, increase with the square root of the bias voltage and are suppressed by the saturation

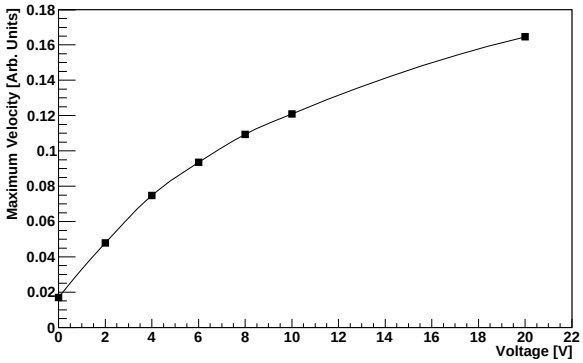

Figure 4.10: Magnitude of the maximum velocities of charge carriers shown in Figure 4.9.

of the electron's velocity in the central region. Also, if the charge collected and the carrier velocity at 40 μm from the front-side of the device were compared for a bias voltage of 20 V, it can be seen that although there is only a small carrier velocity relative to the middle of the device there is close to full charge collection due to the short distance traveled by the carriers. Secondly, the detector has a greater active volume at higher bias voltages because the low-field region near the surfaces is still depleting. At 2 V only around 100 μm of the sensor shows full charge collection, rising to the full 230 μm at 20 V.

The velocity given for an illumination position within a column is non-zero because of the active silicon before and after the column that the beam also passes through. When considering the vertical line passing from the column tip to the surface, there is a peaked velocity close to the column tips for both the n and p-type columns. This is due to the high electric field in these regions.

The peak velocity below the columns (at 100 μm and 200 μm) is equivalent to the velocity at the same position in the inter-column region because the signal is dominated by the charge carriers moving in the active silicon away from the column and the high fields at the column tips are obscured.

4.3.3 Spatially Resolved Top Surface TCTs for Non-Irradiated Sensors

TCT measurements were also performed for illumination normal to the top surface of the non-irradiated sensor. Again, waveforms were collected for laser pulses at a series of posi-

tions across the surface. A schematic of the top surface being scanned is shown in Figure 4.11(a). The current induced on a collecting electrode is related to the charge produced and the weighting field by the Shockley-Ramo Theorem [56]. A simulation of the weighting field for the strip devices tested is shown in Figure 4.11(b). This weighting field simulation was calculated using Synopsys TCAD.

According to Ramo's Theorem, the signal induced on the electrodes of the detector are due to the movement of the charge carriers inside the device. This is given as a dot product of the velocity vector of the charge carriers and of the weighting field. Therefore carriers that experience a large change in the weighting potential during their movement through the device induce more signal than those that travel through regions of small weighting field change. This effect is exploited in the characterisation of planar devices with front and back-side alpha or short wavelength illumination to obtain the charge collected from individual charge carrier types. For a 3D detector, the situation is slightly different. Illumination close to the n+ junction column will result in the holes produced inducing the majority of the signal; while illumination close to the p+ ohmic column will result in a signal dominated by electron movement. Illumination mid-point between the junction and ohmic columns gives rise to a signal due approximately equally to both electrons and holes.

Figure 4.12(a) shows a series of waveforms starting at the electron collecting column and moving in steps of 10 μm perpendicular to the strip. Figure 4.12(b) shows another series of waveforms, this time progressing from the electron collecting column at 45° to the strip. For both data sets, the waveform at 0 μm show a reduced response. This is because the majority of the laser pulse is reflected by the metallised strip with the rest being caused by the extremities of the beam spot. At 20 μm from the electron collecting column, the waveforms display two major peaks. There are several interesting effects inside the device that can be seen from the current pulses obtained and shown in Figure 4.12.

Figure 4.12(a) and 4.12(b) show that for over depletion, 62 V bias, the signal duration is of the order of 3 ns with a second peak, of 2 ns duration, occurring a nanosecond after the first. The origin of the second peak is at present not fully understood, but is suspected to

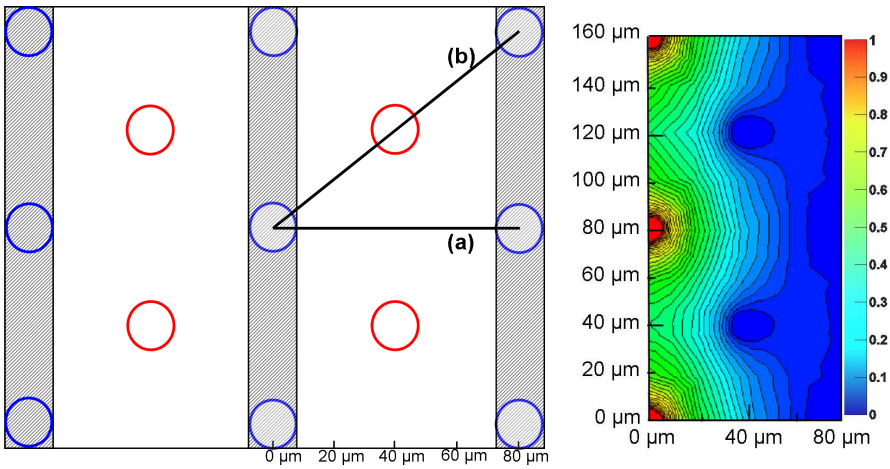

(a) (b)

Figure 4.11: (a) shows a schematic of the top surface that was scanned. Lines (a) and (b) correspond to the waveforms in Figure 4.12(a) and (b). Positions of n-type columns (blue circles), p-type columns (red circles) and strips (hatched areas) have been indicated. (b) is a simulation of the weighting potential for the device, with contour lines showing areas of equal potential. Each contour line represents a change of 0.03 V in the weighting potential. The cross-section is halfway down the device. Only the columns on the left hand strip were biased, which is why the weighting potential is not symmetric about the centre of the x-axis.

be due to the column non-overlap region of the device. The structure of the main first peak depends on illumination position and bias voltage. Figure 4.12(a) shows the waveforms for different illumination positions along line (a) shown in Figure 4.11(a). The signal for illumination at x = 0 µm, close to the junction column, shows a signal that has a falling magnitude with time. This is after a very fast rise in the signal due to the velocity of the signal charge carriers falling with time. This signal is dominated by the movement of holes away from the junction electrode towards the ohmic electrode, and therefore from regions of high to low space charge. The signal at x = 40 µm, corresponding to a position between two ohmic columns and 40 µm away from the strip, is dominated by the movement of electrons created between two ohmic contacts drifting to the junction electrode. The movement of holes to the ohmic contact will not induce significant signal as the change in weighting potential over this region is small, as can be seen in Figure 4.11(b). The waveform shows an increasing signal with time which is as expected for the electrons moving into a region of higher space charge, and consequently a higher electric field, and therefore moving with increasing speed with time. The signal produced at x = 20 µm is due to both the movement of

electrons and holes in approximately equal measure. The rise time of the signal at x = 20 μm is faster than that at x = 40 μm due to the higher electric field at this point and therefore higher carrier velocities. The hole signal will take a little longer than the electron signal due to their lower mobility. This is clear in the wider signal compared to that from x = 40 μm, which is in fact due to electrons moving over twice the distance as for the x = 20 μm signal.

The x = 20 μm signal exhibits three bumps. The first reduction in current (falling side of the first bump) is due to the movement of holes going from a region of higher to lower space charge. The second bump is due to the electron signal dominating. The electrons again move to a region of higher space charge and therefore give rise to a signal with rising magnitude with time, as observed. The falling edge of this bump is due to the collection of electrons. The third bump is due to the movement of holes and is due to the fact that the hole velocity increases slightly as it approaches the p+ ohmic columns.

The waveforms shown in Figure 4.12(b) are very similar to those shown in 4.12(a). These are due to illumination at positions along line (b) in Figure 4.11(a) which joins a junction column to an ohmic column. The significant differences in the waveforms of Figure 4.12(b) are that the rise time of the signals produced at x = 20 μm and x = 40 μm are very similar. The waveforms of Figure 4.12(a) showed a significantly slower waveform at x = 40 μm. This is due to the fact that along this line the electric fields in the device are higher than at the point between two ohmic contacts (Figure 4.12(a) point x = 40 μm) and therefore there is little difference in the velocities of the charge carriers for these two illumination positions.

At 60 μm, a bipolar signal is observed, due to the electrons being collected by the adjacent columns and inducing a signal of opposite polarity. This 60 μm position is outside of the unit cell formed by the p-type columns at the four corners and the strip running through the centre. Electrons generated at this position will travel to the strip neighbouring the collecting strip. The bipolar peak results from the electrons having no effect on the collecting strip and thus integrating to zero. The holes generated here move to the same column as at a point any other distance along the line, however the hole signal is suppressed in this region because of the low weighting field.

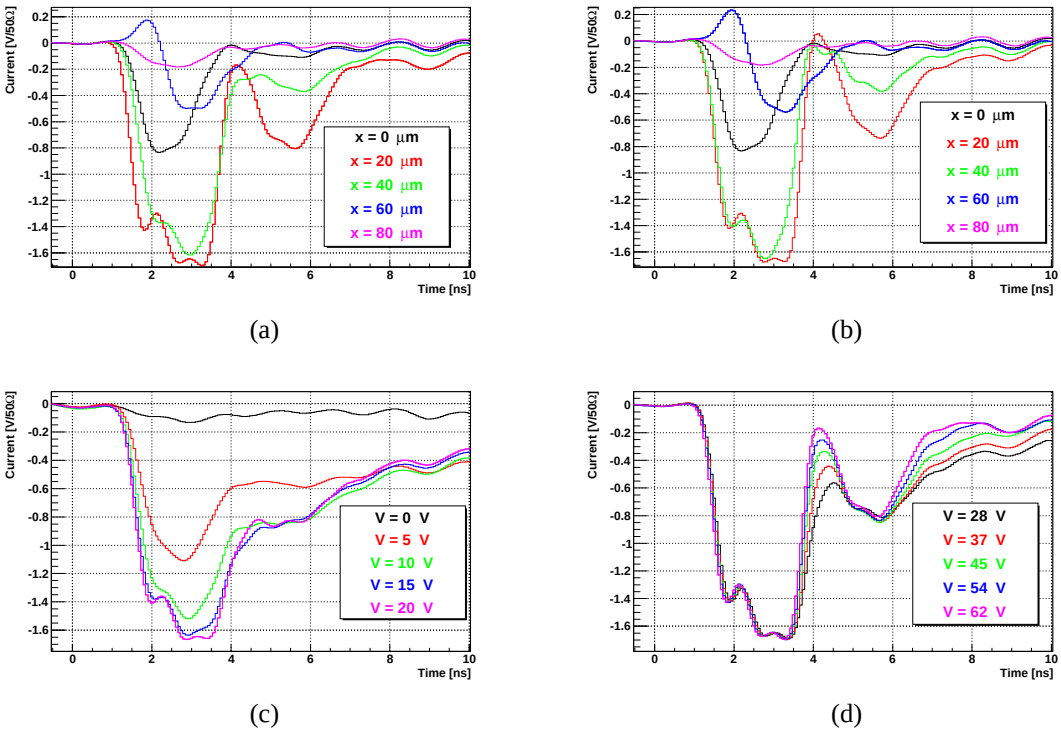

Figure 4.12: (a) and (b) show waveforms from various positions of illumination over the top surface of a non-irradiated sensor with a bias voltage of 62 V. The position of illumination given by the line (a) in Figure 4.11(a) corresponds to the waveforms in Figure 4.12(a) and line (b) in Figure 4.11(a) corresponds to the waveforms in Figure 4.12(b). (c) and (d) show the effect of varying the bias voltage on waveforms at a position of illumination 20 μm from the central strip on line (b).

Figures 4.12(c) and 4.12(d) show the waveforms produced with increasing bias voltage for the illumination point of x = 20 μm along line (b) of Figure 4.11(a). The waveform generated with a bias voltage of 5 V shows only an increasing current signal with time. This is due to the fact that the signal is dominated by electron movement towards the junction column because, while the device is fully depleted laterally, the magnitude of the electric field close to the ohmic columns is low and the signal from the holes drifting into this region is small. As the bias voltage increases the magnitude of the electric field inside the device increases and the waveforms exhibit distinct peaks, forming at approximately 15 V, due to the increase in the contribution of the hole signal; due to increasing hole velocity in the device in the region around the ohmic contact.

The rise time and magnitude of the prompt signal saturates at about 20 V. The rise time is dominated by the movement of the electrons in the high field region around the junction

electrode, and this saturates as the velocity of the electrons in this region of the device saturates. The fall time of this peak continues to become faster with increasing bias voltage, as this is dominated by the collection of holes in the device moving in the region around the ohmic contact where the electric field is lower than around the junction contact. The second displaced peak becomes separated from the first prompt peak with increasing bias voltage, due to a faster rise time and the fast fall time of the prompt peak. The second peak also has a faster fall time with bias voltage. However, the position of the peak of the signal does not change.

Using the same method as before, the velocity profile for the surface can be extracted and is presented in Figure 4.13. At the aluminium strip (overlaid in the figure) there is a small signal as a result of the non point source illumination. At 4 V, there is a significant velocity across the high electric field region, as expected from the lateral depletion voltage of 3 V. The combined electron and hole velocity is greatest in the 10 μm adjacent to the columns implying high electric field regions exist around the columns. The velocity then decreases in the region between the columns, because while there is full lateral depletion at 3 V there is still significant non-uniformity within the field of the device. As the voltage is increased, the velocity in all regions increases until saturation is reached by 80 V.

Summing the charge generated between the columns produces the same response as a MIP traversing the full strip. To do this, the waveforms from 0 μm to 40 μm in Figure 4.12(b) were integrated over 20 ns and then added together. This shows the total collected charge saturating at around 11 V and is displayed in Figure 4.14. This is due to a combination of the depletion of the inter-column region at 3 V and the under-column region requiring a higher voltage. The “MIP” in this example does not pass directly under the column, so full depletion in that region is not needed to collect all the charge.

The charge collection maps, presented in Figure 4.15, show the integrated charge collected in the 20 ns after the pulse. At 0 V, charge is only collected around the n-type columns and in areas directly between the n and p-type columns where the electric field is non-zero because of the built-in potential. There is little charge collected between columns of the same

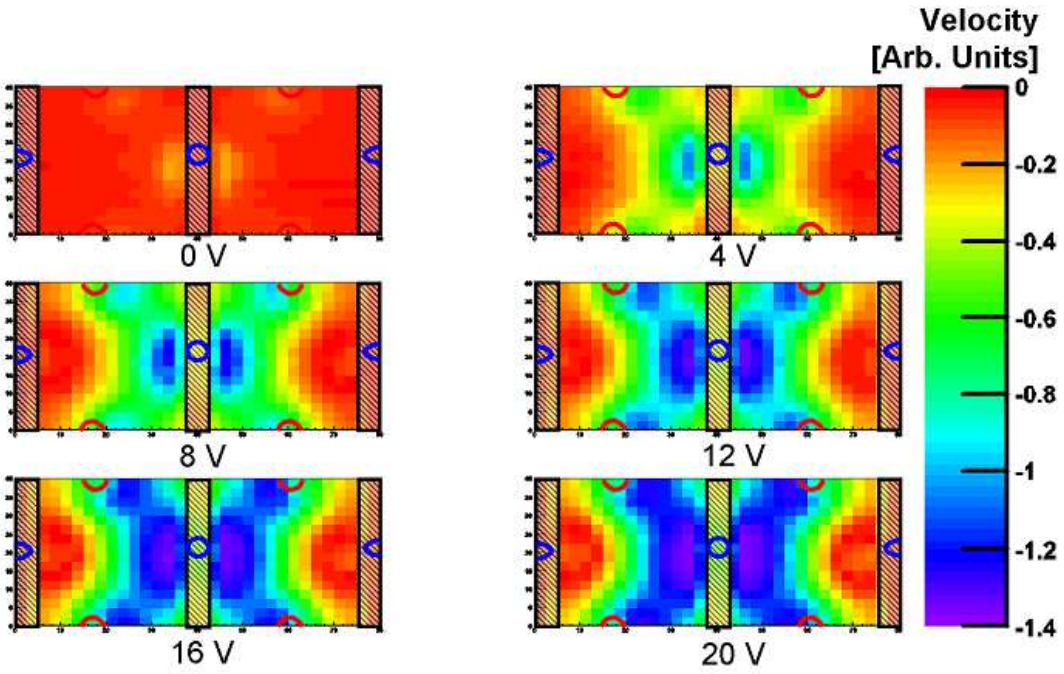

(a)

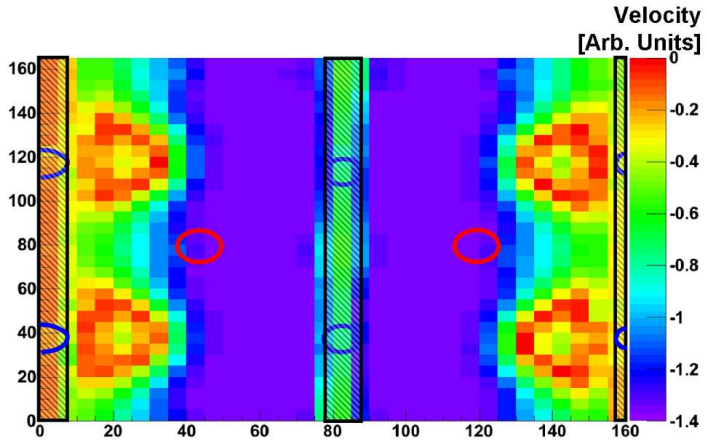

(b)

Figure 4.13: Velocity maps of a non-irradiated sensor with various bias voltages. (a) shows the velocity for bias voltages increasing from 0 V to 20 V and (b) shows the velocity with a bias voltage of 80 V. Positions of n-type columns (blue circles), p-type columns (red circles) have been indicated. The hatched areas are the positions of the aluminium strips forming the readout lines.

type because of the low electric field. As the voltage is increased, firstly the region around the n-type column shows full charge collection with the difference between the area around the n-type column and the rest of the active area disappearing as the voltage is increased to 15 V. Even at 15 V, the charge collection increases towards the collecting columns.

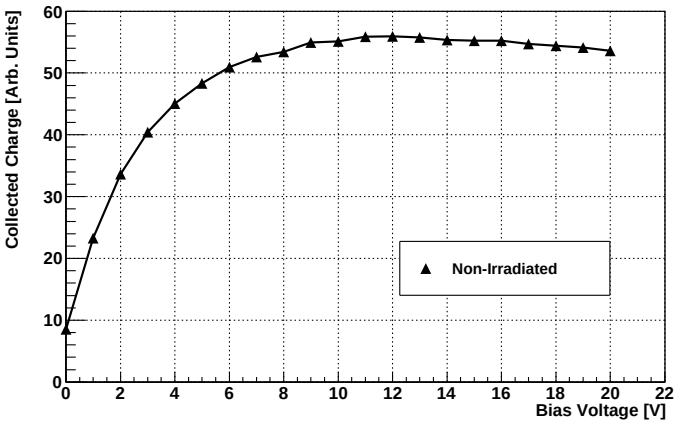

Figure 4.14: Charge collected versus bias voltage for a MIP-like particle.

The area around the p-type column show a low level of charge collection for biases up to 15 V. This is partially due to the column itself being non-collecting and also because the beam spot has a finite size. Although the centre of the beam may be outside of the column, part of the signal may be lost. There is still non-uniform charge collection in the low weighting field region between the adjacent p-type columns. The proportion of charge collected falls to 50% at the boundary of the unit cell. Any charge deposited at this location has a chance of being shared with and collected by the neighbouring cell.

4.3.4 Surface TCTs for Irradiated Sensors

A sensor was irradiated to 5 x 10^{15} 1 MeV equivalent neutrons/cm^2 at the Jozef Stefan Institute in Ljubljana. The irradiated device was kept at -20 °C to stabilise the leakage current and prevent unintentional annealing. During the initial mounting, the detector was at a slight angle to the orthogonal. This was corrected in later scans. As before, waveforms were collected for the same region across the surface and are shown in Figures 4.16 and 4.17. At 100 V there is very little difference between the waveforms generated perpendicular to the strip and those at 45°. The signal is much faster than for the non-irradiated case. This is due to the fact that the bias voltage applied is higher and the electric field is consequently greater. The trapping effects inside the device also reduce the duration of the signal. The signal at 100 V shows no obvious structure which implies that the contribution from the holes is

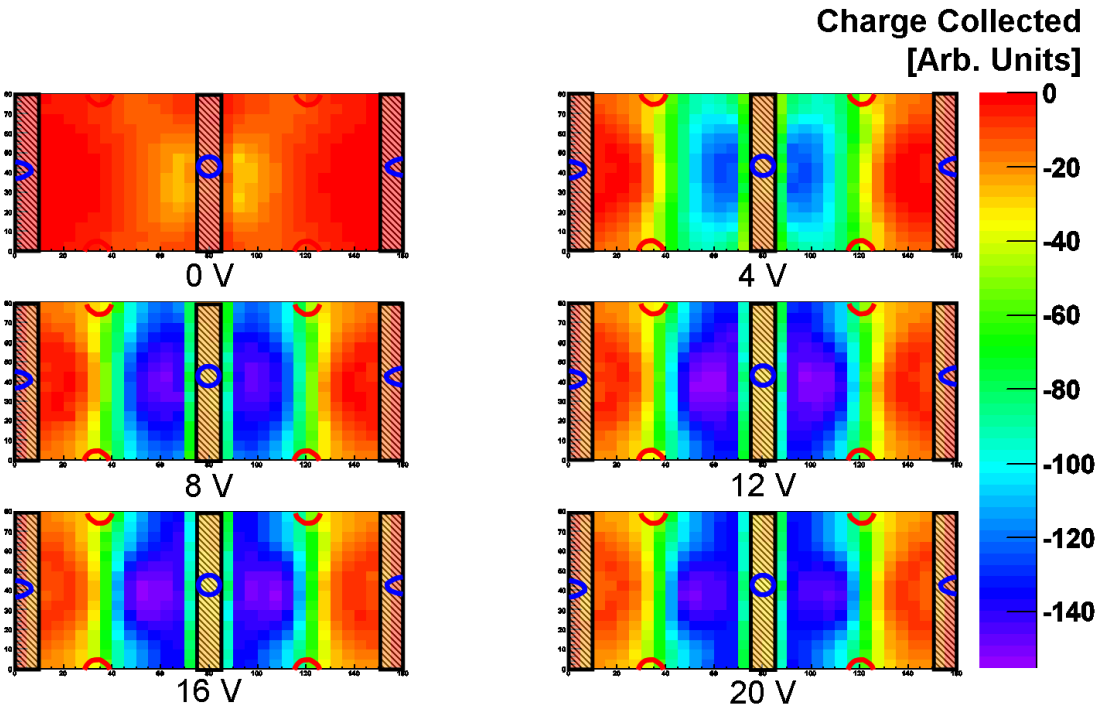

Figure 4.15: Charge collection maps with top illumination for a non-irradiated sensor. Bias voltage increases from 0 V (top left) to 15 V (bottom right) in steps of 3 V. Positions of n-type columns (blue circles), p-type columns (red circles) and strips (hatched area) have been indicated.

small. The magnitude of the signals generated along the line between the junction and ohmic columns, shown in Figure 4.17(b), falls uniformly with distance from the junction column as the electric field magnitude falls with distance from the junction column, even though the device has a bias of 100 V applied. The small signal at x = 0 μm is due to some of the signal being reflected by the metal strip.

With a higher bias voltage of 300 V the signal magnitude remains constant throughout the device (again the low signal at x = 0 μm is due to reflections at the strip and at x = 40 μm is due the laser falling on the non-sensitive hole). Therefore the device is fully active at this bias voltage. A second bump in the signal is now visible, but not a third, as in the non-irradiated case for illumination close to the ohmic contact. This would tend to suggest that the signal is still dominated by electrons even at these high bias voltages.

Velocity maps from this sensor were extracted with the same method as before and are presented in Figure 4.18. As with the non-irradiated sample, the velocity of the charge carriers are greatest when the pulse is adjacent to the n-type columns. Unlike the non-irradiated

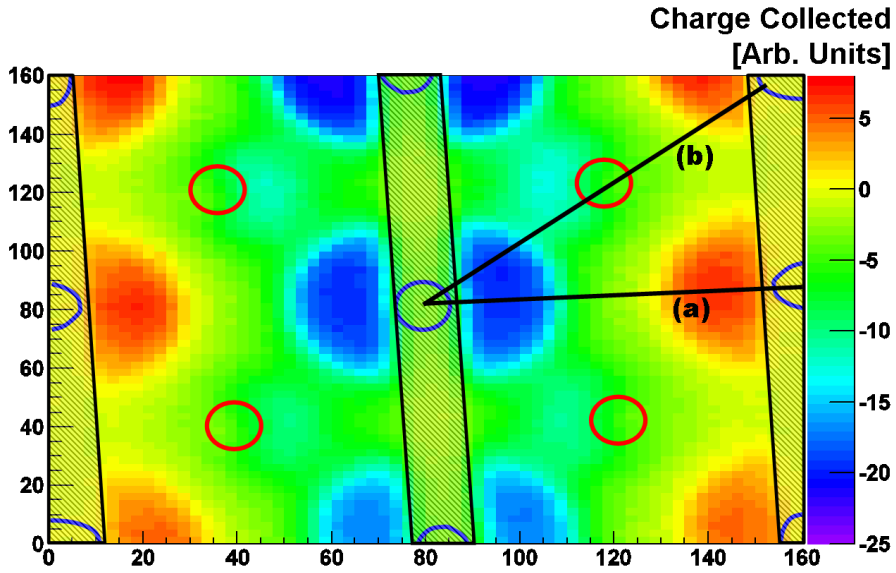

Figure 4.16: Charge collection map for the irradiated device with top surface illumination. Bias voltage was set to 70 V. Lines (a) and (b) correspond to the waveforms in Figures 4.17 (a) and (b). Positions of n-type columns (blue), p-type columns (red) and strips (hatched area) have been indicated.

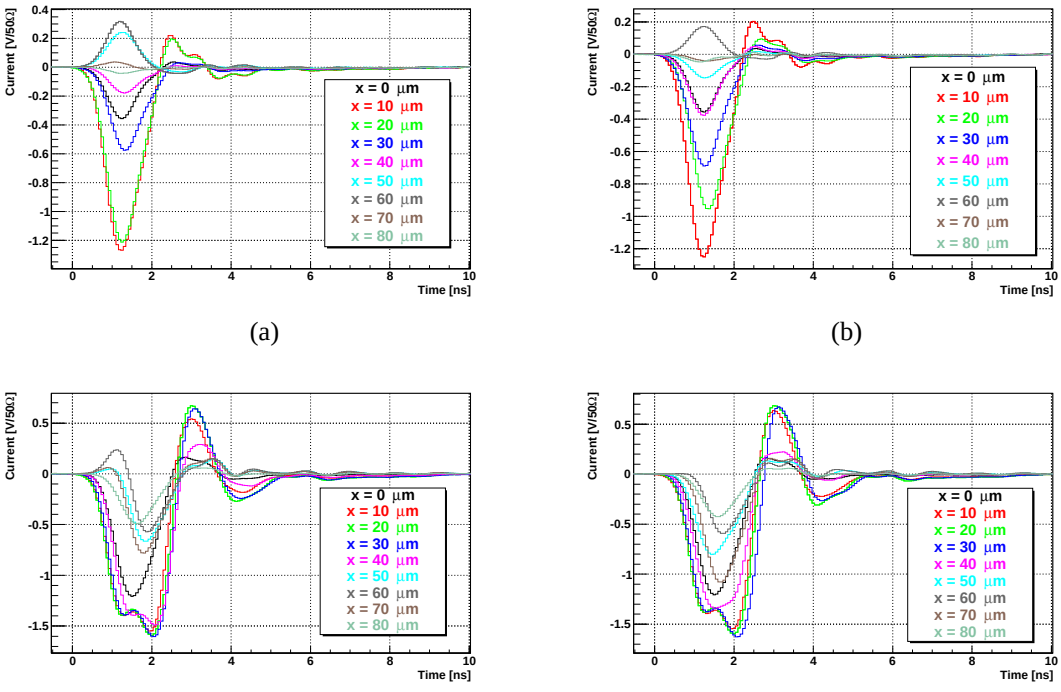

Figure 4.17: Waveforms from various positions of illumination over the top surface of an irradiated sensor moving from the central backside column to an adjacent one either perpendicularly in (a) and (c), or at 45° in (b) and (d). Bias voltages shown were 100 V in (a) and (b) or 300 V in (c) and (d).

sensor however, the combined velocity is greatly suppressed around the hole collecting, p-type column, for bias voltage up to 80 V. This experiment was not sensitive to the presence or not of the double field structure that would be expected for an irradiated device [92]. The device is fully active at a low bias voltage (40 V) but due to the low velocity at this bias point trapping will degrade the collected charge significantly.

The velocity throughout the device tends to increase with increasing bias voltage up to 200 V. At 200 V and greater biases, the velocity has a uniform profile across the device. This would only be the case if the velocity had become saturated at these high bias values.

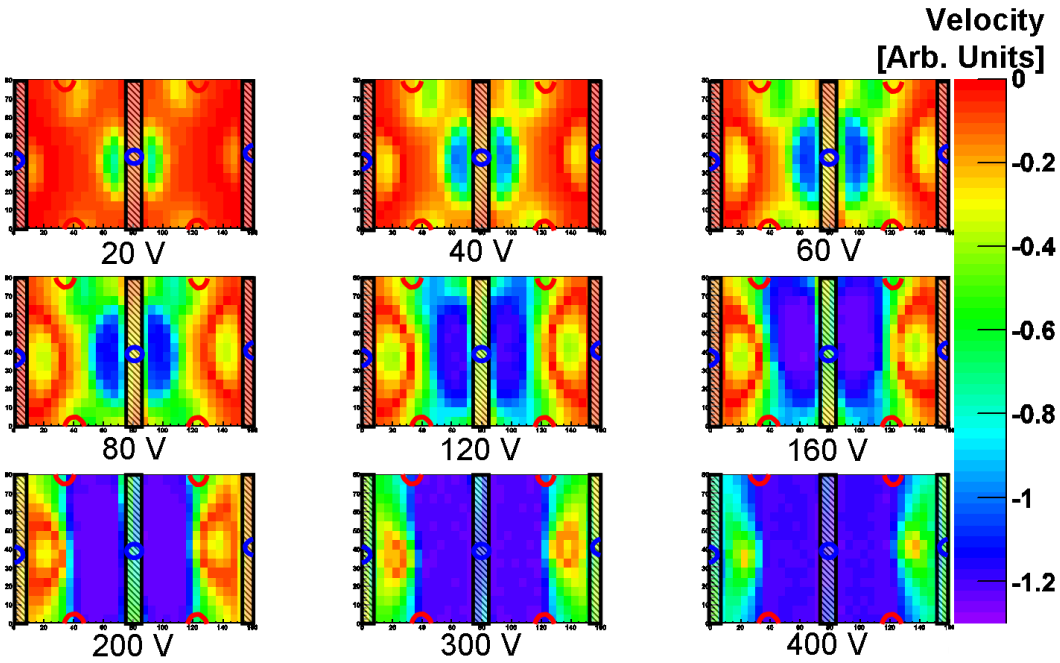

Figure 4.18: Velocity maps of an irradiated sensor with various bias voltages. Bias voltage increases from 20 V up to 400 V.

A similar effect can be seen when considering the collected charge in Figure 4.19. Below the full depletion voltage, the majority of the charge is collected in the high field regions around the columns where the velocity is greatest. At higher voltages, a greater proportion of the charge is collected from lower field regions. The opposite-sign signals around the columns away from the central strip are due to the full charge not being collected because of ballistic deficit. Charge multiplication effects become apparent in the high field regions above 200 V. At these bias voltages the velocity of the charge carriers is saturated. The

increase in the induced current recorded in Figures 4.17(c) and (d) can only be the result of charge multiplication. Additional acceptors appearing during long term annealing enhance the field and the multiplication then becomes more obvious.

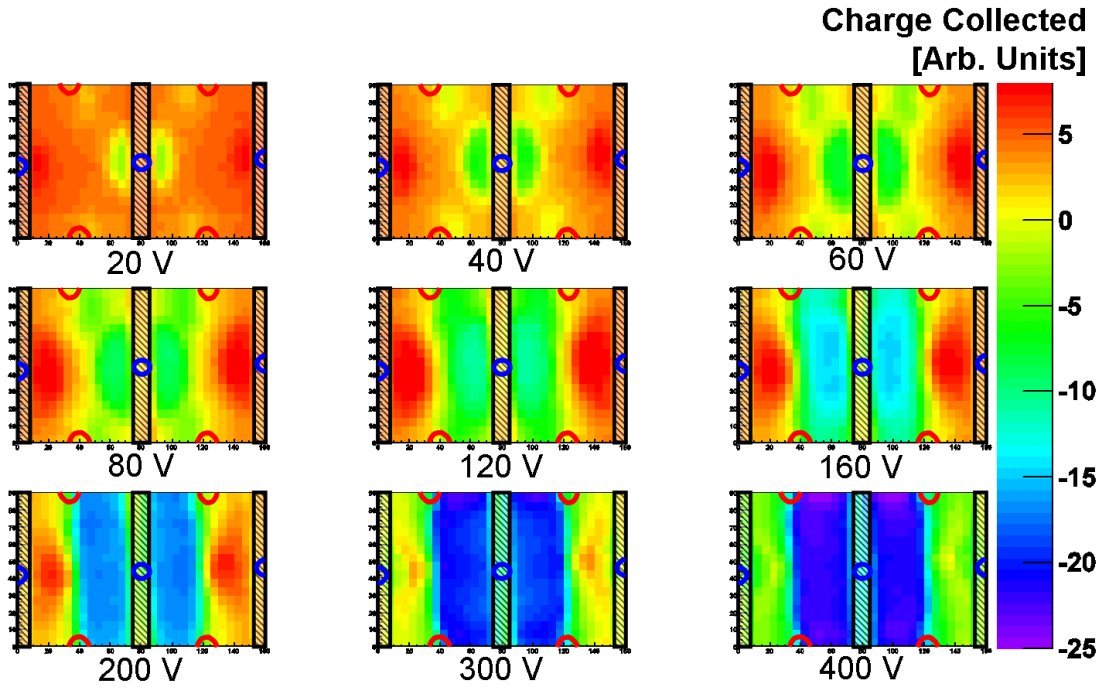

Figure 4.19: Charge collection maps with top illumination for an irradiated sensor. The bias voltages shown are 20 V, 40 V, 60 V, 80 V, 120 V, 160 V, 200 V, 300 V and 400 V. Positions of n-type columns (blue), p-type columns (red) and strips (hatched area) have been indicated.

4.3.5 Surface TCTs for Irradiated Sensors Post-Annealing

The effects of annealing the samples upon the signal collected were studied using the same techniques described in Section 4.3.3. The previously irradiated sample was annealed at 60 °C for cumulative times of 20 minutes, 40 minutes, 100 minutes, 300 minutes and 600 minutes. Annealing for 600 minutes at 60 °C (equivalent to the amount of annealing expected for 11 years of operation in an LHC experiment) led to the inter-strip resistance decreasing to a level where the strips were shorted together at bias voltages above 100 V. For this reason, only the annealing steps of 0, 20, 40, 100 and 300 minutes at 60 °C were considered.

Looking at the charge collected in Figure 4.20 and the waveforms generated after 20 minutes of annealing that are shown in Figure 4.21, a similar pattern to the pre-annealing

irradiated sample can be observed. The peaks and sub-peaks are very similar. For a bias voltage of 100 V the signal collected for illumination points closer to the ohmic contact (x = 30 μm) are now very similar to those collected for illumination close to the junction contact. This implies that the device has a high electric field throughout. At 400 V bias the waveforms are very similar to those before annealing.

The waveforms produced after 300 minutes of annealing are shown in Figure 4.22. These show the same series of effects as in Figure 4.21 after 20 minutes of annealing.

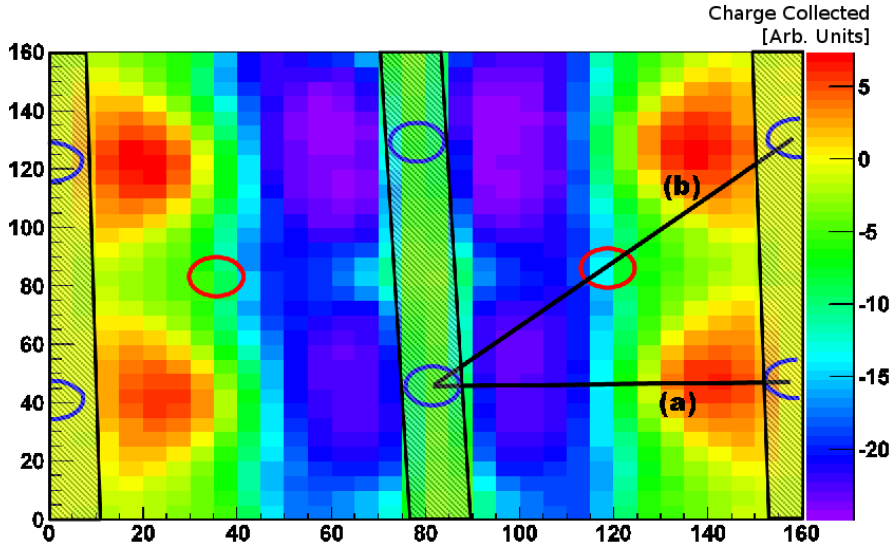

Figure 4.20: Charge collection map for the irradiated device after annealing for 20 minutes at 60 °C with top surface illumination. The bias voltage was set to 100 V. Lines (a) and (b) correspond to the waveforms in Figures 4.21(a) and (b). Positions of n-type columns (blue), p-type columns (red) and strips (hatched area) have been indicated.

Similarly to the non-irradiated device, it is possible to sum the charge generated between the columns as if a MIP traversed the region. This is presented in Figure 4.23. Above 300 V, the charge collected increases due to charge multiplication effects. This charge multiplication effect increases with longer annealing.

The charge collection maps for a unit cell of the device with a bias voltage of 400 V, as shown in Figure 4.24 were examined. After 20 minutes of annealing at 60 °C, the area with the greatest charge collection is the high field regions directly between the n-type and p-type columns. Longer periods of annealing cause the charge collection across the entire active area of the strip to increase proportionally. The waveforms shown previously in Figures 4.21

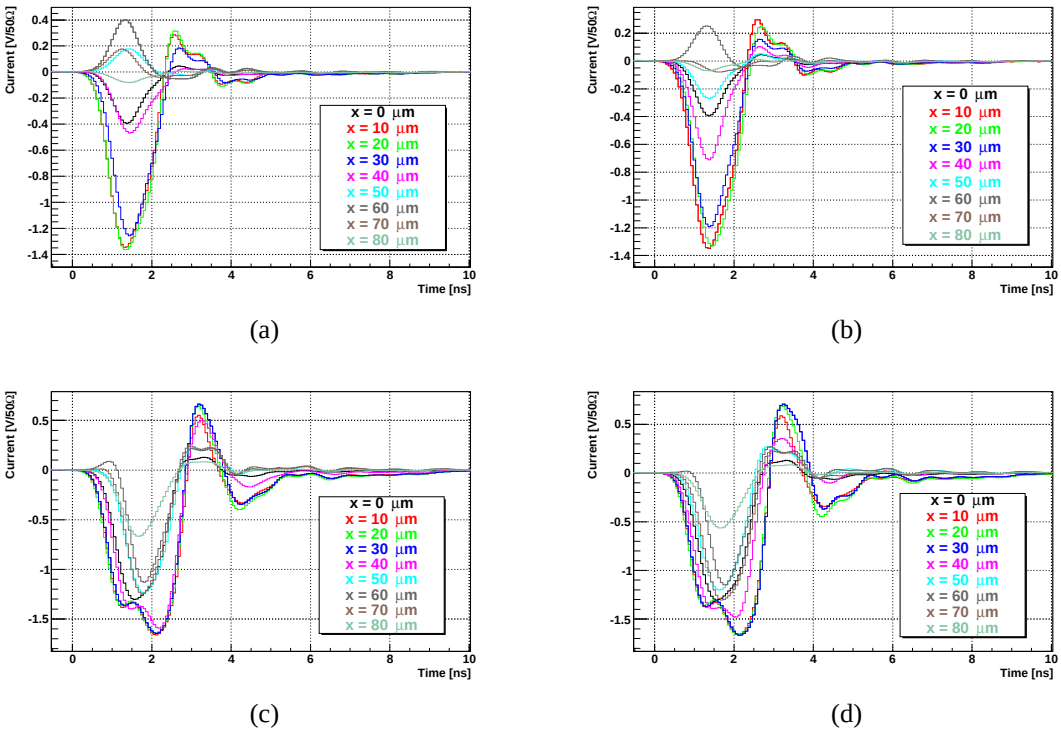

Figure 4.21: Waveforms from various positions of illumination over the top surface of an irradiated sensor, after annealing for 20 minutes at 60 °C, moving from the central backside column to an adjacent one either perpendicularly (a) or at 45° (b) with a bias voltage of 100 V or perpendicularly (c) or at 45° (d) with a bias voltage of 400 V.

and 4.22 show the complete signal is collected well within the 20 ns time frame required. Therefore, increasing the collected charge with longer annealing times is not due to the decrease in collection time. Effects of less trapping due to higher carrier velocities and shorter collection times are also not expected to be the cause of the increased charge as the drift velocity has saturated. Therefore the increase in charge collected is attributed to an increase in charge carriers due to a charge multiplication effect.

The electrons in the high electric field directly between n and p-type columns increase their kinetic energy enough to produce further electron-hole pairs. This creates a second, slower current peak. An electric field greater than 10 V/μm is required for electrons to undergo charge multiplication [93]. Due to their electrode structure, 3D devices have larger electric fields than a planar device of equivalent thickness and thus have greater potential for charge multiplication. Holes require a larger electric field to undergo multiplication. Charge multiplication has been observed with charge readout experiments in irradiated 3D devices

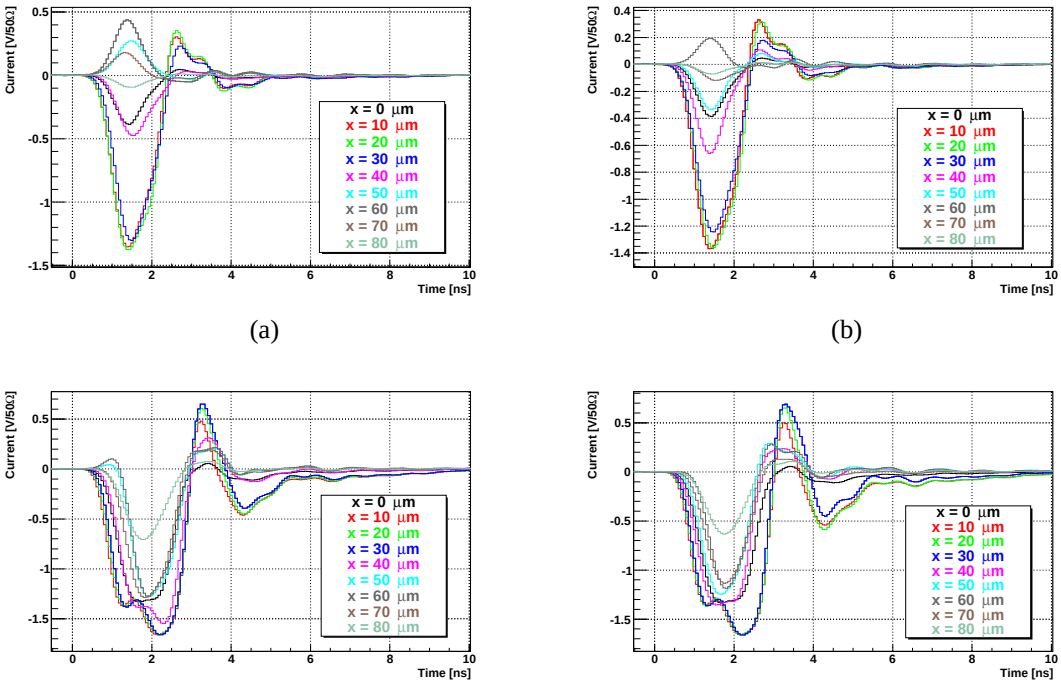

Figure 4.22: Waveforms from various positions of illumination over the top surface of an irradiated sensor, after annealing for 300 minutes at 60 °C, moving from the central backside column to an adjacent one either perpendicularly (a) or at 45° (b) with a bias voltage of 100 V or perpendicularly (c) or at 45° (d) with a bias voltage of 400 V.

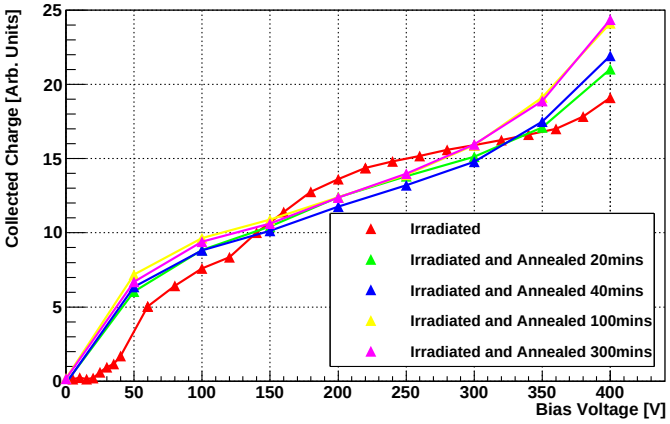

Figure 4.23: Charge collected versus bias voltage for a MIP-like particle for sensors that were annealed for a range of times.

[68].

The velocity map of the device, when biased to 400 V, is shown in Figure 4.25 for the different annealing stages. This shows that there is no change in the uniformity and magnitude of the velocity with increasing annealing unlike for the charge collection profiles.

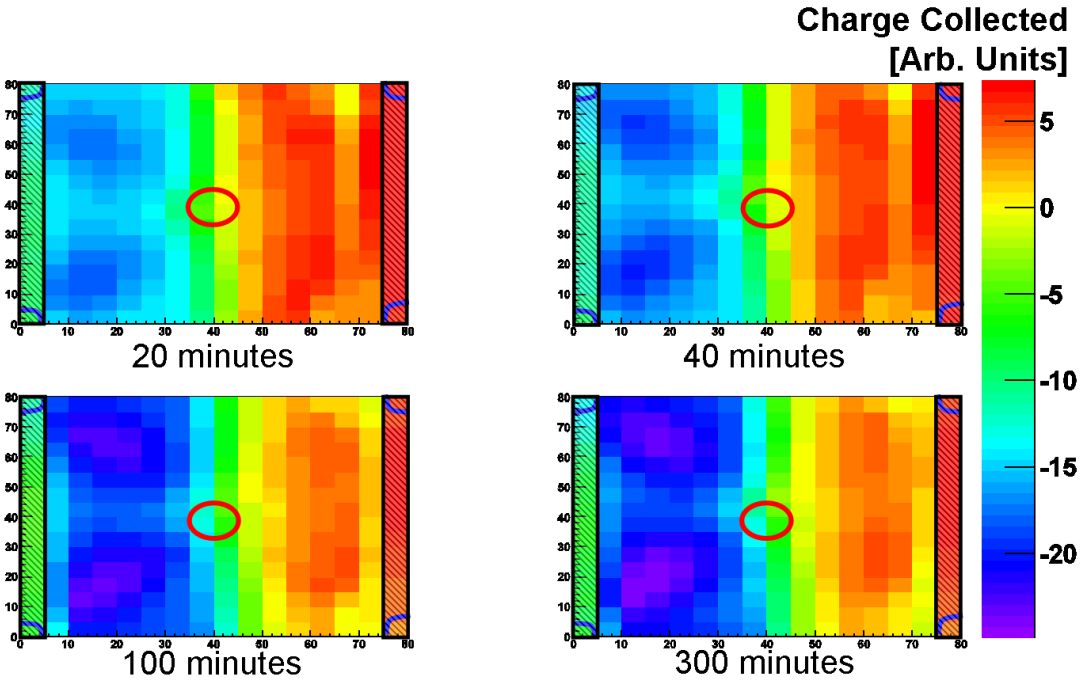

Figure 4.24: Charge collection maps for a sensor with a bias voltage of 400 V annealed for 20 minutes, 40 minutes, 100 minutes and 300 minutes. Positions of n-type columns (blue), p-type columns (red) and strips (hatched area) have been indicated.

The velocities of charge carriers of the non-irradiated device, the irradiated device and the irradiated device after annealing were compared in Figure 4.26. For the non-irradiated device, 80 V is a high enough bias to saturate the velocity across the active region. Post-irradiation results in this velocity are not saturating due to distortion of the electric field because of deep defects, even at a slightly greater bias voltage. However, even a short period of annealing provides a beneficial effect and increases the velocity closer to that of the non-irradiated device. With 400 V bias for the irradiated and annealed devices, it can be seen that the velocity of both the irradiated and annealed detectors approaches that of the non-irradiated detector. After irradiation there is an increased velocity beyond 40 μm. This is due to the opposite-signed signal produced in that area.

4.4 Conclusions

TCT measurements allow for the velocity of charge carriers within a device to be measured which a standard integrated charge collection technique does not. This enables the magnitude

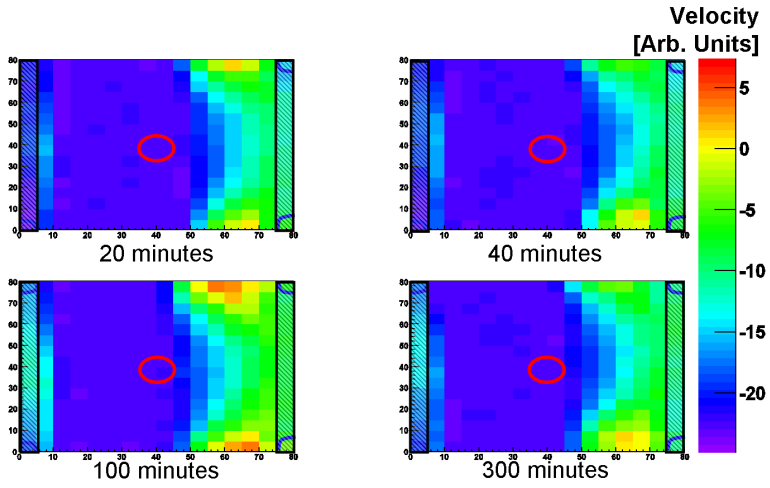

Figure 4.25: Velocity maps for a sensor with a bias voltage of 400 V annealed for 20 minutes, 40 minutes, 100 minutes and 300 minutes. Positions of n-type columns (blue), p-type columns (red) and strips (hatched area) have been indicated.

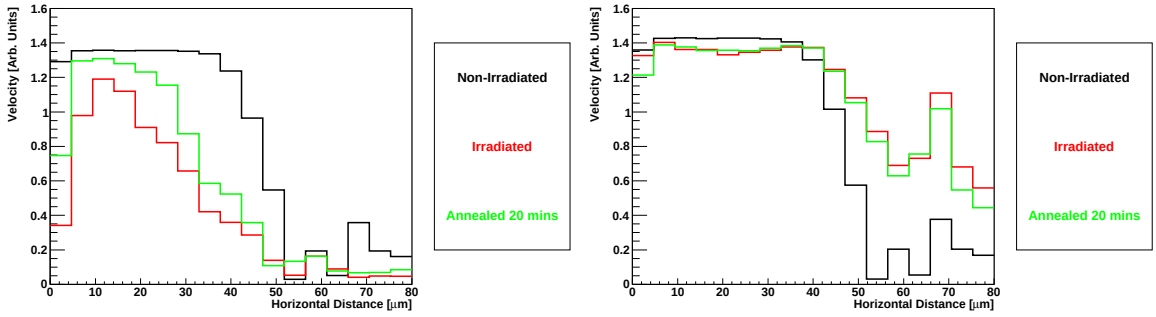

(a) (b)

Figure 4.26: Velocity profiles for various illumination positions, moving at 45° to the strip, for a non-irradiated sensor, an irradiated sensor and an irradiated sensor after annealing for 20 minutes at 60 °C. The non-irradiated sensor was biased to 80 V, and the irradiated and annealed devices were biased to 100 V in (a) and 400 V in (b).

of the electric field to be mapped in a way not possible before. This is because the collected charge saturates at full charge collection whilst the velocity continues to increase with bias voltage.

There is a clear non-uniformity of the sensors prior to irradiation. The areas of greatest carrier velocity and charge collection match the simulated electric field. While full lateral depletion between the columns occurs at low bias voltages, at approximately 3 V, a uniform carrier velocity between the columns is not achieved until 5 times this value at 20 V. Below 20 V, the greatest velocities of the charge carriers are adjacent to the columns. Both the drift of electrons and holes provide equal contributions to the measured signals. The regions

beneath the columns deplete at different rates depending on the type of column. The region underneath the n-type column depletes with a lower bias voltage than the p-type column.

The p-type and n-type columns were measured to be 7.30$\pm$0.03 μm and 9.18$\pm$0.03 μm respectively.

When illuminating the top surface prior to irradiation, a bias voltage of 80 V was required to create a uniform velocity of charge carriers across the device. Lower bias voltages again showed the highest velocities at the columns. The charge collection, however, was saturated at a bias voltage of 8 V.

After irradiation, both the velocity and the collected charge saturated at a bias voltage of 200 V. In addition, charge trapping greatly suppresses the contribution of the holes on the signal produced. This effect is most pronounced around the p-type column. There was no evidence observed of a double-junction around the p-type column. After irradiation there is clear charge multiplication enhancement along the line between columns with a very non-uniform velocity profile in the unit cell of the device at a low bias voltage (100 V). At 400 V the velocity profile appears more uniformly. This occurs at bias voltages in excess of the full depletion voltage of the device. The annealing of the detector further enhances these trapping and charge multiplication effects.

Chapter 5

Active Pixel Sensors

In this chapter, a novel CMOS APS detector is compared to a CCD in a typical synchrotron experiment [94]. The APS detector studied was the Vanilla device developed by the MI^3 collaboration (Multidimensional Integrated Intelligent Imaging) [14] and the Rutherford Appleton Laboratory (RAL). The CCD this was compared to was developed by Princeton Instruments and is used by the Diamond Light Source synchrotron in their experiments. Soft X-rays from the synchrotron were used to create a diffraction pattern from a permalloy sample that was then recorded with both the APS and the CCD. The noise and signal intensity of the two detectors were then compared.

The best figure of merit for an X-ray imaging application would be the detective quantum efficiency (DQE). To do this, a wide illumination with soft X-rays to create a flat field and to illuminate an edge mask would be required. This was not possible with our experimental setup, so looking at the ratio of spot intensity integrated over a ROI divided by the noise calculated over a background ROI at various exposure times gives an estimation of the detector performance that can be compared between the two detectors.

The Diamond Light Source synchrotron provides a wide range of beamlines, each with different photon wavelengths. The beamline used for the work in this chapter was the Nanoscience beamline, I06. The energy range of the photons available is from 80 eV to 2100 eV (corresponding to wavelengths of 15.5 nm to 0.6 nm). By illuminating a sample with X-rays, deflections from the atoms can be recorded. Analysis of the patterns produced

from the diffraction and scattering of photons can provide information on the structure of molecules. The spots produced from a diffraction pattern will decrease in intensity the further from the centre they are formed. Measuring the strain in materials when under load is also possible by monitoring the changing distances between various atomic planes. Scattering experiments are used to determine the structures of non-crystalline materials such as proteins.

X-rays can be segregated into hard and soft X-rays depending on their wavelengths. X-rays with wavelengths shorter than 0.2 nm are referred to as hard X-rays. These will penetrate further into materials before scattering than the soft X-rays with longer wavelengths. Tuning the wavelength is important in order to be able to produce a diffraction pattern from a specific crystal structure. The photon flux at the I06 beamline was 2.0 x 10^{12} photons/s. Consequently, a detector designed to image these diffraction patterns will require a large dynamic range in order to image the full range of intensities within the diffraction pattern. A small pixel size and high resolution will be necessary for clear imaging of the diffraction pattern. For dynamic experiments such as where the distances between atomic planes varies, a high frame rate will be required in order to measure the changes accurately.

5.1 An Introduction to Active Pixel Sensors

Charge Coupled Devices (CCDs) are currently used in the majority of high-end imaging applications due to their low noise and high sensitivity. Complementary Metal-Oxide Semiconductors (CMOS) sensors are an emerging technology that could be applied in situations requiring faster or real-time image acquisition [11]. These differing technologies were discussed in Sections 2.2.4 and 2.2.5. In this chapter, a novel CMOS APS detector will be characterised before comparing it to a Princeton CCD in a typical synchrotron experiment.

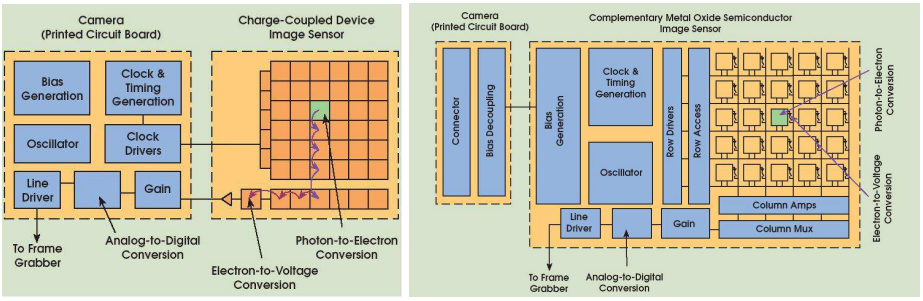

(a) (b)

Figure 5.1: Diagram of a generic CCD (a) and CMOS APS (b) layout. In a CCD, charge collected is passed down each column to be read out. The remainder of the printed circuit board can be customised based on the required specifications. In a CMOS APS, the charge collected in each pixel can be read out independently of its neighbours. [43]

5.1.1 Charge Coupled Devices

CCDs operate by accumulating signal charge in each pixel in proportion to the incident photon flux. When the preset acquisition time is completed, the charge is passed sequentially from each pixel down its column. When it reaches the output structure, the charge is converted to a voltage and read out. This is shown in Figure 5.1(a). Once it has been read out, the voltage is multiplied by the device's gain and converted to a digital signal.

CCDs are used in a wide variety of applications. However, CCDs can suffer from an effect known as blooming. This is when the charge collected within a single pixel exceeds its storage capacity, resulting in the charge spreading to the neighbouring pixels. This storage capacity is defined as the full-well capacity and is the maximum number of signal electrons that a pixel can store at once, which is fundamentally constrained by the size of the pixel. There are many advantages in using CCDs for imaging applications. Firstly, CCDs will typically have low noise performance especially concerning fixed pattern noise. This is because a CCD only has a conversion element and so has essentially no source of pixel to pixel variations. This is described in more detail in Section 5.1.2.1. Secondly, CCDs will normally operate over a large dynamic range. The conversion from incident photons to electrons will not be completely linear across the entire dynamic range. The percentage deviation from the linear response is defined as the linearity of the sensor.

However, there are several reasons why technologies other than CCDs should be investi-

gated. CMOS-based sensors typically have lower power requirements and can be manufactured in bulk relatively inexpensively. CMOS sensors can also integrate on-chip processing for intelligent imaging applications.

The CCD used in our experiment was a Princeton PIXIS-XO: 2048B with 2048 by 2048 pixels and this is representative of the CCDs currently in use at the Diamond Light Source. A photograph of this CCD is shown in Figure 5.2(a). Each pixel is 13.5 μm by 13.5 μm in size. The CCD had both low noise and high capacity modes, and could be operated at different gains and speeds. During our experiment, the CCD was operated at a speed of 2 MHz. At this speed, the low noise mode had a specified rms noise value of 17.3 e^-, a gain of 1.0 e^-/ADU and a non-linearity of less than 2%. The high capacity mode had a specified rms noise value of 36.6 e^-, a gain of 3.5 e^-/ADU and a non-linearity of less than 2%. The single pixel full-well capacity of both modes was quoted as 100 ke^- and the dark current was given as 0.008 e^-/pixel/second. All of this data was for operation at -60 °C, which was the temperature at which the experiment was performed. These values were taken from the manufacturer's datasheet [95].

5.1.2 Vanilla Active Pixel Sensor

CMOS Active Pixel Sensor (APS) devices mainly differ from CCDs as they perform the charge to voltage conversion on each individual pixel. This is shown in Figure 5.1(b), and a photograph of this is shown in Figure 5.2(b). As discussed in Section 2.2.5, CMOS detectors include a minimum of three transistors within each pixel. The three transistors perform the functions of row selection, signal to voltage conversion and then the pixel reset. Additional transistors can be included to provide optional features such as active buffering, additional amplification or in-pixel processing or discrimination if desired. Random access to pixels allows the development of intelligent imaging.

A new series of APS, the Vanilla APS, was developed by the MI^3 collaboration [14] of which the University of Glasgow was a part. It was designed as a general purpose sensor, with design specifications of 100 frames per second (fps) full-frame readout, and a readout

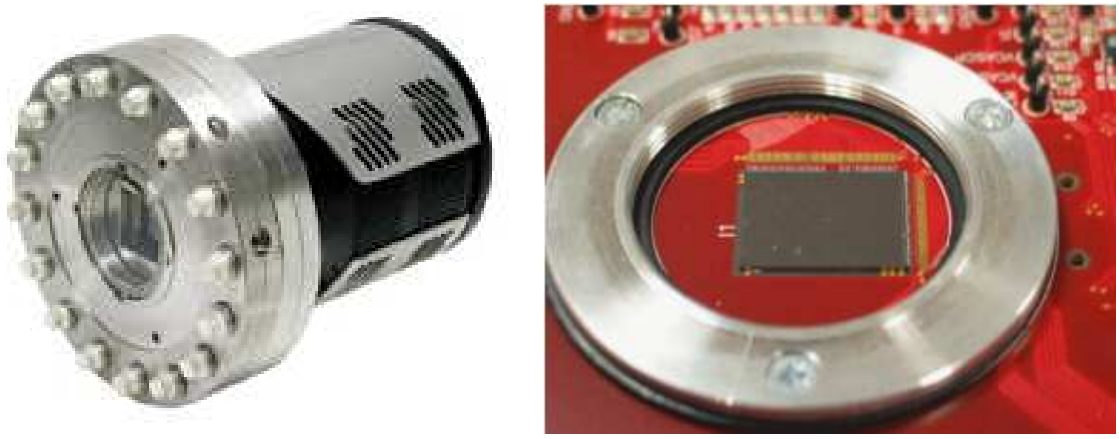

(a) (b)

Figure 5.2: Photographs of the CCD (a) and CMOS APS (b) used in the experiment

noise of below 25 electrons RMS. The sensor had 520 by 520 25 μm pixels.

Signals were able to be read out in either analogue or digital formats. The analogue mode utilised an off-chip analogue to digital converter (ADC) approach and was designed specifically for region of interest (ROI) measurements using a 10-bit readout system. In order for this to be facilitated, address decoders replace the column shift registers. The readout time of any single pixel is limited by the capacitance load of the wires and the DAQ system. Hence, reducing the number of pixels to be read out will give a higher frame rate. The default digital readout mode uses an on-chip ADC approach and is faster for full-frame readout, employing a 12-bit on-chip ADC. The sensor was also designed with the possibility of back-thinning, ceramic packing in vacuum operation and two side tiling.

The Vanilla APS has the standard 3 transistors per pixel that was discussed in Section 2.2.5. However, additional circuitry was used in order to implement different reset modes. A schematic of this is shown in Figure 5.3. The transistor labeled Mrst is used to reset the pixel, Msf is used to convert the collected charge to a voltage and Msel is used to select the row to be read out. The remaining components are used to implement the hard, soft and flushed resets [51].

There were three reset modes available to the Vanilla APS - soft, hard and flushed [11]. Using the soft reset, the gate and drain of the reset transistor (labeled Mrst in Figure 5.3) are set to the same fixed voltage. This leads to residual charge remaining on the photodiode from

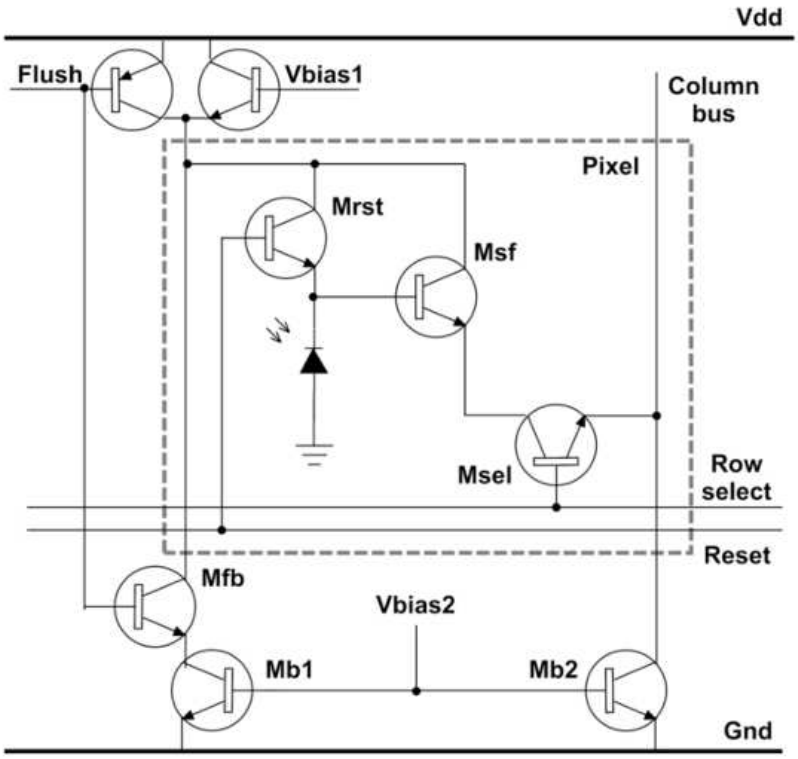

Figure 5.3: Vanilla APS pixel circuitry with column-based reset architecture.

previous integration periods. This effect is known as image lag and is examined in Section 5.3.1.4. This effect is greatest where the charge on a pixel may vary greatly from frame to frame. The advantage of this reset mode is that the smaller reset voltage reduces the noise but at a cost of increasing the image lag.

When a hard reset is applied, the gate voltage of the reset transistor is set higher than the drain voltage by more than the transistor voltage. This applies a voltage to the photodiode that clears it of any residual charge preventing any image lag. However, the reset noise in this mode will typically be greater by a factor of $\sqrt{2}$.

The flushed reset mode was designed with the idea to implement the image lag prevention of the hard reset mode with the reset noise of the soft reset mode. In this mode, a short hard reset is performed followed by a soft reset.

Back-thinning is a well established process in high-specification scientific applications involving CCDs. During this process, the substrate is thinned using a combination of lapping, mechanical grinding, chemical etching and laser annealing. This reduces losses in the bulk

silicon on the back of the device. Consequently, the quantum efficiency of a detector can be improved across the full spectral range if the device is illuminated from the back and thinned. A typical device, with passivation, electronics and metal to a depth greater than a micrometer on the surface, will prevent nearly all of the photons with a wavelength below 400 nm being detected. More recently, there has been a move towards the back-thinning and illumination in CMOS devices as well [96].

One reason for back-thinning is to increase the fill-factor of the sensor. The fill-factor is the percentage of the surface area of a pixel that is sensitive to incoming photons and not reflected by metal traces on the front of the sensor. Although the fill-factor is dependent on the wavelength of light illuminating it, back-thinning can increase this fill-factor to essentially 100%. A second reason for back-thinning a sensor is that it reduces the mass.

The back-thinning of the Vanilla APS was performed by e2v[1]. The process involves removing the back substrate up to the epitaxial layer using a variety of methods including reactive ion etching and laser annealing. The thickness of substrate remaining above the epitaxial layer was between 14 μm and 20 μm. The sensor was then reversed and bonded to its PCB. The back-thinning and back-side illumination increased the measured signal by reducing the number of photons lost due to interactions with the device's circuitry. This particularly improved the signal collection for higher energy photons, particularly soft X-rays.

Regardless of whether the Vanilla APS was read out in Analogue or Digital mode, the initial stages of the process are the same. The ADC and all of the pixels are reset and the bias generators are set to their defined values. Then, the process diverges for digital and analogue readout modes. For digital readout, the rows that require reading out are selected by using a 10 bit value from the address decoders. Once the correct row has been identified, the column read lines will show data from each corresponding pixel. When the full-frame is being read out, the data can be digitised before being read out. This involves using a successive approximation ADC. The physical size of the ADC limits the number that can be implemented on each sensor. In the case of the Vanilla APS, each ADC multiplexes signals

[1] e2v, Chelmsford, UK.

from four columns. Once the pixel values are digitised, the digital value is stored in 12 bit RAM until the remainder of the four columns are converted. The data is then read out using shift register.

When the analogue readout mode is employed, the data from each pixel is read serially using two different analogue multiplexers. Each of these places the input in a buffer amplifier and then to the off-chip ADCs where the data is converted to the digital result.

5.1.2.1 Noise Sources in a Sensor

There are four main sources of noise in any measurement by a sensor. Two of these sources, Fano noise and photon shot noise, are related to photon interactions with a pixel. The third source, fixed pattern noise, is dependent on the pixel to pixel non-uniformity of a sensor. The final source of noise is read noise and this encompasses all sources of noise related to the readout of the signal and the reset of the pixel. Fano noise is proportional to the square root of the incident photon's energy, whilst shot noise is proportional to the square root of the signal and fixed pattern noise increases proportionally to the signal.

The photon shot noise is defined as the standard deviation of the number of photon interactions per pixel. This is related to the fact that photons incident on a detector will be randomly dispersed in space and time. This can be described by Bose-Einstein statistics as follows,

$$\sigma_S(P_I)^2 = P_I \frac{e^{E_p/kT}}{e^{E_p/kT} - 1}, \tag{5.1}$$

where $\sigma_S(P_I)^2$ is the variance due to shot noise as a function of photon intensity, P_I, k is Boltzmann's constant, T is the temperature of the detector and E_p is the energy of the photons.

Photons with an energy greater than 0.1 eV will begin to couple with lattice vibrations and cause an increase in shot noise. Increasing the temperature of the detector will cause larger lattice vibrations and consequently will also increase the shot noise. However, for most imaging applications (e.g. at room temperature) hc/λ will be much greater than kT. In

these cases, Equation 5.1 will simplify to,

$$\sigma_S(P_I) = \sqrt{P_I}. \tag{5.2}$$

The photon shot noise can also be used to determine the probability, p_i, that photons will interact i times with any pixel,

$$p_i = \frac{P_I^i}{i!} e^{-P_I}. \tag{5.3}$$

Fano noise is defined as the variation in electron and hole pair production from photons of identical energy. If all of a photon's energy were to go into electron and hole production then there would be no Fano factor in the noise. However, some of a photons energy will be lost in interactions with the lattice. This can be derived empirically as,

$$\sigma_{FN} = \sqrt{F_F \eta_i} = \sqrt{F_F \frac{h\nu}{E_{e,h}}}, \tag{5.4}$$

where σ_{FN} is the variance due to Fano noise, F_F is the Fano factor, h_ν is the energy of the incident photon and $E_{e,h}$ is the energy required to create a single electron-hole pair. η_i is then simply $\frac{h\nu}{E_{e,h}}$. The Fano factor is defined as the variance in the number of electrons generated over the average number of electrons generated. This factor is given as 0.1 for silicon and begins to dominate from the soft X-ray region and higher energies. Low-noise detectors based on CCD or CMOS technologies will generally be limited by Fano noise in X-ray and gamma ray detection. When imaging photons with longer wavelengths, the Fano noise will typically be less relevant to the noise performance of the detector.

After photons interact with a detector, there will be a quantity of charge within a range of pixels. How efficient each pixel is at collecting charge will differ from pixel to pixel. This effect will be compounded with variations in the gain when this charge is converted to a current. The variation in the gain results from the variation in the transconductance of the transistors. This will create sensitivity differences across a detector. It is referred to as fixed pattern noise because the differences in sensitivity are constant from frame to frame. The

fixed pattern noise resulting from variations in the gain can be defined as,

$$\sigma_{FPN}^2 = P_N S, \tag{5.5}$$

where S is the signal and P_N is a quality factor. For a silicon sensor, this quality factor will typically be approximately 1% and is the ratio of noise to the mean signal. Due to its direct relationship with signal, fixed pattern noise will dominate shot noise over a large region of an imaging sensor's dynamic range. It is possible to remove the fixed pattern noise resulting from the pixel to pixel variations in the pedestal by subtracting one consecutive frame from the next, assuming the frames have identical levels of photon flux. This process is called flat field correction [97].

Read noise (σ_R) accounts for any other sources of noise present in a particular measurement that are not proportional to the photon intensity. An example of this would be the reset noise. The reset noise originates from thermal noise effects within the pixel architecture. This changes the reset reference voltage every time the pixel is reset. The level of reset noise will vary depending on the reset mode employed. When all of the sources of noise are combined in quadrature the total noise, σ_T is given as,

$$\begin{aligned} \sigma_T^2 &= \sigma_S^2 + \sigma_{FN}^2 + \sigma_{FPN}^2 + \sigma_R^2 \\ &= P_I + F_F \eta_i + (P_N S)^2 + \sigma_R^2. \end{aligned} \tag{5.6}$$

5.2 Characterising the Vanilla sensor at Low Temperatures

5.2.1 Photon Transfer Curve

In a sensor, the incoming signal is measured by the number of electrons it generates in the silicon substrate. This is then converted to Analogue-to-Digital Unit (ADU) for reading out. The ratio of electrons per ADU is given by the sensor's gain. One method for measuring this gain is the Photon Transfer Curve (PTC) [97]. To create a PTC, rms noise is plotted

as a function of mean signal with a monochromatic light source. The level of signal can be altered either by varying the intensity of the monochromatic light source or by varying the image integration time. This process can be completed for either the full array of pixels or a subset of them. When this data is plotted on a log-log scale four dominating regimes can be observed. An example of this is shown in Figure 5.4. This calculation can either give an average value across the entire sensor array or can be repeated for each pixel individually.

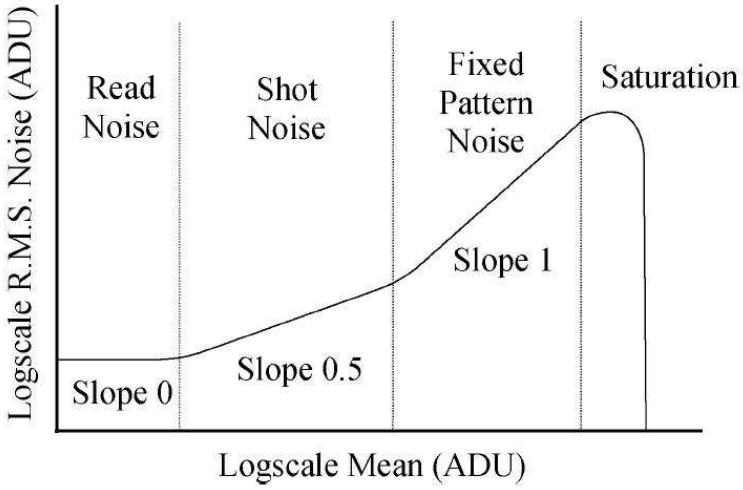

Figure 5.4: Example Photon Transfer Curve, showing the four main regimes identifiable. The fixed pattern noise includes the variations from the different gains between pixels. In addition, the full well capacity and gain can be calculated from the plot. [98]

Under dark or low-light conditions, the read noise of the sensor should dominate. This will often have multiple sources of noise. As the read noise is not related to the photon intensity, the logarithm of the read noise will not vary with increasing signal and will have a slope with a gradient of 0. As the signal increases, the photon shot noise begins to increase in importance. As shown in Equation 5.2, the shot noise is proportional to the square root of the signal. When the logarithm is then taken, this regime becomes identifiable by the slope with a gradient of 0.5. A further increase in the signal leads to the fixed pattern noise dominating and this increases proportionally with the signal, as shown in Equation 5.5. This results in the logarithm of the noise increasing as a function of the signal with a gradient of 1. Finally, the full-well regime is characterised by the noise decreasing as the pixels in the array saturates. This is because the shot noise will always decrease under saturated conditions, even if the

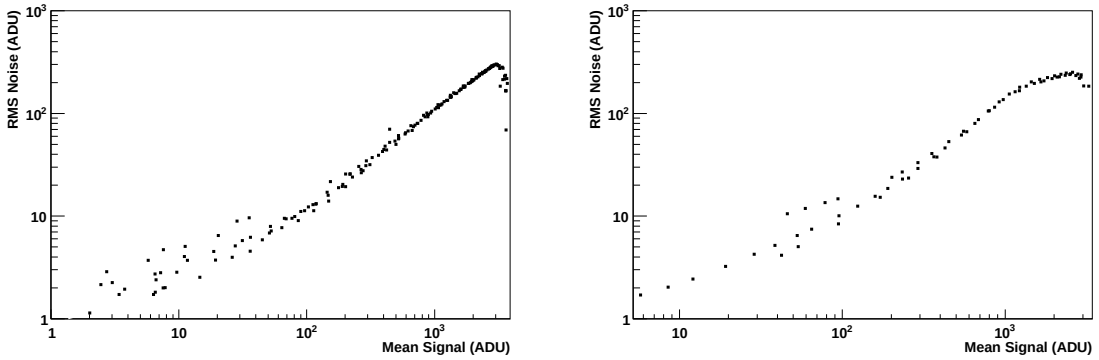

(a) (b)

Figure 5.5: PTC curve for the Vanilla sensor in digital (a) and analogue (b) modes, after pedestal subtraction.

fixed pattern noise may continue increasing. The reason the fixed pattern noise may carry on increasing is because some pixels and columns of pixels will reach saturation before others. This will introduce a further fixed pattern effect across the sensor.

When illuminating the array of pixels it is important that the light source used has as uniform an intensity as possible. Variations in the uniformity can act as additional fixed pattern noise. The wavelength of the light used may also have a small effect on the fixed pattern noise as well. The shot noise regime is immune to the effects of uniformity and wavelength.

Before the mean signal value can be calculated for any individual frame, the background noise has to be subtracted. This removes background electrons such as those generated by thermal dark current.

The PTC allows several key characteristics of the detector to be analysed [99]. The full-well capacity is given by the maximum signal prior to saturation. The dynamic range is the ratio of the noise under full-well conditions to the read noise. The camera gain is equal to the x-intercept of a linear fit to the shot noise region.

PTCs were generated using the Vanilla APS and averaged over the entire pixel array. A green LED, with a wavelength of 530 nm, was used to vary the signal intensity for a range of frame rates and temperatures. The PTCs are shown for both analogue and digital readout modes in Figure 5.5.

There are several ways to improve upon these curves. One method would be to remove the fixed pattern noise by subtracting two consecutive frames with identical illumination levels from each other. An alternative to this would be to calculate the gain for each individual pixel, and this is the method that was used. This has the advantage that pixel to pixel variations are now irrelevant, and any variations in gain across the sensor can be determined. The downside is the large increase in data that needs to be fitted to produce a valid measurement.

A map of the gains measured across the Vanilla APS in digital mode and the resulting histogram are shown in Figure 5.6. The mean of the gains across the sensor was measured as 7.87 ± 0.01 e^-/ADU with the mean of the gaussian portion at 8.69 ± 0.01 e^-/ADU. The map of the gains shows a cyclic pattern every fourth column. This is a result of the digital readout mode sharing one ADC for each set of four columns. There is also a pattern of diagonal striped regions of lower average gains. It is these areas of lower gain that make the expected gaussian distribution of the gains in Figure 5.6(b) to spread out the lower tail.

In addition to the gain, further information can be gathered from the photon transfer curves. The full-well capacity, read noise and dynamic range are presented in Table 5.1. These can also be observed from Figure 5.5(a). The full-well capacity is the signal level at which saturation is achieved and the read noise is the level where the read noise regime is entered. The dynamic range is then simply the ratio of the full-well capacity to the read noise.

Gain	7.87 ± 0.01 e^-/ADU
Full-Well Capacity	$25\,000\pm200$ e^-
Read Noise	15 ± 1.5 e^-
Dynamic Range	$\sim1700\pm140$

Table 5.1: Specifications of the digital readout mode of the Vanilla sensor derived from the PTC.

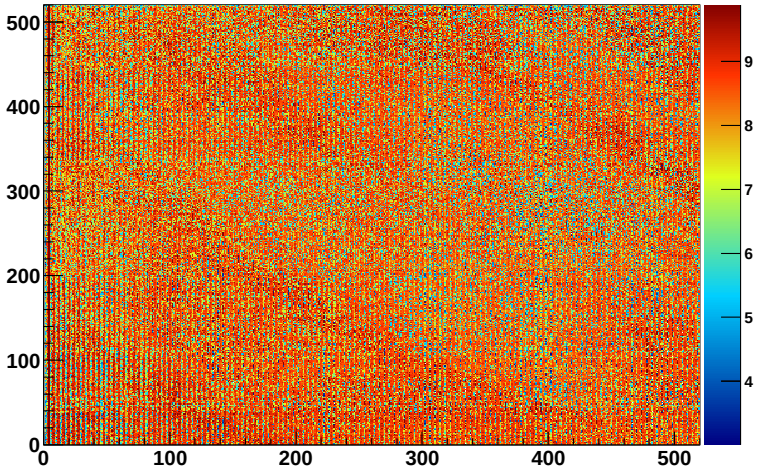

(a)

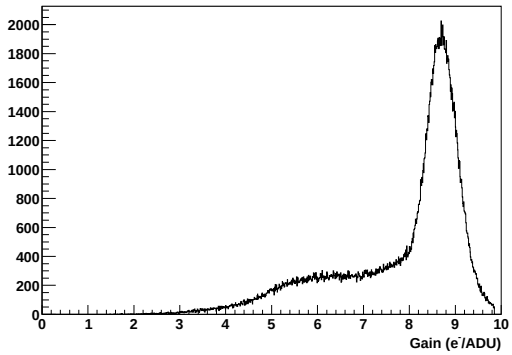

(b)

Figure 5.6: The gain was calculated from the shot noise region of the PTC from each individual pixel of the Vanilla Sensor, operating in digital mode. This was then plotted as a map of the pixels (a), and as a histogram (b). The mean gain across the sensor was calculated as 7.87 ± 0.01 e^-/ADU.

5.2.2 Stability with Temperature Changes

The performance of the Vanilla APS generally improves as the operating temperature is lowered. This is because the generation of electrons and holes as a result of thermal effects will be reduced. In order to determine whether cooling and warming the Vanilla APS over the course of a typical multi-day synchrotron experiment would effect the sensor, measurements of the stability and damage to pixels were made.

Initially, a Vanilla detector was placed in an oven and baked for a period of 10 days at 50 °C. The purpose of this was to ready the detector for vacuum experiments. The detector was then placed in a high vacuum chamber that was capable of being cooled to -24 °C. An LED was used to illuminate the sensor at room temperature and the result of this after background subtraction is shown in Figure 5.7. With no defects present, the image would show an area of highest signal in the centre and then decreasing areas of signal radially from there. However, there were two clear defects present in the sensor. Firstly, there were diagonal bands of lower signal regions evenly spaced across the detector. Secondly, there were about 100 defective pixel clusters that displayed significantly lower signal values than their neighbours.

The diagonal bands appeared to have been present from the fabrication process. They are not visible by simply taking a dark image. These large bands correspond to the striped bands in the gain measurements of Figure 5.6. When illuminated, there is a 12% difference in the signal from the centre of a dark band to the centre of an adjacent brighter band. This level of difference was maintained at both room temperature and at -24 °C.

Immediately after fabrication there were no dead or defective pixels. The defective pixels were created by changing the temperature of the sensor too rapidly during the baking process. The sensor was subjected to slower cooling and warming cycles over a three day period, and no new defective pixels were detected. The locations of the defective pixel clusters are shown in Figure 5.8. These pixels gave signal responses that were at least 15% less than the average of their 8 nearest neighbours, and there were 187 pixel clusters identified, corresponding to around 400 defective pixels. The clusters are typically between one and four pixels in size.

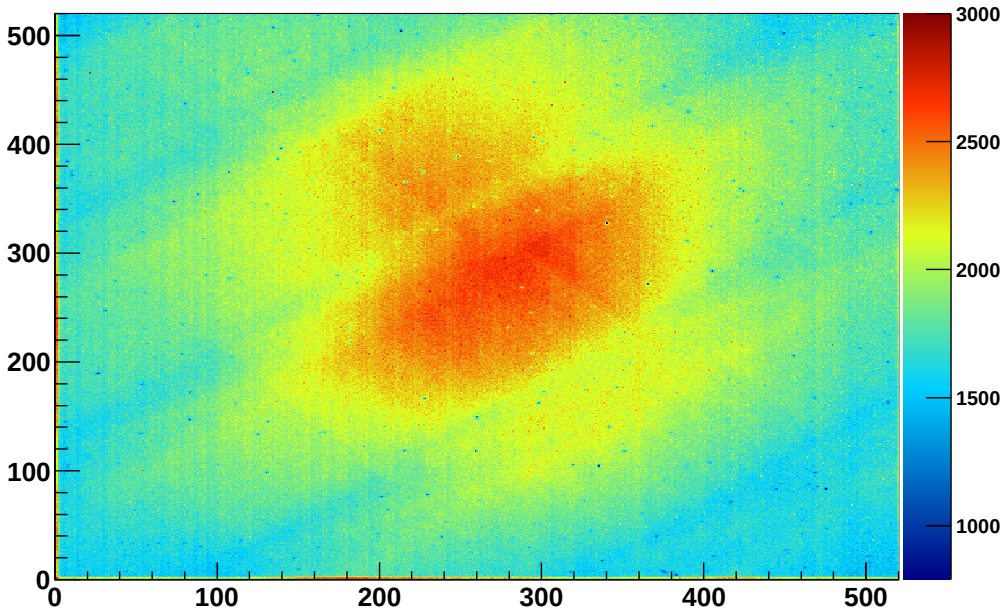

Figure 5.7: Example of point defects created by the baking process. The diagonal bands were created during the fabrication process.

This was equivialent to less than 0.2% of the surface area of the sensor and was considered neglible to the following results.

In previous work [11], the stability of a Vanilla APS was measured by taking dark images every half hour over a three day period. It was shown that the magnitude of the signal was proportional to the room temperature, and that the 15% change in the signal generated by the dark current between day and night would equate to a 1.1 °C change in the temperature of the sensor.

A similar measurement was made over a period of half an hour instead of three days, and this is shown in Figure 5.9. The measurement, taken at 20 °C, showed a change of 0.2% in the signal resulting from the dark current over the 30 minutes - equating to a change of 0.01 °C in the temperature of the sensor. This would be an adequate stability for the sensor in an experiment.

As the temperature was changed, the pedestal signal was measured as a function of integration time. The average dark signal recorded increased with longer integration times. Furthermore, as the sensor temperature decreased both the level of pedestal signal and the

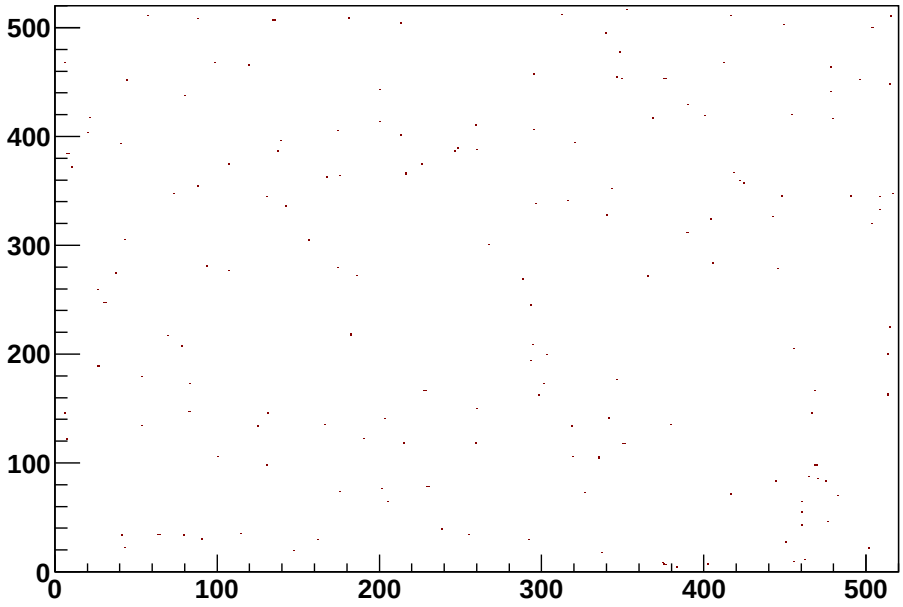

Figure 5.8: Location of defective pixel clusters created by the baking process. These pixels are at least 15% less than the average of their 8 nearest neighbours.

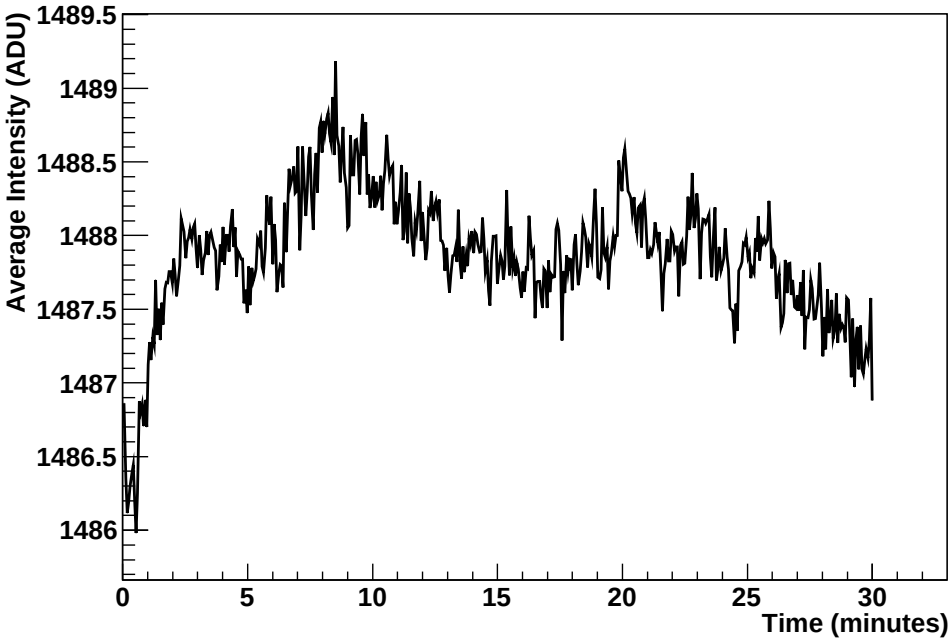

Figure 5.9: Measurement of stability of the Vanilla APS over a period of 30 minutes at -24 °C.

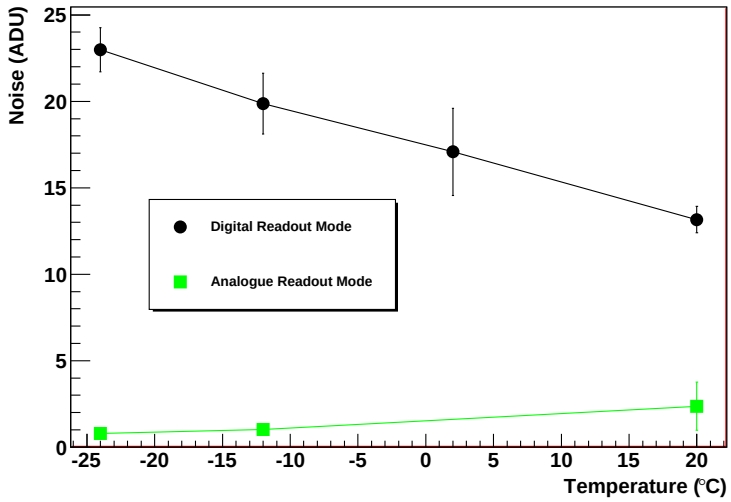

Figure 5.10: Measurement of the total noise in a Vanilla APS with Analogue and Digital readout modes at temperatures varying from -24 °C to 20 °C.

dark current decreased. This same effect was seen with both the analogue and digital readout modes.

However, there are differences between the analogue and digital modes when comparing the dark noise as the temperature decreases. For the analogue readout mode, the dark noise is reduced as the temperature decreases. This is the expected behavior if the dark noise is mainly composed of thermal effects. However, the digital readout mode showed the opposite response to the decreased temperature. In this case the decreasing temperature caused the noise to increase. This is shown in Figure 5.10.

This result occurs because the sensor itself is less noisy at lower temperatures, leading to lower noise readings in the analogue mode. However, the electronics associated with the digital readout were not designed to be operated below room temperature and consequently increase the readout noise. This readout noise completely dominates any signal generated by the dark current. These electronics were designed with room temperature operation in mind, and were not tested at lower temperatures.

5.3 Results from the Synchrotron Experiment

The purpose of this section was to perform a typical synchrotron experiment with both the Princeton CCD and the Vanilla APS. The differing sensor technologies could then be compared and contrasted.

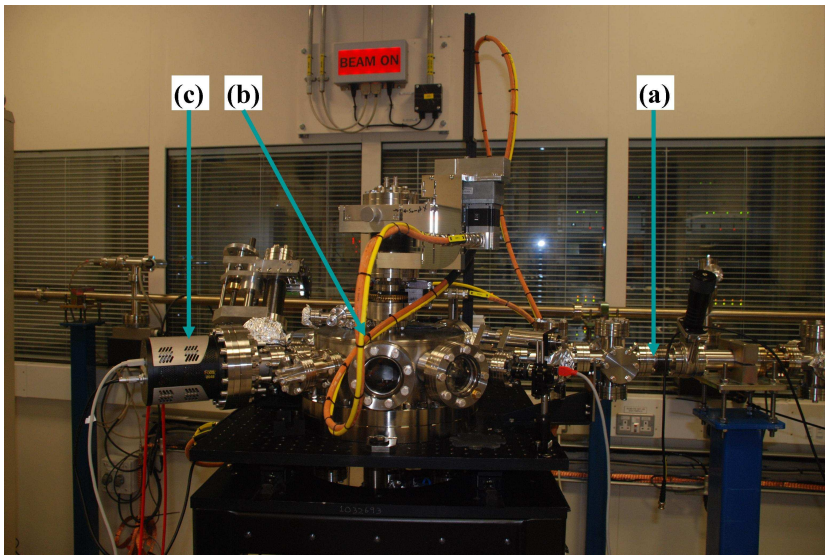

Figure 5.11: Photograph of experimental set up, showing the beamline labeled (a), the permalloy sample labeled (b) and the position of the detector labeled (c).

The standard experiment chosen was a simple X-ray diffraction experiment. Beamline I06 was selected to use soft X-rays, at 708 eV (wavelength of 1.75 nm), to create a diffraction pattern from a permalloy sample. Permalloy is typically an alloy of iron and nickel in proportions of 1:4. The sample used in the experiment also had small concentrations of tungsten and aluminium on a silicon support. The setup is shown in Figure 5.11. This is typical of a soft X-ray experiment [100].

The sample could be rotated freely in θ and ϕ directions to allow the same spots to be imaged by the different detectors. The physical area of the CCD sensor was about four times larger than the area of the Vanilla APS, and the mount for the sensor electronics was also much larger. This meant that the sample had to be rotated slightly when moving between the CCD and the APS to ensure that the same diffraction spots were being imaged.

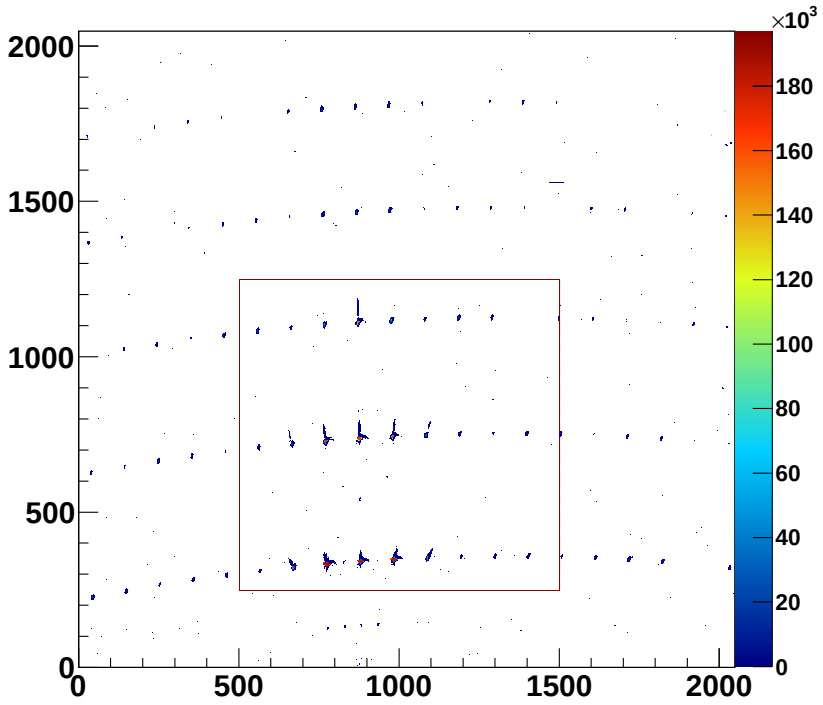

Figure 5.12: CCD image with the longest integration time (300 s). Image has had pedestals subtracted. X and Y axes show the pixel number. The red rectangle indicates the region that was imaged by the Vanilla APS. Blooming effects cause the charge to spread radially outwards from the centre of the diffraction pattern. The second order diffraction spots are the set between y = 600 and y = 700.

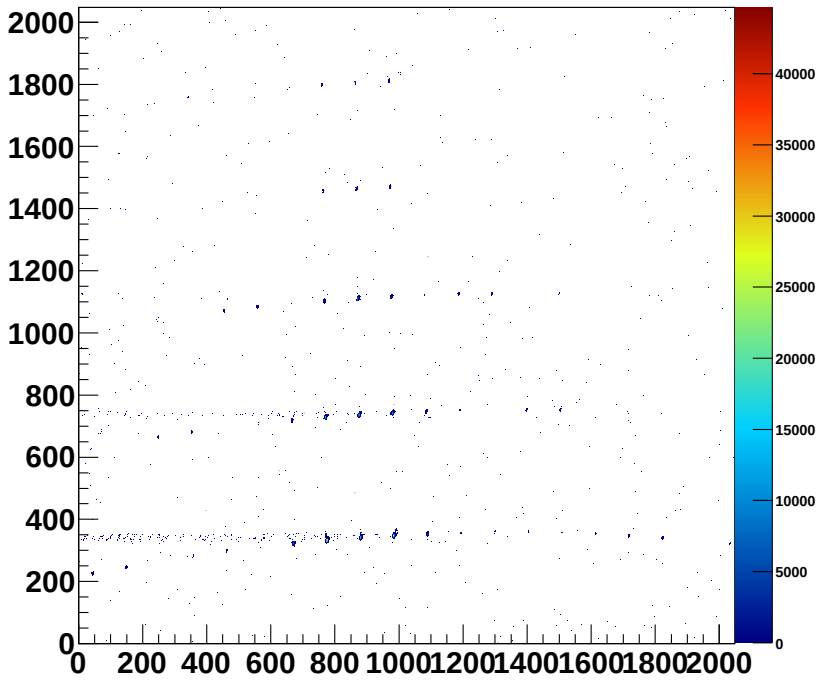

Figure 5.13: CCD image from the shortest integration time (10 s). Image has had pedestals subtracted.

5.3.1 CCD and APS Signals with varying Frame Rates

Both the APS and CCD were used to take images of the diffraction pattern at a variety of frame rates. The Vanilla images cover a quarter of the area of the CCD images, and so are only a subset of the diffraction pattern. The integration time to capture the images was varied between 10 seconds and 5 minutes for the CCD, and between 0.05 seconds and 10 seconds for the Vanilla APS. The large differences in the two ranges used is partly a result of the sort of applications the detectors were designed for. The CCD was designed to take long-exposure images whereas the APS was designed to image in real-time.

From these images, a simple line profile through the second order diffraction spots can be used to derive a straightforward peak to trough ratio by taking the ratio of the highest peaks to the average of the inter-spot regions. In order to get the largest signal to noise ratio possible, the CCD used the low noise readout mode and was cooled to -55 °C whereas the Vanilla APS was cooled to -10 °C. The difference temperatures and readout modes make to

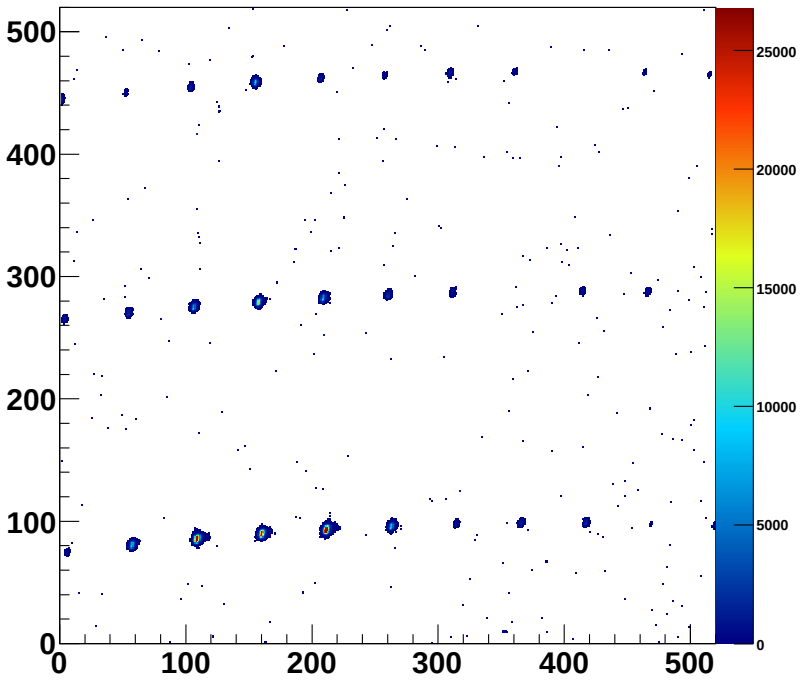

Figure 5.14: Vanilla APS image from the longest integration time (10 s). Image has had pedestals subtracted.

the noise level is discussed in Sections 5.3.1.1 and 5.3.1.2.

A pedestal subtraction was performed on all of the images. In order to do this, a series of dark images were taken at each integration time and then averaged. In the series of frames, the first few would be ignored until the average signal across the sensor becomes stable. The remaining dark images were averaged and this was then used as the pedestal image.

The CCD image from the longest integration time of 300 s displays an effect known as blooming and this is shown in Figure 5.12. This is where a pixel is overloaded by incoming signal, and the charge floods into neighbouring pixels. This is most apparent from the diffraction spots with the greatest collected charge, and the blooming appears to spread the charge radially outwards from the centre of the diffraction pattern. This also leads to the diffraction spots appearing wider on the corresponding line profile, in Figure 5.16(a). This is a feature of CCDs that is not present in APS images. The cut applied to the pixels in the image was set at 155 e^- to allow the fainter spots to be displayed without being swamped in noise hits.

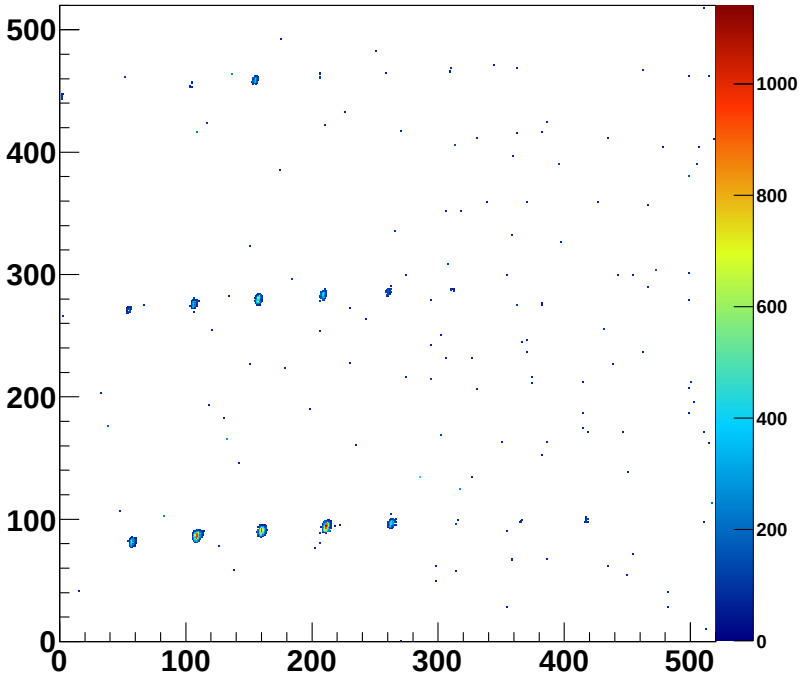

Figure 5.15: Vanilla APS image from the shortest integration time (0.05 s). Image has had pedestals subtracted.

Along with the presence of nearly every diffraction spot in the first four lines, one interesting feature is the presence of half-order diffraction spots. These are present only just above the level of the noise and consist of four spots with x-coordinates between 750 and 1000 and y-coordinates between 100 and 150.

With the shortest integration time of 10 s, the CCD does not display any blooming artifacts because there is not enough time to collect sufficient charge to saturate any pixels. A smaller proportion of the diffraction pattern is also visible as some of the fainter spots do not produce enough charge within the 10 s limit. There is, however, a different feature of CCD images visible. In this setup, the columns are read out from the furthest pixel to the right and the charge is passed along to the left of the device. The charge from the pixels with the greatest charge collected leave trails of charge in the subsequent pixels after they are read out. Any integration time less than 10 s would cause this trail to increase greatly. This is due to the CCD having an imperfect charge transfer efficiency. Even the quoted efficiency of 99.9998% will cause some of the charge to be left behind with a short reset time.

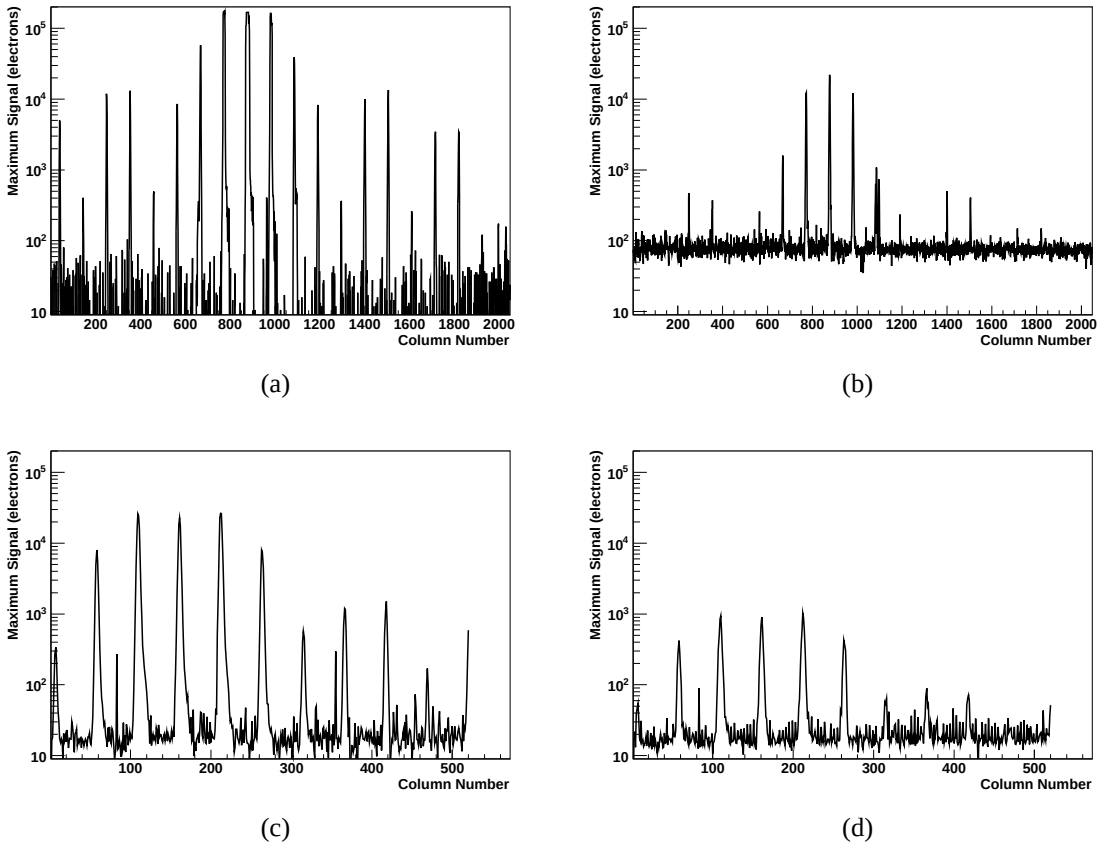

Figure 5.16: Line profiles for the CCD with the longest integration time (300 s) (a) and shortest integration time (10 s) (b) and the Vanilla APS for the longest integration time (10 s) (c) and shortest integration time (0.05 s) (d).

When the Vanilla APS was used with an integration time of 10 s, the blooming and streaking artifacts associated with the CCD images are not present. This is displayed in Figure 5.14. The noise cut applied to the APS images was lower than the CCD, at a level of 73 e^-. This was done to allow spots in the three orders of diffraction spots to be clearly visible. Although this noise level was under half what the CCD displayed, the maximum signal is also reduced. The maximum signal collected by the CCD in 10 s of integration is 44 000 e^- whereas the Vanilla APS only collected 26 000 e^- due to the difference in fill factors. The same spots in the diffraction pattern are visible in this image as in the longer CCD exposure, although a smaller area was imaged.

Even when the integration time for the Vanilla APS was reduced to its minimum of 0.05 s, as in Figure 5.15, the major peaks in the faintest line of diffraction spots are still visible above the background noise.

The line profiles for each of the devices and integration times are shown in Figure 5.16. These line profiles were created in a process with multiple stages. Firstly, by taking rectangle across the width of the image and 60 pixels wide, an entire line of diffraction spots from the CCD could be encompassed. The width used for the Vanilla APS was only 30 pixels, due to the larger pixel size and the reduced spread in the spots. Then, for each x-position the highest signal pixel would be sought. This was then averaged with its neighbours from either side to give a value that should accentuate the diffraction signal peaks whilst limiting the noise in the inter-spot regions. In this sense, it is not a true signal to noise measurement, rather it measures the peak signal value to the trough value.

The line profile for the longest CCD exposure, shown in Figure 5.16(a), shows the maximum signal of the brightest spots at over 10^5 electrons with an average trough value of 10 electrons giving a peak to trough ratio of 10^4. The effect of blooming can also be seen strongly in the central three peaks with the largest signals. Here, the flat tops to the peaks show that the pixels are saturating and the broadening of the peaks shows the charge spilling out from the saturated pixels into the neighbours. When compared to the line profile of the shorter integration time in Figure 5.16(b) it can be seen that there is no saturation in the signal. The middle peak of the three that previously saturated is now clearly larger than the others and this signal reaches 20 000 electrons. The main difference in this line profile is that the trough value has risen to 80 electrons, reducing the peak to trough value to 2.5 x 10^3. In particular, the mean trough value increases from 72 ± 2 e^- to 80 ± 2 e^- after the peaks of greatest signal due to the trail of charge remaining from the frame readout.

The Vanilla APS line profiles, shown in Figures 5.16(c) and (d), are for the integration times of 10 seconds and 0.05 seconds. In both profiles, the same peaks can be seen with the same relative heights between the peaks. The trough value is the same in both images at 20 electrons and is independent of the integration time. This gives a variation in the peak to trough ratio of 5 x 10^2 for the shortest integration time up to 1.5 x 10^3 for the longest integration time, which compares very well to the equivalent CCD values with a 10 s integration time.

Whilst the peak to trough is a figure of merit, the later signal to noise analysis of Section 5.3.1.3 is of greater relevance.

5.3.1.1 Dark Current

In any photosensitive device, a small current will be present even when there are no incident photons. This is due to the random creation of electrons and holes in the depletion region due to thermal effects. The dark current can cause noise that can be removed by pedestal subtraction. It also has a temporal component that adds to the shot noise. The CCD used showed significantly less dark current than the Vanilla APS and this is shown in Figure 5.17, due to the temperature at which the detector was cooled to. The CCD was cooled to -55 °C in order to improve the signal to noise performance significantly. The Vanilla's measurements of dark current display non-linear traits. This is explained by the reset noise of the sensor beginning to dominate the other sources of noise. The reset noise is not temperature dependent, so provides a noise floor.

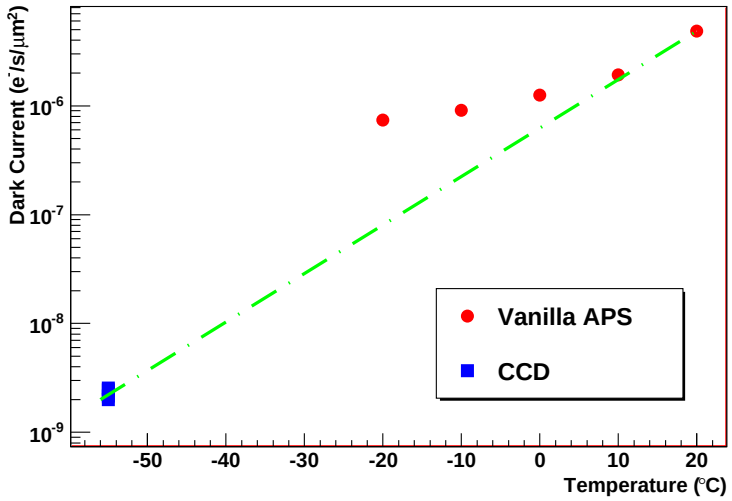

Figure 5.17: The measured dark current against sensor temperature for the Vanilla APS and the CCD. Vanilla reached a dark current of 10^{-6} $e^-/s/\mu m^2$ at -20 °C, and the CCD dark current was 2 x 10^{-9} $e^-/s/\mu m^2$ at -55 °C. The green dashed line represents the extrapolation resulting from halving the dark current every 7 °C.

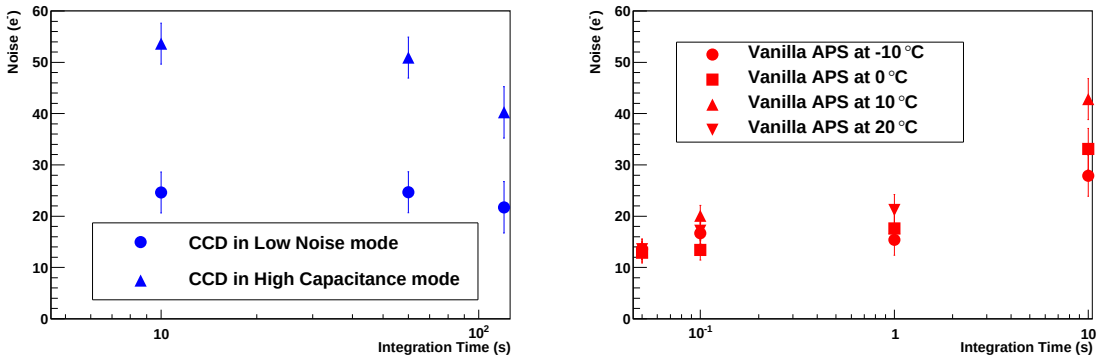

(a) (b)

Figure 5.18: Noise levels for the CCD (a) and Vanilla APS (b). The Vanilla APS has comparable noise to the CCD's low noise mode at short integration times.

5.3.1.2 Noise Measurements

In order to quantify the dark noise, a series of dark images were recorded. The Vanilla APS was recorded at different temperatures with various integration times, whereas the CCD used its different imaging modes for various integration times and with a sensor temperature of -55 °C. From these, the average pedestal signal was subtracted and the variance of the resultant image gives the read noise. These are shown in Figure 5.18(a) and (b) for the CCD and the Vanilla APS respectively. At -55 °C, the CCD's two modes, low noise and high capacity, each have different noise levels. The low noise mode has a noise level of around 20 electrons, whereas the high capacity mode has a level of around 50 electrons. Changing the gain of each of the independent modes has no significant effect on the level of the noise.

The Vanilla's noise was around 20 electrons, increasing to 35 electrons at the longest integration time. This is around the level of the low noise mode of the CCD.

The longest CCD integration time (300 s) suffered from unusually high levels of noise. For this length of integration, only a single background frame was recorded. This meant the background had greater noise and a pedestal subtraction was not possible. As a result the CCD data with a 300 second integration time will not be included in future measurements.

5.3.1.3 Signal to Noise Analysis

Once the noise values were calculated, the Signal to Noise (S/N) measurement was made by summing the charge from a spot and then comparing this with the calculated noise level. This is shown in Figure 5.19. In order to make a fair comparison, the brightest spot in the second order diffraction spots was chosen. This was done to prevent saturation affecting the result. The full spot was integrated by beginning with the brightest pixel and adding adjacent pixels to the cluster as long as they were four times the background level. When this was done, the total charge collected increased linearly with integration time until saturation, with the CCD S/N ratio increasing from 200±50 to 1800±100 and Vanilla APS S/N ratio increasing from 20±10 to 150±25. When comparing the same integration times, the two detectors have comparable S/N ratios. The difference between the performances is primarily due to the temperature at which they were operated.

The S/N measurement is an important figure of merit for diffraction experiments. The ability to image the less intense spots within the diffraction pattern will be impeded by a low S/N value. In this case, the background noise would obscure some of the spots. Both detectors tested here displayed S/N values that were appropriate for diffraction experiments.

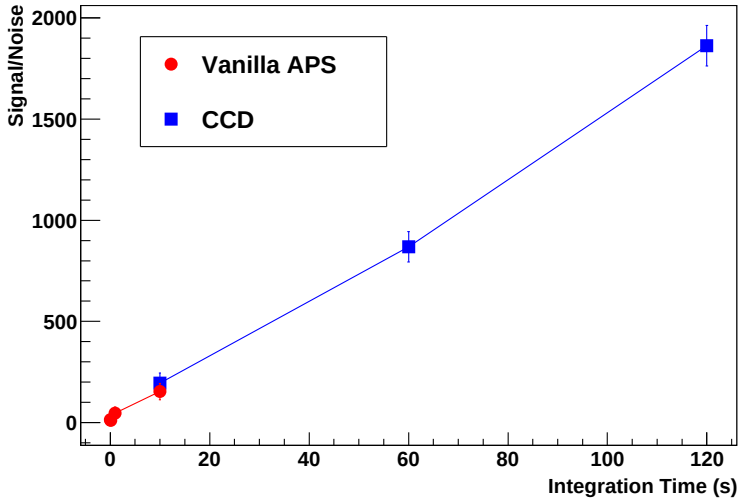

Figure 5.19: Integrated Signal to Noise ratios for CCD and Vanilla integration times.

5.3.1.4 Image Lag

One of the main differences between the reset modes of the Vanilla APS is the amount of residual signal remaining from one frame to the next. This is referred to as the image lag. In order for this effect to be quantified for each reset mode of the device, a single spot of the diffraction pattern was studied. A series of 500 frames were recorded, at 55 frames per second. Initially the diffraction pattern was visible on the sensor. After about a second of data taking, the beam was switched off. The remaining data taking period would show the effect the previous frame's signal had on the next. This was repeated for each reset mode. The image lag was calculated after a background subtraction was performed.

By only considering the brightest spot in the diffraction pattern, the charge collected in that spot in each frame can be summed to determine the image lag. This is shown in Figure 5.20. The normalised signal is calculated by taking the charge summed from a square of 12 pixels by 12 pixels around the brightest pixel, and normalising the signal prior to removing the beam. From this plot, it can be seen that the hard reset mode reduces the signal to the noise floor almost immediately. There was a hard cut at 0 signal. The hard reset mode reaches 10% of the initial value within 0.03594 seconds (1 frame) and oscillates between 10% and 0% from the 2nd frame onwards. This oscillation is caused by the large noise associated with the hard reset mode. In contrast, the soft and flushed reset modes take a lot longer, although clearly have lower noise as a result. The flushed reset mode reaches 10% after 0.32348 seconds and the soft reset mode takes 0.98842 seconds or about three times longer than the flushed reset. This is due to signal after a flushed reset undergoing an exponential decay whereas after the soft reset the signal appears to plateau for almost a second.

The greater the signal level that a group of pixels initially have relative to the noise level will decrease the time required to reduce the signal to 10% or 1% of the inital value. If a smaller region than the 12 by 12 square is considered, the times are reduced accordingly. By taking a 5 by 5 square, the hard reset image lag is not reduced at all. However, the flushed and soft reset modes now reach 10% after a single frame and reach 1% after 2.0667 seconds and 4.9601 seconds respectively. This is because the 5 by 5 square initially has a higher

average value per pixel. The 10% and 1% thresholds are consequently at a greater level as well.

The noise performance of the flushed reset mode matches that of the soft reset closely. One possible method for improving the flushed reset further would be to increase the length or intensity of the hard reset period. Whilst this will increase the reset noise slightly, there should also be a further reduction in the image lag.

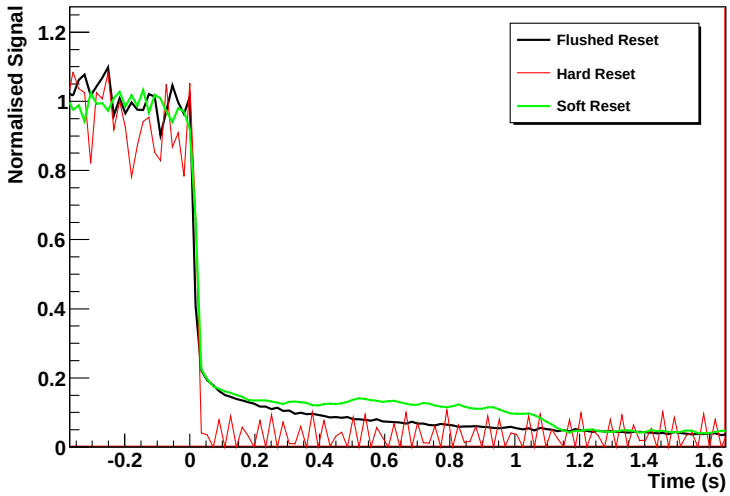

Figure 5.20: Image lag of the Vanilla APS with hard, soft and flushed reset modes.

5.4 Conclusions

The Vanilla sensor, despite not being designed specifically for the experiment performed, showed competitive results in comparison to the CCD. These results are displayed in Table 5.2. The frame rate of the Vanilla is an order of magnitude greater than the CCD with full frame readout. Reading out a 60 x 60 pixel square of the Vanilla sensor increases the frame rate by another order of magnitude. Further work remains to be carried out to investigate the maximum frame rate the sensor can be run at.

The read noise of the CCD is more stable at 20 e^- or 50 e^- depending on the collection mode. The read noise in the Vanilla APS has a larger variation in its range between 15 e^- and 50 e^-. The peak to trough ratio is greater for the CCD than for the Vanilla APS, although

	Princeton PIXIS CCD	Vanilla CMOS APS
Frame Rate	0.1 fps - 0.003 fps	20 fps - 0.1 fps (300 fps ROI)
Gain	HC mode - $\sim$14 e^-/ADU LN mode - $\sim$3 e^-/ADU	Analogue - $\sim$15 e^-/ADU Digital - $\sim$7 e^-/ADU
Operating Temperature	-55 °C	-10 °C
Read Noise	20 e^- - 50 e^-	15 e^- - 50 e^-
Peak to Trough	2.5 x 10^3 - 10^4	5 x 10^2 - 1.5 x 10^3
Signal to Noise	200 - 1800	20 - 150

Table 5.2: Comparison of the key characteristics of the CCD and Vanilla sensors.

this measurement fails to take into account certain features of the images such as blooming and streaking. However, the signal to noise ratio is comparable between the CCD and the CMOS APS at identical integration times. The Vanilla APS is also able to be operated at much higher temperatures. Even at room temperature, the sensor's noise does not dominate the signal. As a consequence, there are many applications where an APS sensor could outperform a traditional CCD.

Chapter 6

Conclusions

In the years to come, there will be successive advances in synchrotron technology and high energy physics. This, in turn, will drive forward developments in their associated detectors. Silicon pixel detectors will be at the forefront of this wave.

Firstly, one of the main advances that will require novel detectors will be in the area of high luminosity colliders. The new colliders will require detectors that are resistant to the high radiation environment. Also, these experiments will require a large active area and a fast readout system. Improvements to 3D detectors will offer solutions to some of these problems.

A 3D detector is one in which the doped electrodes extend through the bulk of the detector. This differs to a planar device that has highly doped electrodes on the surfaces of the device. The main advantage to this is that the opposing electrodes can be constructed to be far closer together. A double sided 3D detector has the opposing electrodes extending from the opposite sides, but not for the full depth. This has the advantage of there being no completely dead areas for a MIP to pass through.

Secondly, the requirements for new sensors in synchrotron environments will mean that imaging sensors with a faster readout capability than currently utilised will be essential. Whilst some traditional CCDs may will have this capability, newer CMOS sensors may offer alternative advantages in some situations. Due to the manner in which a CMOS sensor is designed, the possibility of on-chip intelligence is greatly increased.

Development of these technologies will also offer further benefits in different applications. Any benefits accrued by CMOS sensors in a synchrotron experiment can also be utilised in an area such as medical imaging or in low power applications such as in digital cameras.

In Chapter 3 a double-sided 3D Timepix device was studied and characterised in a pion testbeam. A telescope consisting of 3 planes before the DUT and 3 planes after was utilised in order to measure the position and time in which each pion interacted with the DUT. By matching the measured hits to the telescope-predicted tracks, a number of conclusions about the sensor could be drawn.

A MIP incident on the detector will lose a portion of its energy generating electron hole pairs in the silicon of the device. If the MIP completely misses the dead areas at the electrodes, then it will generate around 32 ToT counts in the device. If the MIP passes through the central electrode, then the value of the counts generated will be cut to about a quarter. When the MIP passes close to the edge of the device then the charge will be split between the neighbouring pixels. This occurs because there will be a small amount of diffusion of the charge between its generation and collection. In a 3D device this charge sharing effect was shown to have a very limited effect. The majority of the charge sharing occurred at the edges between columns. Tracks incident on a corner column directly would not generally share charge because when the reduced amount of charge was split between multiple pixels it would fall below the threshold that was set. Even with the DUT rotated to 10°, around 40% of the incident tracks are still contained within a single pixel. The main difference that the rotation has is that the charge deposited is now independent of the track entry position. The majority of the tracks will pass through at least part of a column and a larger part of active silicon. The total charge generated will be slightly greater than for perpendicular tracks because the MIP spends a greater length of time within the detector.

When only the area of the detector away from the columns for perpendicular tracks, the efficiency of the device was greater than $99.7 \pm 0.5\%$. When the entire device is considered this drops to $93.0 \pm 0.5\%$, with the reduction due to the electrodes at the centre and the corners

and the charge sharing at the edges. When the device was rotated to 10° the efficiency increased further, up to 99.7±0.5%.

The last measurement that was made during the testbeam was of the resolution of the device. This was reduced from 15.81±0.10 μm with perpendicular tracks to its minimum of 9.81±0.10 μm with tracks of 10°.

One piece of detector technology that will provide benefits to many different designs of sensors is the ability to tile multiple sensors. If the dead space taken up by the guard ring structures can be reduced, then the overall active area of the detectors will be increased. This in turn will allow larger area sensors to be created. This aspect was investigated in Section 3.5.

A strip detector was created where one edge perpendicular to the strips had the traditional guard ring structures and the other edge had a reduced edge structure. This was fabricated using an SCP process. The sensor was then scanned across both edges using a 11 μm FWHM 15 keV micro-focused X-ray beam. A pedestal measurement showed that while the strip closest to the cleaved edge had a higher level of noise, no other strip was affected. The charge collection in the strips adjacent to the cleaved edge showed the same collection profile as the strips adjacent to the full guard rings.

The analysis of double-sided 3D detectors continued in Chapter 4. In this chapter, the detector had the columns connected together in short strips and it had a larger strip pitch (80 μm as opposed to 55 μm) than the previous, Timepix sensor. A Transient Current Technique (TCT) experiment was performed in order to map the charge collection and velocity profiles in the device.

A TCT measurement is performed by using a short laser pulse to generate pairs of electrons and holes at a specific position within a detector. The drift of these carriers induced a current pulse. By using a precise XY-stage, scans with a resolution of 2.5 μm were performed. This technique was repeated for both the top surface and the edge perpendicular to the strips of the 3D detector. The top surface measurements were then repeated after the detector had been irradiated to a dose of 5 x 10^{15} 1 MeV equivalent neutrons/cm^2 and after

annealing in stages up to 300 minutes.

The maps of charge collection and carrier velocity were created for various bias voltages. When the edge of the non-irradiated device was illuminated, the charge collection in the central portion of the device saturated with a bias voltage of around 4 V. Increasing the bias voltage above this level caused an increase in the charge collection in the regions closest to the top and bottom surfaces of the detector. Unlike the charge collection, the velocity of the charge carriers carried on increasing with the bias voltage as this is proportional to the electric field. The low electric field portions of the device, such as between the tip of a column and the top surface, showed only a limited carrier velocity, even with an applied bias of 20 V.

Illuminating the top surface of the device showed a similar response. Again, the charge collection saturated at the lateral depletion voltage whereas the velocity carried on increasing until the device was fully depleted. In this case, however, the response of the detector resulting independently from the motion of electrons and holes is measurable.

When the detector was irradiated, a number of new effects were seen. Firstly, the response from illumination is now due entirely to the motion of electrons. The holes are trapped prior to collection. Secondly, the areas of greatest velocity and charge collection are now around the n-type electrodes and where the greatest electric field occurs - between the n-type and p-type electrodes. Thirdly, with bias voltages greater than 200 V, there is evidence of charge multiplication occurring. By this level of bias, the velocity is saturated so the increase in charge collection can only be due to charge multiplication. Annealing the device exacerbates these effects.

There is further work remaining to be completed on these sensors. An edge TCT measurement of an irradiated 3D detector will add valuable information to that already assembled. This would provide a more detailed study of the effect of irradiation on the electric field around the column tips and near the top and bottom surfaces of the detector. A further study of the irradiated device in a testbeam would also allow the effect the irradiation has on the efficiency to be observed. This effect will be of particular importance at the area around

the electrodes.

A novel CMOS based sensor was compared to a typical CCD in Chapter 5. The CCD used in the experiment was a Princeton PIXIS-XO: 2048B, which is typical of the devices used by the Diamond Light Source and other synchrotrons. The CMOS sensor used was a prototype APS called the Vanilla sensor, which had been designed in conjunction by RAL and the University of Glasgow.

Before any comparison of the sensors could be made, the Vanilla APS first needed to be characterised in a lab. A per pixel PTC measurement was employed to calculate the gain of each pixel in the sensor. When averaged across the whole pixel matrix, a value for the gain of 7.912 e^-/ADU was evaluated. It was also shown that although the gain varied randomly across the sensor, there were some patterns that were indicative of the overall performance. Firstly, every fourth column show a similar level of response. This resulted from the readout electronics whereby four columns are read out together. Secondly, there were striped diagonal bands of higher and lower gains that were created during the fabrication process. These bands were also visible in the first cold temperature measurements that were performed. This first measurement also identified around 400 dead pixels; this represented around 0.2% of the total pixels in the sensor.

The Vanilla APS had two different readout modes. There was a digital readout mode that was designed for a fast, full-frame readout, and an analogue mode designed for region of interest measurements. As the sensor was cooled from 20 °C to -24 °C, the noise performance of the two readout modes differed. The noise associated with the analogue readout mode decreased due to a reduction in the thermal noise as would be expected. However, the noise associated with the digital mode increased slightly. This was a result of the on-chip electronics used in the prototype not being designed for operation at low temperatures. As a result, the digital mode was used solely in the comparison with the CCD.

A fairly standard X-ray experiment was selected in order to test the capabilities of the two sensors. A permalloy sample was used to create a diffraction pattern that was then imaged. The CCD was operated at a temperature of -60 °C and with frame rates varying between

0.1 and 0.003 frames per second. The Vanilla APS was operated at -10 °C and between 20 and 0.1 frames per second. It was shown that the Vanilla APS had a comparable signal to noise and read noise performance to the CCD, despite being operated at a much greater temperature.

Bibliography

[1] W.C. Röntgen. On a new kind of rays. *Science*, 3(59):227–231, 1896.

[2] N.N. Das Gupta and S.K. Ghosh. A report on the Wilson Cloud Chamber and its applications in physics. *Rev. Mod. Phys.*, 18:225–290, Apr 1946.

[3] C.D. Anderson. The positive electron. *Phys. Rev.*, 43:491–494, Mar 1933.

[4] G.D. Rochester and C.C. Butler. Evidence for the existence of new unstable elementary particles. *Nature*, 160(855):173, 1947.

[5] D.A. Glaser. Some effects of ionizing radiation on the formation of bubbles in liquids. *Physical Review (US) Superseded in part by Phys. Rev. A, Phys. Rev. B: Solid State, Phys. Rev. C, and Phys. Rev. D*, 87, 1952.

[6] H. Ing, T.D. McLean, and R.A. Noulty. Bubble detectors - a maturing technology. *Radiation Measurements*, 27(1):1 – 11, 1997.

[7] Y. Akimov. Silicon radiation detectors (review). *Instruments and Experimental Techniques*, 50:1–28, 2007.

[8] S.I. Parker, C.J. Kenney, and J. Segal. 3D - a proposed new architecture for solid-state radiation detectors. *NIM A: Accelerators, Spectrometers, Detectors and Associated Equipment*, 395(3):328 – 343, 1997. Proceedings of the Third International Workshop on Semiconductor Pixel Detectors for Particles and X-rays.

[9] A. Blue et al. Characterisation of edgeless technologies for pixellated and strip silicon detectors with a micro-focused X-ray beam. *JINST*, 8(01):P01018, 2013.

[10] P. Magnan. Detection of visible photons in CCD and CMOS: A comparative view. *NIM A: Accelerators, Spectrometers, Detectors and Associated Equipment*, 504(1):199–212, 2003.

[11] A. Blue et al. Characterisation of Vanilla–A novel active pixel sensor for radiation detection. *NIM A: Accelerators, Spectrometers, Detectors and Associated Equipment*, 581(1):287–290, 2007.

[12] E.M. McMillan. The synchrotron - a proposed high energy particle accelerator. *Physical Review*, 68(5-6):143–144, 1945.

[13] M. Moll et al. Development of radiation tolerant semiconductor detectors for the Super–LHC. *NIM A: Accelerators, Spectrometers, Detectors and Associated Equipment*, 546(1 - 2):99 – 107, 2005. Proceedings of the 6th International Workshop on Radiation Imaging Detectors.

[14] N. Allinson et al. The multidimensional integrated intelligent imaging project (MI-3). *NIM A*, 604(1):196–198, 2009.

[15] S.M. Sze. *Semiconductor Devices: Physics and Technology*. John Wiley & Sons, 2008.

[16] M. Faraday. Experimental Researches in Electricity. Fourth Series. *Philosophical Transactions of the Royal Society of London*, 123:pp. 507–522, 1833.

[17] W. Shockley. The theory of pn junctions in semiconductors and pn junction transistors. *Bell Syst. Tech. J*, 28(3):435–489, 1949.

[18] S.M. Sze and K.K. Ng. *Physics of Semiconductor Devices*. John Wiley & Sons, 2006.

[19] G.L. Miller, W.L. Brown, P.F. Donovan, and I.M. Mackintosh. Silicon p-n junction radiation detectors. *Nuclear Science, IRE Transactions on*, 7(2-3):185 –189, june 1960.

[20] G.F. Knoll. *Radiation Detection and Measurement*, volume 1. John Wiley and Sons, Inc., 1979.

[21] G. Lutz. *Semiconductor Radiation Detectors*. Springer, 2007.

[22] V. Gligorov et al. Charged particle tracking with the Timepix ASIC. *NIM A: Accelerators, Spectrometers, Detectors and Associated Equipment*, 661(1):31 – 49, 2012.

[23] E. Belau, T. Böhringer, L. Hubbeling, J. Kemmer, R. Klanner, U. Kötz, G. Lutz, E. Neugebauer, M. Riebesell, H.J. Seebrunner, P. Weilhammer, and A. Wylie. Charge collection in silicon strip detectors. *Nuclear Instruments and Methods in Physics Research*, 214(2 - 3):253 – 260, 1983.

[24] G. Pellegrini et al. Double sided 3D detector technologies at CNM-IMB. *Nuclear Science Symposium Conference Record, IEEE*, 2:1248–1252, 2006.

[25] J. Kemmer. Improvement of detector fabrication by the planar process. *NIM A: Accelerators, Spectrometers, Detectors and Associated Equipment*, 226(1):89 – 93, 1984.

[26] Y.H. Cho, T. Fujii, B.J. Kim, and S.W. Lee. Fabrication of silicon dioxide submicron channels without nanolithography for single biomolecule detection. *Nanotechnology*, 18(46):465303, 2007.

[27] S. Altenheiner, C. Goessling, J. Jentzsch, R. Klingenberg, T. Lapsien, D. Muenstermann, A. Rummler, G. Troska, and T. Wittig. Planar slim-edge pixel sensors for the ATLAS upgrades. *JINST*, 7(02):C02051, 2012.

[28] E. Noschis et al. Final size planar edgeless silicon detectors for the totem experiment. *NIM A: Accelerators, Spectrometers, Detectors and Associated Equipment*, 563(1):41 – 44, 2006. Proceedings of the 7th International Workshop on Radiation Imaging Detectors.

[29] C.J. Kenney, C. Da Via, J. Hasi, J. Morse, S. Parker, J.D. Segal, S. Watts, and E. Westbrook. Active-edge planar radiation sensors. *NIM A: Accelerators, Spectrometers,*

Detectors and Associated Equipment, 565(1):272 – 277, 2006. Proceedings of the International Workshop on Semiconductor Pixel Detectors for Particles and Imaging.

[30] A. Kok, G. Anelli, C. Da Via, J. Hasi, P. Jarron, C. Kenney, J. Morse, S. Parker, J. Segal, S. Watts, and E. Westbrook. 3D detectors - state of the art. *NIM A: Accelerators, Spectrometers, Detectors and Associated Equipment*, 560(1):127 – 130, 2006.

[31] C. Da Via, G. Anelli, J. Hasi, P. Jarron, C. Kenney, A. Kok, S. Parker, E. Perozziello, and S.J. Watts. Advances in silicon detectors for particle tracking in extreme radiation environments. *NIM A: Accelerators, Spectrometers, Detectors and Associated Equipment*, 509(1 - 3):86 – 91, 2003. Proceedings of the 4th Internatonal Workshop on Radiation Imaging Detectors.

[32] S. Parker, C. Kenney, J. Segal, and C. Storment. Silicon detectors with 3-D electrode arrays: fabrication and initial test results. *Nuclear Science, IEEE Transactions on*, 46(4):1224 –1236, aug 1999.

[33] P. Grenier et al. Test beam results of 3D silicon pixel sensors for the ATLAS upgrade. *NIM A*, 638:33–40, 2011.

[34] C.J. Kenney, S. Parker, and E. Walckiers. Results from 3-D silicon sensors with wall electrodes: near-cell-edge sensitivity measurements as a preview of active-edge sensors. *Nuclear Science, IEEE Transactions on*, 48(6):2405–2410, 2001.

[35] R.L. Bates, J.P. Balbuena, M. Breindl, X. Blot, C. Fleta, M. Koehler, M. Lozano, C. Parkes, U. Parzefall, G. Pellegrini, and B. Rakotomiaramanana. Charge collection studies and electrical measurements of heavily irradiated 3D double-sided sensors and comparison to planar strip detectors. *Nuclear Science, IEEE Transactions on*, 58(6):3370 –3383, Dec. 2011.

[36] D. Pennicard, R. Bates, C. Fleta, M. Lozano, C. Parkes, and G. Pellegrini. Design, simulation, production and initial characterisation of 3D silicon detectors. *NIM A: Accelerators, Spectrometers, Detectors and Associated Equipment*, 598(1):67–70, 2009.

[37] G. Pellegrini, R. Bates, C. Fleta, M. Lozano, D. Pennicard, and M. Ullan. First double-sided 3-D detectors fabricated at CNM-IMB. *NIM A: Accelerators, Spectrometers, Detectors and Associated Equipment*, 592(1-2):38–43, 2008.

[38] J.R. Janesick. *Scientific charge-coupled devices*, volume 83. Society of Photo Optical, 2001.

[39] A. Theuwissen. The 2009 Nobel Prize in Physics: W. Boyle and G. Smith for the CCD. *Europhysics News*, 40(6), 2009.

[40] M.F. Tompsett, G.F. Amelio, W.J. Bertram, R.R. Buckley, W.J. McNamara, J.C. Mikkelsen, and D.A. Sealer. Charge-coupled imaging devices: Experimental results. *Electron Devices, IEEE Transactions on*, 18(11):992 – 996, nov 1971.

[41] D.F. Barbe. Imaging devices using the charge-coupled concept. *Proceedings of the IEEE*, 63(1):38 – 67, jan. 1975.

[42] W.S. Boyle and G.E. Smith. Charge-coupled devices - a new approach to MIS device structures. *Spectrum, IEEE*, 8(7):18 –27, july 1971.

[43] D. Litwiller. CCD vs. CMOS. *Photonics Spectra*, 2001.

[44] B.E. Burke et al. CCD soft-X-ray detectors with improved high- and low-energy performance. *Nuclear Science, IEEE Transactions on*, 51(5):2322 – 2327, oct. 2004.

[45] R. Turchetta et al. CMOS Monolithic Active Pixel Sensors (MAPS): New eyes for science. *NIM A: Accelerators, Spectrometers, Detectors and Associated Equipment*, 560(1):139–142, 2006.

[46] M. Clampin. Ultraviolet-optical charge-coupled devices for space instrumentation. *Optical Engineering*, 41:1185, 2002.

[47] A.D. Holland, C.M. Castelli, and D.H. Lumb. Further development of CCD X-ray detectors for astronomy. In *Society of Photo-Optical Instrumentation Engineers (SPIE) Conference Series*, volume 1159, pages 113–124, 1989.

[48] E.R. Fossum. Active pixel sensors: Are CCD's dinosaurs? *Proceedings of the SPIE*, 1993.

[49] E.R. Fossum. CMOS image sensors: electronic camera-on-a-chip. *Electron Devices, IEEE Transactions on*, 44(10):1689–1698, Oct 1997.

[50] M. Kyomasu. A new MOS imager using photodiode as current source. *Solid-State Circuits, IEEE Journal of*, 26(8):1116 –1122, aug 1991.

[51] A. Blue et al. Optical and electrical characterization of a back–thinned CMOS active pixel sensor. *Nuclear Instruments and Methods in Physics Research Section A: Accelerators, Spectrometers, Detectors and Associated Equipment*, 604(1-2):215 – 217, 2009. Proceedings of the 8th International Conference on Position Sensitive Detectors.

[52] D. Groom and S. Klein. Passage of particles through matter. *The European Physical Journal C - Particles and Fields*, 15:163–173, 2000. 10.1007/BF02683419.

[53] J.D. Jackson. Electromagnetic form factor corrections to collisional energy loss of pions and protons, and spin correction for muons. *Phys. Rev. D*, 59:017301, Nov 1998.

[54] W. Abdel-Rahman and E.B. Podgorsak. Energy transfer and energy absorption in photon interactions with matter revisited: A step-by-step illustrated approach. *Radiation Physics and Chemistry*, 79(5):552 – 566, 2010.

[55] S.N. Ahmed. *Physics and engineering of radiation detection*. Academic Pr, 2007.

[56] S. Ramo. Currents induced by electron motion. *Proceedings of the IRE*, 27(9):584 – 585, sept. 1939.

[57] L. Rossi. *Pixel detectors: From fundamentals to applications*. Springer Verlag, 2006.

[58] D. Pennicard. *3D Detectors for Synchrotron Applications*. PhD thesis, University of Glasgow, UK, 2009.

[59] W. Shockley. Currents to conductors induced by a moving point charge. *Journal of Applied Physics*, 9:635, 1938.

[60] Z. He. Review of the Shockley-Ramo theorem and its application in semiconductor gamma-ray detectors. *NIM A: Accelerators, Spectrometers, Detectors and Associated Equipment*, 463(1 - 2):250 – 267, 2001.

[61] G. Lindström, E. Fretwurst, and M. Moll. Radiation hardness of silicon detectors - a challenge from high-energy physics. *NIM A: Accelerators, Spectrometers, Detectors and Associated Equipment*, 426(1):1 – 15, 1999.

[62] V. Eremin, Z. Li, and E. Verbitskaya. Effect of radiation induced deep level traps on Si detector performance. *NIM A: Accelerators, Spectrometers, Detectors and Associated Equipment*, 476(3):537 – 549, 2002. Proc. of the 3rd Int. Conf. on Radiation Effects on Semiconductor Materials, Detectors and Devices.

[63] G. Lindström. Radiation damage in silicon detectors. *NIM A: Accelerators, Spectrometers, Detectors and Associated Equipment*, 512(1-2):30 – 43, 2003. Proceedings of the 9th European Symposium on Semiconductor Detectors: New Developments on Radiation Detectors.

[64] R.S. Harper. *Radiation Damage Studies of Silicon Detectors and Searching for an Intermediate Mass Higgs Boson at ATLAS.* PhD thesis, University of Sheffield, UK, 2001.

[65] M. Moll. *Radiation Damage in Silicon Particle Detectors.* PhD thesis, University of Hamburg, Germany, 1999.

[66] A.M. Raighne et al. Precision scans of the pixel cell response of double sided 3D pixel detectors to pion and x-ray beams. *JINST*, 6:P05002, 2011.

[67] M. Mathes et al. Test Beam Characterization of 3-D Silicon Pixel Detectors. *Nuclear Science, IEEE Transactions on*, 55(6):3731 –3735, dec. 2008.

[68] R.L. Bates et al. Charge collection studies and electrical measurements of heavily irradiated 3D double-sided sensors and comparison to planar strip detectors. *Nuclear Science, IEEE Transactions on*, 58(99):3370–3383, 2011.

[69] N. Roxhed, P. Griss, and G. Stemme. A method for tapered deep reactive ion etching using a modified Bosch process. *Journal of Micromechanics and Microengineering*, 17(5):1087, 2007.

[70] X. Llopart, R. Ballabriga, M. Campbell, L. Tlustos, and W. Wong. Timepix, a 65k programmable pixel readout chip for arrival time, energy and/or photon counting measurements. *NIM A: Accelerators, Spectrometers, Detectors and Associated Equipment*, 581(1 - 2):485 – 494, 2007. Proceedings of the 11th International Vienna Conference on Instrumentation.

[71] Z. Vykydal, J. Jakubek, and S. Pospisil. USB interface for Medipix2 pixel device enabling energy and position-sensitive detection of heavy charged particles. *NIM A: Accelerators, Spectrometers, Detectors and Associated Equipment*, 563(1):112 – 115, 2006. Proceedings of the 7th International Workshop on Radiation Imaging Detectors.

[72] T. Holy, J. Jakubek, S. Pospisil, J. Uher, D. Vavrik, and Z. Vykydal. Data acquisition and processing software package for medipix2. *NIM A: Accelerators, Spectrometers, Detectors and Associated Equipment*, 563(1):254 – 258, 2006. Proceedings of the 7th International Workshop on Radiation Imaging Detectors.

[73] D. Turecek, T. Holy, J. Jakubek, S. Pospisil, and Z. Vykydal. Pixelman: a multi-platform data acquisition and processing software package for medipix2, timepix and medipix3 detectors. *JINST*, 6(01):C01046, 2011.

[74] J. Jakubek, A. Cejnarova, T. Holy, S. Pospisil, J. Uher, and Z. Vykydal. Pixel detectors for imaging with heavy charged particles. *NIM A: Accelerators, Spectrometers, Detectors and Associated Equipment*, 591(1):155 – 158, 2008. Proceedings of the 9th International Workshop on Radiation Imaging Detectors.

[75] J.A. Thompson et al. Controlling the EXCALIBUR detector. *ICALEPCS*, 2011.

[76] M. Stanton et al. Area detector design Part II: Application to a modular CCD-based detector for X-ray crystallography. *NIM A: Accelerators, Spectrometers, Detectors and Associated Equipment*, 325(3):558–567, 1993.

[77] H.F.W. Sadrozinski et al. Issues in proton computed tomography. *NIM A: Accelerators, Spectrometers, Detectors and Associated Equipment*, 511(1):275–281, 2003.

[78] M. Barbero et al. A via last TSV process applied to ATLAS pixel detector modules: proof of principle demonstration. *JINST*, 7(08):P08008, 2012.

[79] M. Christophersen et al. Alumina and silicon oxide/nitride sidewall passivation for p-and n-type sensors. *NIM A: Accelerators, Spectrometers, Detectors and Associated Equipment*, 2012.

[80] M. Beimforde. The ATLAS planar pixel sensor R&D project. *NIM A: Accelerators, Spectrometers, Detectors and Associated Equipment*, 636(1):S8–S14, 2011.

[81] S. Eränen, J. Kalliopuska, R. Orava, and T. Virolainen. 3D processing on 6 inch high resistive SOI wafers: Fabrication of edgeless strip and pixel detectors. *NIM A: Accelerators, Spectrometers, Detectors and Associated Equipment*, 607(1):85–88, 2009.

[82] M. Christophersen et al. Laser-scribing and sidewall passivation of p-type sensors. *Presented at the Sixth Workshop on Advanced Radiation Detectors, Trento, Italy*, 2011.

[83] R. Marco-Hernández. A portable readout system for microstrip silicon sensors (ALIBAVA). *NSS Conference Record, 2008. IEEE*, pages 3201–3208, 2008.

[84] N. Van Bakel et al. The Beetle Reference Manual chip version 1.3, 1.4 and 1.5. *Citeseer*, 2004.

[85] R. Mori et al. Charge collection measurements on slim-edge microstrip detectors. *JINST*, 7(05):P05002, 2012.

[86] G. Stewart et al. Analysis of edge and surface TCTs for irradiated 3D silicon strip detectors. *JINST*, 8(03):P03002, 2013.

[87] G. Kramberger. *Signal Development in Irradiated Silicon Detectors*. PhD thesis, University of Ljubljana, Slovenia, 2001.

[88] R. Jeraj and M. Ravnik. Research reactor benchmarks. *Nuclear science and engineering*, 145(1):145–152, 2003.

[89] G. Lindström et al. Radiation hard silicon detectors - developments by the RD48 (rose) collaboration. *NIM A: Accelerators, Spectrometers, Detectors and Associated Equipment*, 466(2):308 – 326, 2001. 4th Int. Symp. on Development and Application of Semiconductor Tracking Detectors.

[90] M. Bass et al. *Handbook of Optics, Third Edition Volume IV: Optical Properties of Materials, Nonlinear Optics, Quantum Optics (set)*. Handbook of Optics. McGraw-Hill Education, 2009.

[91] G. Kramberger et al. Investigation of irradiated silicon detectors by edge-TCT. *Nuclear Science, IEEE Transactions on*, 57(4):2294–2302, 2010.

[92] A. Castaldini, C. Canali, A. Cavallini, F. Nava, and L. Polenta. Double-junction effect in proton-irradiated silicon diodes. *Journal of Applied Physics*, 92(4):2013–2016, 2002.

[93] R. Van Overstraeten and H. De Man. Measurement of the ionization rates in diffused silicon pn junctions. *Solid-State Electronics*, 13(5):583–608, 1970.

[94] G. Stewart et al. Comparison of a CCD and an APS for soft x-ray diffraction. *JINST*, 6(12):C12062, 2011.

[95] Princeton Instruments. PIXIS-XO: 2048B, March 2011.

[96] P. Jerram, D. Burt, N. Guyatt, Y. Henrion, V. Hibon, and J. Vaillant. Back-thinned CMOS sensor optimisation. In *Proc. of SPIE Vol*, volume 7598, pages 13–1, 2010.

[97] J.R. Janesick. *Photon transfer: DN* $\rightarrow \lambda$. SPIE-International Society for Optical Engineering, 2007.

[98] S.E. Bohndiek et al. Comparison of methods for estimating the conversion gain of CMOS active pixel sensors. *Sensors Journal, IEEE*, 8(10):1734–1744, 2008.

[99] European Machine Vision Association. EMVA Standard 1288, Release A3.0, November 2010.

[100] S.S. Dhesi et al. The nanoscience beamline (I06) at Diamond Light Source. In *AIP Conference Proceedings*, volume 1234, page 311, 2010.

Appendix A

List of Publications

The following publications are based on work from this thesis:

Graeme Stewart, R. Bates, A. Blue, A. Clark, S.S. Dhesi, D. Maneuski, J. Marchal, P. Steadman, N. Tartoni and R. Turchetta, **Comparison of a CCD and an APS for soft X-ray diffraction**, Proceedings of the 13th International Workshop on Radiation Imaging Detectors (IWORID), published in the Journal of Instrumentation, Vol. 6 No. 12, p. C12062, December 2011.

Graeme Stewart, R. Bates, C. Fleta, G. Kramberger, M. Lozano, M. Milovanovic and G. Pellegrini, **Analysis of edge and surface TCTs for irradiated 3D silicon strip detectors**, Journal of Instrumentation, Vol. 8 No. 3, p. P03002, March 2013.

Aaron Mac Raighne, K. Akiba, L. Alianelli, R. Bates, M. van Beuzekom, J. Buytaert, M. Campbell, P. Collins, M. Crossley, R. Dumps, L. Eklund, C. Fleta, A. Gallas, M. Gersabeck, E.N. Gimenez, V.V. Gligorov, M. John, X. Llopart, M. Lozano, D. Maneuski, J. Marchal, M. Nicol, R. Plackett, C. Parkes, G. Pellegrini, D. Pennicard, E. Rodrigues, G. Stewart, K.J.S. Sawhney, N. Tartoni and L. Tlustos, **Precision scans of the Pixel cell response of double sided 3D Pixel detectors to pion and X-ray beams**, Journal of Instrumentation, Vol. 6 No. 5, p. P05002, May 2011.

Vladimir V. Gligorov, K. Akiba, M. Artuso, R. Badman, A. Borgia, R. Bates, F. Bayer, M. van Beuzekom, J. Buytaert, E. Cabruja, M. Campbell, P. Collins, M. Crossley, R. Dumps, L Eklund, D. Esperante, C. Fleta, A. Gallas, M. Gandelman, J. Garofoli, M. Gersabeck, H. Gordon, E.H.M. Heijne, V. Heijne, D. Hynds, M. John, A. Leflat, L.F. Llin, X. Llopart, M. Lozano, D. Maneuski, T. Michel, M. Nicol, M. Needham, C. Parkes, G. Pellegrini, R. Plackett, T. Poikela, E. Rodrigues, G. Stewart, J. Wang, Z. Xing, **Charged particle tracking with the Timepix ASIC**, Nuclear Instruments and Methods in Physics Research Section A: Accelerators, Spectrometers, Detectors and Associated Equipment, Vol. 661 No. 1, pp. 3149, January 2012.

Andy Blue, R. Bates, M. Christophersen, L. Eklund, V. Fadeyev, E. Gimenez, V. Kachkanov, J. Kalliopuska, A. Macchiolo, D. Maneuski, B.F. Phlips, H.F.W. Sadrozinski, G. Stewart, N. Tartoni and R.M. Zain, **Characterisation of edgeless technologies for pixellated and strip silicon detectors with a micro-focused X-ray beam**, Journal of Instrumentation, Vol. 8 No. 1, p. P01018, January 2013.